
Masters Theses

Student Theses and Dissertations

Summer 2017

Long-term monitoring of a landslide in Stone County, Missouri using high precision multi-temporal laser scanning

Benjamin Michael Herries

Follow this and additional works at: https://scholarsmine.mst.edu/masters_theses



Part of the [Geological Engineering Commons](#)

Department:

Recommended Citation

Herries, Benjamin Michael, "Long-term monitoring of a landslide in Stone County, Missouri using high precision multi-temporal laser scanning" (2017). *Masters Theses*. 7686.
https://scholarsmine.mst.edu/masters_theses/7686

This thesis is brought to you by Scholars' Mine, a service of the Missouri S&T Library and Learning Resources. This work is protected by U. S. Copyright Law. Unauthorized use including reproduction for redistribution requires the permission of the copyright holder. For more information, please contact scholarsmine@mst.edu.

LONG-TERM MONITORING OF A LANDSLIDE IN STONE COUNTY, MISSOURI
USING HIGH PRECISION MULTI-TEMPORAL LASER SCANNING

by

BENJAMIN MICHAEL HERRIES

A THESIS

Presented to the Faculty of the Graduate School of the
MISSOURI UNIVERSITY OF SCIENCE AND TECHNOLOGY

In Partial Fulfillment of the Requirements for the Degree

MASTER OF SCIENCE IN GEOLOGICAL ENGINEERING

2017

Approved by

Dr. Norbert Maerz, Advisor
Dr. Joseph Guggenberger
Dr. J. David Rogers

ABSTRACT

A terrestrial laser scanning survey was conducted over the course of 1.5 years to test and validate a new target tracking method which characterizes the surface and subsurface behavior of soft slope landslides. Reflective spherical Styrofoam targets were mounted onto steel rods and driven into multiple levels of a landslide located in Stone County, Missouri. These targets were scanned a total of seventeen times over the course of the survey and were used as a proxy to measure the displacement of specific areas of the landslide. The three-dimensional point cloud data was processed through a software suite specifically developed to process data retrieved from reflective spherical targets. A geophysical survey was also conducted toward the later portion of the scanning survey to get a sense of what types of material were below the slide surface. On the final date of the survey, a basic surface map of the landslide was generated based on satellite imagery and physical observations at the slide site. All of these results were compiled and analyzed along with prior control and field tests to see if this new method was a feasible and accurate approach to tracking and predicting surface and subsurface landslide movement. While this approach and method is still relatively new, the results from the survey showed that the displacement of the landslide could be accurately measured and the movement of the landslide could be accurately tracked.

ACKNOWLEDGMENTS

First and foremost, I would like to thank my graduate advisor Dr. Norbert Maerz for all his help during my undergraduate and graduate career at Missouri University of Science and Technology (MS&T).

Secondly, I would like to thank the other members of my committee, Dr. Joe Guggenberger, and Dr. J. David Rogers. Both were also very supportive in my undergraduate and graduate careers at MS&T.

Thirdly, I would like to thank all the people that helped bring this project together. I would like to thank Robert Reals, Ben Hill, Chengxun Lu, and Marissa Hopkins for warmly welcoming me into the LiDAR Applications Team. I would like to specifically thank Ken Boyko for being my guide through and the developer of the lidarsw software suite which made this study possible. I would like to thank Aleksey Khamzin and Nathainail Bashir for performing the geophysical survey for the study. I would also like to thank the Rock Mechanics and Explosives Research Center for giving us the space and means of transportation to perform this study. I would also like to thank the Missouri University of Science and Technology for providing me the opportunity to further my education through the Chancellor's Fellowship and other scholarship opportunities.

Last but certainly not least, I would like to thank my family. My father, mother, and sister have always been there for me and helped to instill and foster my fondness for people and my passion for the outdoors. I can't thank them enough for their constant encouragement and unwavering love.

TABLE OF CONTENTS

	Page
ABSTRACT.....	iii
ACKNOWLEDGMENTS	iv
LIST OF ILLUSTRATIONS.....	vii
LIST OF TABLES	xii
 SECTION	
1 INTRODUCTION.....	1
1.1 LANDSLIDES	1
1.1.1 Causes of Landslides.....	2
1.2 METHODS FOR MONITORING DISPLACEMENT AND GEOMETRY.....	4
1.3 LIGHT DETECTION AND RANGING (LIDAR).....	8
2 METHOD.....	18
2.1 STONE COUNTY LANDSLIDE	18
2.2 DATA COLLECTION.....	23
2.2.1 LiDAR Point Cloud Scans	23
2.2.1.1 LiDAR target setup and designation.....	23
2.2.1.2 TLS equipment and setup	27
2.2.1.3 Data collection	31
2.2.2 Geophysical Survey	39
2.2.3 General Surface Mapping	42
2.3 LIDAR POINTCLOUD AND SPHERE CENTER DATA PROCESSING....	43
2.3.1 Pre-processing and Data Exporting	43
2.3.2 FindMinMax Program	47

2.3.3	Load Program.....	50
2.3.4	View2surf Program.....	54
2.3.5	ClipSpheres Program	58
2.3.6	FindSpheres Program.....	60
2.3.7	Regballs Program.....	61
2.3.8	Surf2vrml Program	64
2.3.9	Precision and Repeatability Tests of Sphere Center Positions	67
2.3.10	Data Representation	70
3	RESULTS.....	72
3.1	GENERAL DISPLACEMENTS AND RATES OF MOVEMENT	72
3.2	SEASONAL DISPLACEMENT MOVEMENT REPORTS	84
3.2.1	Summer and Fall Seasons of 2015.....	84
3.2.2	Winter Season of 2015 through 2016	90
3.2.3	Spring through Fall Seasons of 2016.....	96
3.3	GEOPHYSICAL RESITIVITY RESULTS AND INTERPRETATION ..	102
4	CONCLUSIONS.....	111
4.1	LIMITATIONS OF CURRENT PROCEDURE.....	111
4.2	FUTURE RESEARCH AND DEVELOPMENT OF METHOD	111
	APPENDIX.....	114
	BIBLIOGRAPHY.....	115
	VITA	120

LIST OF ILLUSTRATIONS

	Page
Figure 1.1 Time Dependent Deformation Curve	3
Figure 1.2. Sketch of a Quadrilateral	8
Figure 2.1. General Location of Stone County Landslide	19
Figure 2.2. Google Earth Plan View of Stone County Landslide	20
Figure 2.3. Stone County Landslide near Branson, MO.....	21
Figure 2.4. Garber Quadrangle 2004 Geologic Map 1:24000	22
Figure 2.5. Garber Quadrangle 2004 Geologic Map Legend	22
Figure 2.6. Typical Control Rod With 6” (152.4 mm) Target Embedded outside the Slide Boundaries	24
Figure 2.7. Typical Floating Target Rod with Twin 4” (101.6 mm) Targets Embedded within Slide Boundaries	25
Figure 2.8. Idealized Movement of Styrofoam Spheres above a Planar Slip Surface, when the Base of the Rigid Rod is above the Shear Surface	25
Figure 2.9. Idealized Movement of Styrofoam Spheres above a Planar Slip Surface when the Base of the Rigid Rod is below the Shear Surface	26
Figure 2.10. Idealized Movement of Styrofoam Spheres above a Circular Slip Surface when the Base of the Rigid Rod is above the Shear Surface	26
Figure 2.11. Leica Scanstation 2 Post-setup	28
Figure 2.12. Google Earth View Scanner Position Relative to Landslide	29
Figure 2.13. Tribrach Leveling System	30
Figure 2.14. Data Collection Equipment after Setup	31
Figure 2.15. Argonaut OEM D15R-Series Field Laptop	32
Figure 2.16. Cyclone Project Selection/Creation	33
Figure 2.17. Cyclone Project Selection/Creation	33

Figure 2.18. Beginning of Imaging Process.....	34
Figure 2.19. Cyclone Imaging Process	34
Figure 2.20. Cyclone Fencing/Scanning Process.....	35
Figure 2.21. Resolution Test Sphere Configuration	36
Figure 2.22. Plan View of ERT Profiles	40
Figure 2.23. Setup of Profile 1 (North Side of Slide)	40
Figure 2.24. Setup of Profile 2 (Middle Part of Slide).....	41
Figure 2.25. Setup of Profile 3 (South Side of Slide)	41
Figure 2.26. AGI SuperSting R8 Multichannel Electrode System	42
Figure 2.27. Ground Surface Map	43
Figure 2.28. OutcropData Directory	45
Figure 2.29. Location of Pointfiles within the Specific Site6 Directory	45
Figure 2.30. Initial Command Prompt Window	46
Figure 2.31. Input of the “cd lidarsw” Command.....	47
Figure 2.32. Initial Running of the FindMinMax Program	50
Figure 2.33. Load Prior to Running the Program	52
Figure 2.34. Initial Running of the Load Program.....	52
Figure 2.35. July 19, 2015 Color Image Generated by the Load Program	53
Figure 2.36. December 16, 2016 Color Image Generated by the Load Program	53
Figure 2.37. July 19, 2015 Intensity Image Generated by the Load Program	54
Figure 2.38. December 16, 2016 Intensity Image Generated by the Load Program	54
Figure 2.39. Images of Two Surfaces in View2surf	56
Figure 2.40. Zoomed View of the First Surface	56

Figure 2.41. Point Set of Horizontal, Vertical, and x, y, z Coordinates	57
Figure 2.42. Specific Designator Selected in View2surf	58
Figure 2.43. Example of the ClipSpheres Input Data	59
Figure 2.44. WRL File View of ClippedPointFiles	59
Figure 2.45. FindSpheres Calculating the Best Fit Centers	60
Figure 2.46. FindSpheres Refining Best Fit Centers	61
Figure 2.47. Regballs Displacements of Control Spheres	62
Figure 2.48. Regballs Displacements of Floating Spheres	62
Figure 2.49. Regballs Report Example	63
Figure 2.50. Homogeneous Transformation Matrix of M	64
Figure 2.51. dateList.txt File	65
Figure 2.52. vrmlconfig.txt File	67
Figure 2.53. Displacement Rig	68
Figure 3.1. General Displacement and Rate Report from Base to Final Date	74
Figure 3.2. General Displacement Report with Linear Trendline	75
Figure 3.3. General Displacement Report Linear Trendline Statistics	76
Figure 3.4. Overall Change in Top Sphere X Position between July 19, 2015 and January 8, 2017	77
Figure 3.5. Overall Change in Top Sphere Y Position between July 19, 2015 and January 8, 2017	78
Figure 3.6. Overall Change in Top Sphere Z Position between July 19, 2015 and January 8, 2017	79
Figure 3.7. Overall Rod Rotation between July 19, 2015 and January 8, 2017	80
Figure 3.8. Example of Large Rod Movement	81
Figure 3.9. Divot on Upper Middle Portion of the Slide	82

Figure 3.10. Example of Movement within a Non-Vegetated Area (New Rods Placed March 31, 2016)	83
Figure 3.11. Summer and Fall 2015 Displacement Report with Linear Trendline.....	85
Figure 3.12. Summer and Fall 2015 Displacement Report Linear Trendline Statistics	85
Figure 3.13. Summer and Fall 2015 Change in Top Sphere X Position between July 19, 2015 and November 22, 2015	87
Figure 3.14. Summer and Fall 2015 Change in Top Sphere Y Position between July 19, 2015 and November 22, 2015	88
Figure 3.15. Summer and Fall 2015 Change in Top Sphere Z Position between July 19, 2015 and November 22, 2015	89
Figure 3.16. Summer and Fall 2015 Rod Rotation between July 19, 2015 and November 22, 2015	90
Figure 3.17. Winter 2015 through 2016 Displacement Report with Linear Trendline	91
Figure 3.18. Winter 2015 through 2016 Displacement Report Linear Trendline Statistics	91
Figure 3.19. Winter season of 2015 through 2016 Change in Top Sphere X Position between December 16, 2015 and May 13, 2016.....	93
Figure 3.20. Winter season of 2015 through 2016 Change in Top Sphere Y Position between December 16, 2015 and May 13, 2016.....	94
Figure 3.21. Winter season of 2015 through 2016 Change in Top Sphere Z Position between December 16, 2015 and May 13, 2016.....	95
Figure 3.22. Winter season of 2015 through 2016 Rod Rotation between December 16, 2015 and May 13, 2016	96
Figure 3.23. Spring through Fall 2016 Displacement Report with Linear Trendline.....	97
Figure 3.24. Spring through Fall 2016 Displacement Report Linear Trendline Statistics	97
Figure 3.25. Spring through Fall 2016 Change in Top Sphere X Position between March 31, 2016 and November 5, 2016.....	99
Figure 3.26. Spring through Fall 2016 Change in Top Sphere Y Position between March 31, 2016 and November 5, 2016.....	100

Figure 3.27. Spring through Fall 2016 Change in Top Sphere Z Position between March 31, 2016 and November 5, 2016.....	101
Figure 3.28. Spring through Fall 2016 Change in Rod Rotation between March 31, 2016 and November 5, 2016	102
Figure 3.29. Three-Dimensional View of Landslide with Profile and Rod Positions	104
Figure 3.30. Close-up of Profile 1 with Zoomed in View of Rod 61	104
Figure 3.31. Exposed Dolomite Outcrop on Northeast Corner of Landslide	106
Figure 3.32. ERT Profile 1 (North Side of Landslide)	106
Figure 3.33. ERT Profile 1 with Slide Plane Interpreted and Rods Superimposed	107
Figure 3.34. ERT Profile 2 (Middle Portion of Landslide).....	108
Figure 3.35. ERT Profile 2 with Slide Plane Interpreted and Rods Superimposed	108
Figure 3.36. Non-Vegetated Areas of Dense Fill (Example in Red).....	109
Figure 3.37. ERT Profile 3 (South Side of Landslide)	110
Figure 3.38. ERT Profile 3 with Slide Plane Interpreted and Rods Superimposed	110

LIST OF TABLES

	Page
Table 2.1. Sphere Resolution Test Results	38
Table 2.2. Comparison of LiDAR Measured Displacement with the Actual Displacement of the Four Target Balls.	69
Table 2.3. Results of Displacement Field Test	70
Table 3.1. General Displacements and Rates of Movement Measured by Scanstation 2	73

1 INTRODUCTION

1.1 LANDSLIDES

Ever since mass wasting events started to affect human activity, people have studied them and monitor their behavior. These events include rockfalls, debris flows, and landslides. Cruden (1991) defines a landslide as “the movement of a mass of rock, debris, or earth down a slope”. There are many types of landslides but one type of particular interest to geotechnical and geological engineers are soft slope landslides. The reason that soft slope landslides are of such interest is the fact that they cause large amounts of loss of life and loss of property each year. They also cause travel hazards by blocking highways and other transportation lines. Soft slope landslides are the attributed cause of over one billion dollars in damages throughout the world each year (Fleming, 1980). According an estimate by the National Research Council, in the United States alone, landslides are the cause of 25 to 50 deaths every year (Schuster and Highland, 2001). The worldwide death toll is much higher, at around 4600 deaths per year due to landslides (Petley, 2012). This estimate was taken from recorded landslide fatalities between 2004 and 2010, and the author suggests these numbers may underestimate the true loss. The increase in population throughout the world and the need for more residential land areas has caused populations to advance into landslide prone areas.

If the onset of a catastrophic landslide can be predicted, loss of life and property can be highly mitigated. Engineers have developed ways to analyze and calculate potential slope failures. These analyses can occur in the form of a computer programs or digital or mathematical models using an algorithm. Knowing the geometry of the

subsurface slip plane can greatly help to model the true behavior of a landslide. It is also helpful to know what sort of material the landslide is comprised of, such as soil type and rock type and how these materials are distributed about the landslide. Hydrological properties and their distribution are also beneficial to know because these properties can greatly increase the probability of failure depending on where they are in the slide.

1.1.1 Causes of Landslides. Catastrophic landslides typically do not initiate instantaneously. They usually give some sort of warning in the form of small movements before they ultimately fail. Landslides often follow the time dependent creep curve shown in Figure 1.1. Deformation follows in three separate phases, known as primary, secondary, and tertiary creep. The primary failure phase is also known as the transient creep phase. During this phase, a relatively large amount of initial deformation may occur over a relatively short period of time. The initial stress conditions are equilibrated before the second phase of failure begins. The second phase of failure is known as the steady state creep phase. There is a relatively small amount of predictable movement across the landslide over a long period of time. This is the optimal phase where monitoring, sampling, and remediation or mitigation can take place. According the Cruden and Varnes (1996) scale, a slow-moving landslide travels at 5×10^{-3} mm/sec or less. This movement is equal to about 17 inches of movement per day (Cruden, 1996); however, many slides move at much slower velocities. The tertiary phase of failure is also known as the accelerating creep phase. It constitutes the final failure of a landslide and is accompanied by a large amount of deformation or a catastrophic failure. Prediction of this final phase is important if mitigation techniques are to be attempted. Figure 1.1 shows these phases in a time versus deformation graph.

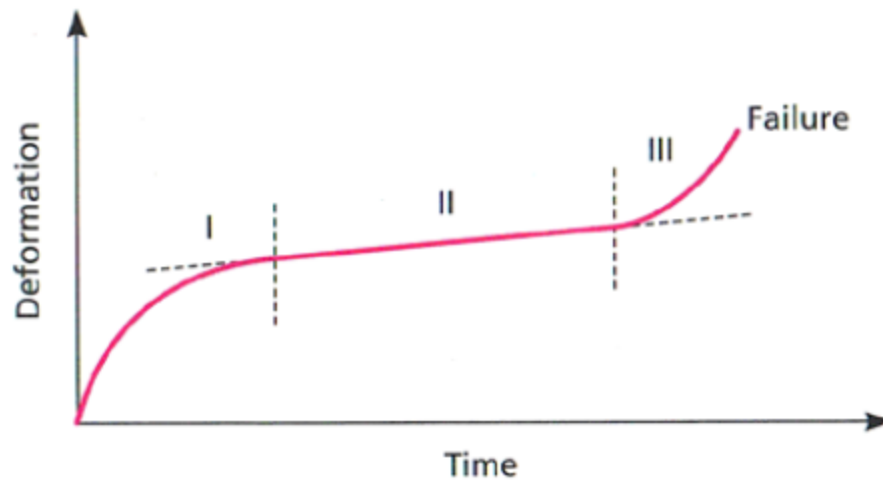


Figure 1.1 Time Dependent Deformation Curve
 (Gonzales de Vallejo, 2011)
 Transient creep phase designated by I
 Steady state creep phase designated by II
 Accelerating creep phase designated by III

Landslides occur when the driving forces on a slide overcome or become greater than the resisting forces on a slide. The driving forces in the slide are greatly dominated by gravity. Seismic activity can temporarily increase the driving forces as well. The resisting forces in the slide are composed of shear resistance (frictional forces, and cohesion). These are largely dependent on the type of material as well as the angle of the slope. Pore-water pressure from in situ water or from weather events can decrease these resisting forces by decreasing the effective normal stress acting on the shear planes. This makes it easier for the slope to fail. The ratio of resisting forces over driving forces in a particular landslide or slope can be described as that slope's factor of safety. In theory, a factor of safety greater than 1 indicates a stable slope and a factor of safety less than 1 indicates an unstable slope.

Landslides that are the most problematic are ones that threaten roadways and residential areas. Landslides can also greatly affect the areas around them, especially the area above and below a particular landslide. Landslides also frequently occur in areas that have a history of previous landslide activity. A majority of these slides are triggered by heavy rainfall events that accumulate large amounts of water which can soak into the subsurface. This water causes the buildup of pore water pressure which reduces the effective stress, and thus reduces the resisting forces. Areas with large amounts of seismic activity are also prone to landslides. Even relatively small earthquakes with local Richter magnitudes of 4 have the capability of triggering landslides (Keefer, 1984). This is also dependent on the slide's distance from the epicenter of the earthquake. Due to the high risk associated with landslides and the prevalence of this problem around the entire world, solutions have been pursued by many government agencies and research programs, such as the United States Geological Survey (Reid, 2012). These agencies and programs build teams that go out to observe areas and slopes that have landslide potential. It is important that these teams discover what different materials compose the potential slide as well as the geometry of the slide on the surface and subsurface. It is also important to know if the specific area has any history when it comes to landslide activity. It is most important to predict when a failure of a slope might occur. Instrumentation and monitoring is needed for a successful prediction to occur.

1.2 METHODS FOR MONITORING DISPLACEMENT AND GEOMETRY

Total stations are highly sophisticated pieces of surveying equipment that can be used to calculate the coordinates of points using line of sight angle and distance measurements from the total station to an unknown point. Total stations are composed of

an electronic theodolite coupled with an electronic distance measurement (EDM) tool. A target on a moving surface could be surveyed multiple times over successive time periods in order to track the change in its position and therefore track the deformation or movement of the surface at that point. Total stations are very accurate with a limited number of points, but it can be difficult and time consuming to track an entire landslide body using just a total station (Ashkenazi, 1980). EDM measurements have a typical precision of 1 to 5 mm depending on the distance from the target in question (Gili, 2000).

While geophysical surveys can be expensive, they can give a great indication on the material in the subsurface. Electrical resistivity tomography surveys along multiple profiles of a landslide surface can give a picture of the material below the surface up to a certain depth, depending on electrode spacing. It may be possible to discern depth to a slip surface and the potential geometry of the slip surface from these types of surveys. However, conclusions like this are based on interpretation and are highly subjective. It is important to pair and correlate other test data with these surveys and not just rely on the geophysics alone.

Global positioning system (GPS) satellites allow the collection of longitude, latitude, and height coordinates of points on the surface of the earth by tracking electromagnetic waves being transmitted by the satellites. Northing and easting measurements can also be collected. These longitude, latitude, and height coordinates or spatial coordinates can be thought of as x, y, and z coordinates in a reference system. Operating these data collection and processing systems can be difficult due to their complexity. The two data collection methods that are used most often are the fast static method and real time kinematic method. The fast static (FS) method became available in

1992 and the real time kinematic (RTK) method became available in 1994, with both of them emerging in the late 1980s and 1990s. Deformation measurements of specific points on a landslide surface can be tracked overtime to characterize the behavior of a specific landslide. This requires a GPS base station to be set up, as well as multiple other GPS antennae to be setup at specified points in order to measure the movement of those points. These systems are quite sensitive to reception loss and signal quality, especially using the RTK method. Gili states that the typical precision of a GPS system when measuring the change in x, y, and z coordinates of a point is 5 to 10 mm (Gili, 2000).

Terrestrial photogrammetry and aerial photogrammetry are other methods that can be used to track surface displacements. These methods employ the use of multiple images of a specific site that have been taken over known periods of time. Specific points can be gathered from these images and their spatial changes can be tracked over time. Terrestrial photogrammetry has a typical precision of 20 mm if the range is less than 100 m (Gili, 2000). Aerial photogrammetry has a typical precision of 10 cm (Gili, 2000).

Another monitoring method that has been used increasingly in the past decade and is continually developing is ground-based interferometric radar (GBIR). These systems measure electromagnetic waves that are superimposed in order for the waves to interfere with each other. GBIR systems analyze the interference of these waves to extract information, such as movement and deformation. These systems have been used in accordance with GPS and photogrammetry to track landslide movement. Vegetation and landslide movement can cause large amounts of noisy data due to these changes affecting the accuracy of the survey. In a displacement study conducted in 2013, Lowry determined an error of 3.5 to 4 mm in the measurements the study collected. During this

study, the landslide was imaged with radar that had varied pixel sizes. At the toe the pixels were 2 m by 0.75 m and at the crown they were 4 m by 0.75 m. Lowry was only able to resolve the horizontal displacements of the slide. Vertical displacements were not able to be resolved in this study. (Lowry, 2013). Multiple problems can arise when measuring landslide displacements with a GBIR system. The measurements can have a large amount of ambiguity when the movement of the landslide becomes greater than the wavelength used to measure the movement. Another problem is the various scanning positions that would occur if a user brought the GBIR system back and forth from the field. If the GBIR system has a radically different scanning position between scans, this can make registration a particularly difficult process due to the loss of the wavelength phase that was established at the first scanning position. The final problem encountered with landslide measurement using GBIR systems is that these systems can only measure precisely in one dimension such as distance. The other two principal direction accuracies are quite low.

Quadrilaterals are an old method that has been used to track the movement and deformation of landslide surfaces. Quadrilaterals consist of four separate stakes that are driven into the ground. The distances between the stakes as well as the angles between each quadrilateral are measured. After a period of time these distances and angles are measured again and the difference in a distance or angle measurement gives an indication on how a landslide surface is moving (Baum, 1988). These distances and angles are manually measured and a representation of them is shown in Figure 1.2. Due to the manual nature of the setup of the quadrilaterals and measurements of the distances and

angles between stakes, there is a much greater chance that error can be introduced into the surveys.

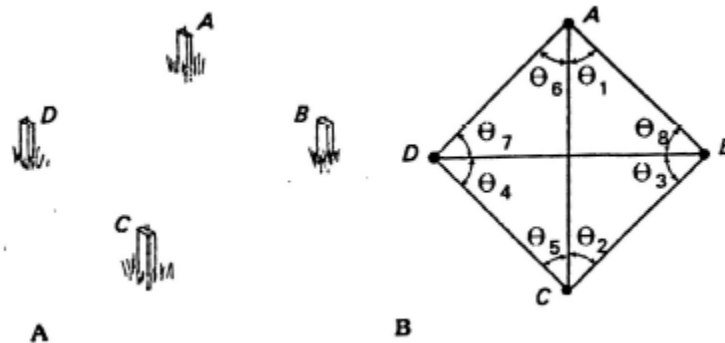


Figure 1.2. Sketch of a Quadrilateral
(Baum, 1988)

There are multiple other monitoring methods that are covered more extensively in Mikkelsen (1996) and Angeli (2000). There are also numerous methods on detecting and locating the slip surface of a landslide covered by Hutchinson (1983). A relatively new method of monitoring landslide displacement compared to the above-mentioned methods is LiDAR.

1.3 LIGHT DETECTION AND RANGING (LIDAR)

LiDAR systems employ the use of a laser, or light amplification by stimulated emission of radiation, to measure distances from a transmitter/receiver to a physical object. LiDAR is facilitating many new ways to monitor and track the movement of landslides. LiDAR came into common use in the late 1990s. While some of these systems

were rather expensive, the cost had significantly decreased towards the end of the decade. The technology and the use of it for monitoring have been progressing ever since.

LiDAR systems acquire data in a point cloud format. Each of these points in space represents a reflection of light energy back to the receiver after it has been transmitted to and reflected back by an object. These points have specific x, y, and z coordinates associated with them based on an intrinsic reference within the LiDAR scanner. These points can be used to generate digital elevation models (DEMs) or digital surface models (DSMs) which can accurately present a certain slope or landslide at a moment in time. This data can also be used to show the movement or difference in position of millions of points over time. It can further be used to infer how fast a slide is moving, how much material is moving, and when specific parts of the slide could fail in the future.

Laser scanning systems or LiDAR units are composed of a transmitter/receiver of a laser scanning device. There are two common methods for determining the range of a point on an object or surface. They are the phase shift method and the time of flight method. The phase method is more accurate but it can have a limited distance to which it can measure. This can be problematic for larger slides where the scanner needs to be farther away to collect data on the entire slide. The phase shift method sends out pulses of light at a specific modulating frequency depending on the manufacturer of the scanning system. The reflected light is then monitored with the modulation frequency and compared to the frequency of the sent light. The resulting phase shift is resolved into a distance measurement. The time of flight method measures the time it takes for a laser pulse to be sent out from the transmitter, reflect off an object and travel back to the

receiver. The physical objects that are normally encountered on a landslide surface are either vegetation, the ground surface, some exposed rock, or a specifically placed target. When the laser pulse encounters these objects, some of the energy back scatters. These back scatterings are then reflected back to and detected by the receiver. These reflections are also known as returns. The time of flight method has the potential to measure at great distances (Jaboyedoff, 2012). Distance is computed by calculating the two-way flight time of light. This equation is placed below:

$$2d = c * \Delta t \quad (1)$$

Where:

d is the distance the pulse traveled from the transmitter to the reflection point.

c is the speed of light.

Δt is the time it takes for the laser pulse to travel from the transmitter to the surface and back to a receiver (Jaboyedoff, 2012).

Measurements are made with respect to the position and orientation of the scanner (local coordinate system). Knowing the particular position and orientation of the laser scanner allows for the deduction of the position of a reflective surface with respect to global coordinate systems. In either case the transformation of the x , y , and z coordinates can be calculated.

There are two main types of laser scanning systems. They are the airborne laser scanner (ALS) and the terrestrial laser scanner (TLS). The airborne laser scanner usually collects data at much lower resolution than the terrestrial scanner but can cover much more area in a short period of time. This is due to the distance between the laser scanner

and the scanned object, and the speed of the aircraft. These types of scanners have been used to create DEMs and landslide susceptibility maps. These DEMs are used extensively to enhance map generation and accuracy on topographic and geologic maps. Terrestrial laser scanners can be used to map and monitor more specific locations such as a single slide or slope. The data that is collected can be used to indicate specific problems and their extent. Terrestrial laser scanners usually have much better resolution than airborne scanners due to the decreased distance between the scanner and the scanned object, and the fact that they are typically stationary during data collection. Terrestrial laser scanners usually collect data from a position horizontal to the target or object they are scanning, while the airborne laser scanners collect data from vertically above the target or object in question. A study done in 2015 cites accuracies of airborne laser scanning to be in the range of 0.24 to 0.75 m (Fey et al., 2015).

When studying and characterizing a particular landslide, it is essential to generate an accurate three-dimensional model of the landslide as well as the adjacent area. In the past and traditionally, this process was completed using a writing instrument and a piece of paper during a walk-over geomorphological survey. During a traditional survey, it was particularly beneficial to have test pits and drilled boreholes available to ground truth the surface observations. This sort of work could be time consuming and require high amounts of expertise in a particular geographic or geologic region. In order to drill a borehole on a particular site, a drilling rig would need to be mobilized to the site. If the ground was unstable, it is possible that putting a drill rig on the unstable ground could destabilize a slope. Even more recent than these walk-over geomorphological surveys, the use of aerial photographs and aerial ortho-photographs have been used to supplement

the surface observations of particular landslide sites and geophysical surveys have further added subsurface data in areas where boreholes and pits are not readily available. These landslide surveys and models can be further enhanced by the use of other ground surveying instruments like electronic distance meters, theodolites, levels, or total stations. All of this equipment and these techniques, while accurate, can be expensive and time consuming and may not be able to detect the small movements of a landslide that is needed in order to predict failure. Millimeter to sub-millimeter accuracy could greatly enhance predicting failures and specific landslide models could be created quickly and easily (Rowlands, 2003).

Rowlands (2003) details a laser scanning survey done of a landslide in Broadway near Worcestershire in England. Advantages of surveying the landslide with a laser scanner rather than the traditional methods mentioned above were outlined. They included that laser scanning systems were able to provide an objective, detailed model that can be worked into a three-dimensional model of a landslide surface. The laser scanning system substantially cut down on labor and expense while increasing the detail at which measurements could be obtained. The data collected by these systems has the flexibility to be processed in many different ways and by many different available software packages. Rowlands also says that if multiple scans of a single site were acquired over a longer period of time, indications of slope movement direction and magnitude could be deduced (Rowlands, 2003).

There are some specific problems that arise at landslide sites that are not related to the type of laser scanner system that is used. Site accessibility is a problem that can arise regardless of where the site is located. The ability to travel to the site is a key part of any

laser scanning survey. Most terrestrial laser scanners are relatively easy to transport and require minimal time and work to set up. The ability to position the scanner at a proper distance from the slide is another problem that arises in scanning survey. A proper field of view for the scanner is needed in order to capture the entire landslide. With some sites, multiple scanner positions are needed to capture the landslide. This leads to the need to the registration of multiple images together which can reduce the overall accuracy. If the scanner position is too low compared to the base of the slide, the perspective of the scan can cause errors in position measurement. Depending on the desired resolution of the digital model, the distance between the scanner and the landslide can be adjusted.

The presence of vegetation on the slide surface can greatly affect the quality of the laser scanning data. A recent study into tracking the movement of landslides using three dimensional measurements where the surface is vegetated was undertaken (Franz, 2016). The quality of data collected and the monitoring process is heavily reliant on how much energy of a laser pulse is reflect off of a target surface or object. This reflection needs to be strong enough to travel back to the laser scanner. Vegetation can cause difficulties in properly mapping the terrain due to some of the laser energy reflecting off this vegetation rather than the actual ground surface. When scanner laser signals are backscattered from trees or vegetation rather than the ground surface, the signal can become smaller than the scanner's detection threshold. A slide may move only millimeters in a month while the vegetation on that slide grows at a rate of 100s of millimeters in the same month. The scanner could be tracking the growth of the vegetation rather than the movement of the slide. It is sometimes essential to filter out data that does not represent the ground surface.

Targets mounted on rods can be driven into parts of the landslide surface during its steady state phase so the movement of the slide can be tracked with much greater accuracy and precision. Different targets have been driven into stable areas of landslides to test their feasibility and reflectiveness. Franz tested five different targets in a 2016 study. The targets used were a white polystyrene sphere, a compact disc, a concave tetrahedron comprised of three white plastic triangles, a reflective road sign, and a planer square with a checkerboard pattern on the face. The targets that came up with the best results for durability, weather exposure, and contrast reflectivity were the white plastics. Franz correlated the LiDAR measurements that were collected during the 2016 and they were comparable with classical methods. In a separate study conducted by Monserrat in 2008, it is noted that specific types of targets played a minor role in the overall estimation of deformation and displacement. The use of a cheaper and more durable target option will give similar results to an expensive target option (Monserrat, 2008; Franz, 2016).

When LiDAR systems collect data in point cloud format, the data can be further processed to create a digital surface model. These models can be compared to other models that were generated at a different time or from a different scanning position. A method for comparing digital surfaces or matching digital surfaces was detailed by Gruen (2005) and adapted by Monserrat (2008). In order to measure the movement or deformation of a complicated and varying surface such as a landslide, one has to discretize that landslide into a mathematical surface. This surface can then be matched or subtracted from another surface to find the movement of specific sections of a surface. In order to match surfaces with each other, the user must co-register the surfaces to the same coordinate system. Most TLS systems or other systems that collect point cloud data do

not do this automatically. If point clouds that are collected at different times or from different transmitter/receiver positions are automatically co-registered to each other there can be large errors in measurement. Some scanners automatically co-register surfaces with mismatching coordinate systems before trying to match the surfaces (Gruen, 2005; Monserrat, 2008).

Laser scanners and laser scanning systems have the ability to directly measure three dimensional coordinates with a large volume of measurements in a relatively short period of time. One disadvantage of laser scanners is that they are line of sight tools. They can only directly measure what they “see” or where light can travel from the transmitter and return to the receiver. Some large objects or large surfaces may require multiple line of sight scans in order to completely construct them digitally. Each of these scans has its own specific coordinate system. The point clouds that come from these scans need to share a single common coordinate system in order to make an analysis or further process the point cloud data. This process is called registration. Gruen (2005) goes on to explain their proposed method which contributes to understanding of four problems that occurs in three-dimensional surface matching. Firstly, is important to be able to match non-rigidly deformed data sets. Secondly, there is a problem with matching of full three-dimensional surfaces rather than just patches of three-dimensional surfaces or two dimensional surfaces. Thirdly, it is necessary that the mathematical model generated to represent an object matches what is happening in the physical reality to the best of the model’s ability. Lastly, these methods that are being developed require a need for internal quality control. Gruen (2005) states that the method they propose fulfills these aforementioned criteria.

Gruen's proposed method is called Least Squares 3D Surface Matching (LS3D).

A singular three-dimensional search surface or multiple three-dimensional search surfaces are matched to a three-dimensional template surface. The template surface is a baseline, and the search surfaces are matched to the baseline. These surfaces are matched by minimizing the sum of squares of the Euclidean distances between the surfaces.

$$d(p, q) = \sqrt{\sum_{i=1}^n (q_i - p_i)^2} \quad (2)$$

General Distance Formula in Euclidean Space

$$d(p, q) = \sqrt{(q_1 - p_1)^2 + (q_2 - p_2)^2 + (q_3 - p_3)^2} \quad (3)$$

Three-Dimensional Distance Formula in Euclidean Space

Monserrat (2008) uses Gruen's method in his own study. The study is in conjunction with matching terrestrial laser scanning data to three-dimensional surfaces. The study follows a general procedure that is used across laser scanning surveys. The first step of the procedure is to actually acquire or collect the TLS data. TLS data is collected across a target area which includes both constant areas and moving areas. It is important to collect data from both moving and non-moving areas to have internal quality control across the entire data collection area. A data collector must take into account the distance from the sensor to the scanned area or object as well as the resolution at which the object is scanned. This will contribute to the variability in data. Collecting data from a moving area completed surrounded by non-moving areas can greatly increase the amount of control inherent in the data. After the first data acquisition, another acquisition must

occur in order to have another set of data with which to compare and match to the first. This can be done as many times as necessary or desired. It is best to wait a period of time in which there can be a measurable amount of deformation of the scanned object or surface.

The second step of the procedure is to globally co-register the data that has been collected. The first point cloud is referred to as a reference or template point cloud and the second or proceeding point clouds are referred to as search point clouds. Each of these point clouds, whether they be a template or search point cloud has its own specific reference or coordinate system. The search point clouds' coordinate systems need to be transformed to the template point cloud coordinate system in order to match and compare them. Global co-registration of the two surfaces can be made easier and systematic errors can be minimized by including sets of ground control points which is covered previously in the literature by Giussani and Scaioni (2004).

The final step is to go about estimating the deformation parameters of the data sets. There are two important actions in the investigation of the deformation of the scanned target or object. The user must first select the particular sections of the data to be investigated and then the user must estimate the transformation parameters for each section. These transformation parameters include three translations and three rotations, and thusly state the type of deformation that has taken place between the two data sets. This can be further done between multiple data sets. There are other similar procedures outlined by Giussani & Scaioni (2004), Prokop (2009), Dunning (2009), and Barbarella (2013).

2 METHOD

A similar procedure to Monserrat's was conducted with a new approach to measuring the landslide movements. This new method is able to track both the surface and subsurface movements of a landslide with millimeter to sub-millimeter accuracy and will greatly increase the usefulness of LiDAR surveys, landslide tracking, and failure prediction. Tracking reflective targets mounted to rods driven into the unstable areas of the landslide gives a measurement of the overall movement of the landslide with great accuracy. It also provides information on the depth and geometry of the slip surface of the landslide.

2.1 STONE COUNTY LANDSLIDE

A TLS survey campaign was performed on a landslide in Missouri further test the tracking of landslide movement. The survey lasted for 550 days in which 17 separate scans were performed. Each of these scans corresponds to a date during the survey. The research into this particular landslide is ongoing. The landslide slope is located near Branson, MO, close to the Stone and Taney County line on the Stone County side. It is on the west side of the Ozark Mountain Highroad on Missouri Highway 465. The latitude and longitude coordinates for the slope is 36.676254, -93.317727. This landslide is located within the Garber 7.5-minute quadrangle as designated by the Missouri Geological Survey. The general location of the landslide can be seen in Figure 2.1 and the plan view of the landslide can be seen in Figure 2.2. The landslide is slow moving and does not pose an immediate threat to the adjacent highway. It is directly off the

southbound side of the highway and can be accessed on foot, but portions of the slide are rather steep.

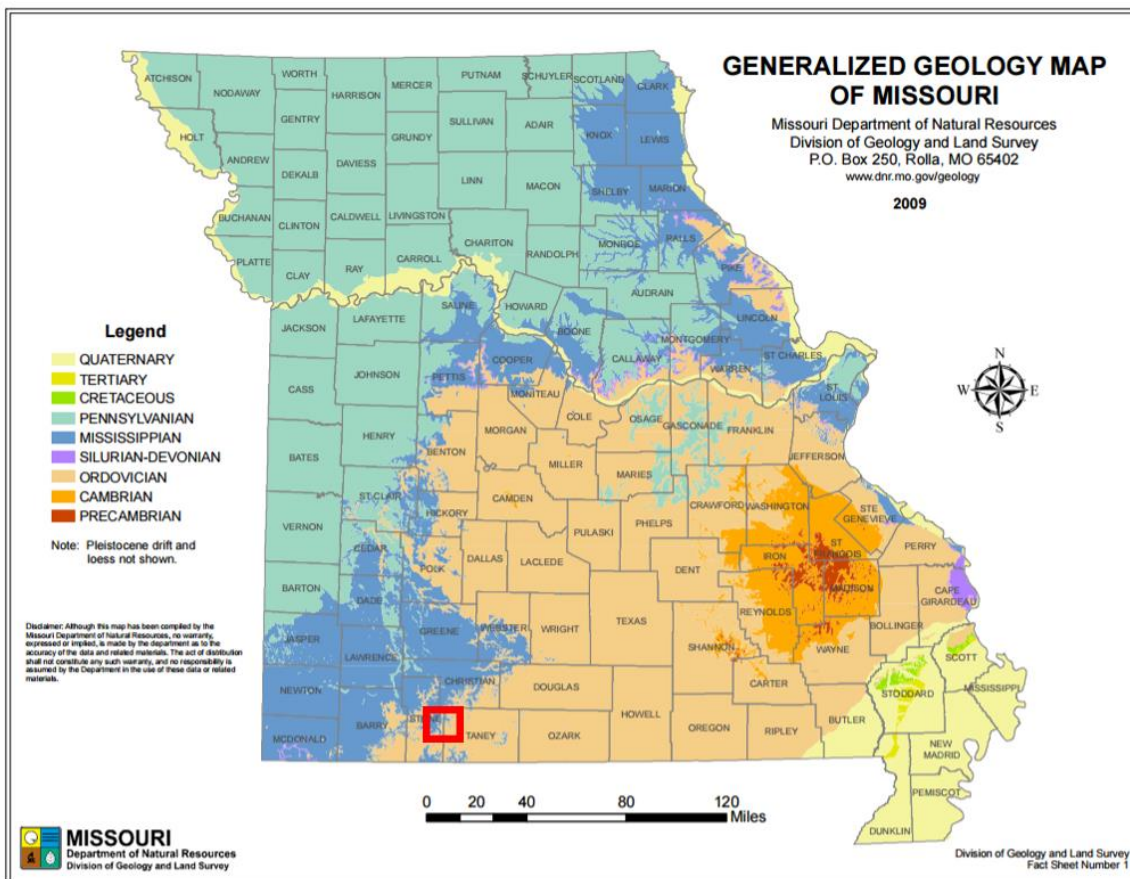


Figure 2.1. General Location of Stone County Landslide (Location outlined in red)



Figure 2.2. Google Earth Plan View of Stone County Landslide

This landslide has typical soft slope landslide geomorphology. There is a head scarp present at the top portion of the landslide and there are clear boundaries on either side of the slide. The boundary of the slide fans outward from the top and increases in width as the bottom of the slide is approached. On the left side of the slide, the slide boundary is defined by a large rock drainage trench that was installed to help the slide drain long before our study and data collection occurred. There is a slight bulge across the slide as one approaches the bottom of the slide. The dimensions of the slide are 140

ft. (approximately 43 m) from the top to bottom and 120 ft. (approximately 36 m) across at its widest point. The underlying bedrock consists multiple formations. The different formations that are the Kinderhookian Series, and the Cotter Dolomite. The Kinderhookian Series is a Mississippian age formation, while the Cotter Dolomite is an Ordovician age formation (Whitfield, 2004). The landslide can be seen in Figure 2.3 below. The geologic formations present can be seen on the geologic map in Figure 2.4 below, and the legend of the geologic formations can be seen in Figure 2.5.

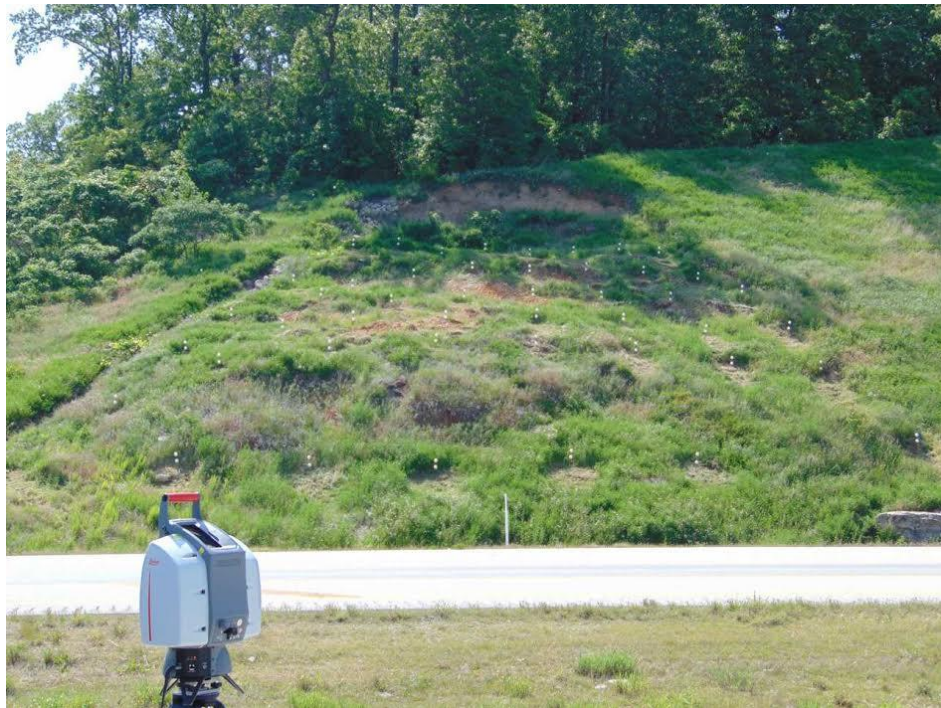


Figure 2.3. Stone County Landslide near Branson, MO



Figure 2.4. Garber Quadrangle 2004 Geologic Map 1:24000
 (Whitfield, 2004)
 (Landslide location outlined in red)

CORRELATION OF MAP UNITS

MAP UNIT SYMBOL	SYSTEM	SERIES	FORMATION(S)/MAPPABLE UNIT	THICKNESS IN FEET
Mbk	Mississippian	Osagean	Burlington Limestone	40*
Mrs	Mississippian	Osagean	Reeds Spring Formation	140 -160
Mp	Mississippian	Osagean	Pierson Limestone	40 - 60
Mk	Mississippian	Kinderhookian	Northview Formation, Compton Limestone and Bachelor Formation	5 - 30
---UNCONFORMITY---				
Oc	Ordovician	Ibexian	Cotter Dolomite	310 - 400*

* Unit is not completely exposed.

Figure 2.5. Garber Quadrangle 2004 Geologic Map Legend
 (Whitfield, 2004)

2.2 DATA COLLECTION

2.2.1 LiDAR Point Cloud Scans. Three-dimensional sets of data were collected of the landslide site in the form of point clouds. These point clouds were composed of the landslide ground surface and reflective targets placed on the landslide.

2.2.1.1 LiDAR target setup and designation. Reflective targets were placed on the stable areas of the landslide as well as the unstable areas to measure the displacement and specific movements of the landslide over time. The targets consisted of various sizes of polystyrene spheres. The actual material and geometry of the targets do not greatly affect the results of displacement and deformation tests. Due to the cheapness, durability, and availability of the material, the spherical polystyrene targets were chosen to track the movement of the landslide. The centers of these spheres can be calculated and tracked regardless of the scanner direction, as long as the laser pulse can reach the surface of the sphere and be reflected back to the scanner (Franz, 2016). These spherical targets are easy to handle and work with. In order to place these targets, steel rods were driven into multiple rows and columns throughout the slide. The length of the rod above and below the surface was measured. The spheres were then mounted to each rod using waterproof glue.

For processing and monitoring purposes, each rod was specified to be either a control rod or a floating rod and each rod was also given a number. The control rods were placed outside of the boundary of the slide and driven into stable areas. Groups of control rods were placed at the top and bottom corners as well as about halfway up the slide outside of the slide boundary. The control rods were used as reference points throughout the course of the survey campaign. Each control rod has only one 6" (152.4 mm) sphere

mounted on it. A typical control can be seen in Figure 2.6. The floating rods were placed within the slide boundary through the unstable areas of the slide. These floating rods measured the displacement of the slide using the spheres mounted on them as a proxy. The floating rods have two 4" (101.6 mm) spheres or two 4.5" (114.3 mm) spheres mounted on them. One of these spheres was mounted on the top of the rod and the other is mounted below the first sphere. The typical distance between the two spheres on each rod is about two sphere diameters (8"-9"). A typical floating rod can be seen in Figure 2.7. The addition of the second sphere on the floating rods allows for the detection of rotational movement of the rod along with translational movement on the surface and in the subsurface of the slide. Ideal visualization of these movement concepts can be seen in Figures 2.8, 2.9, and 2.10. If there is rotation detected, that specific rod could potentially have pierced the slip surface of the slide.



Figure 2.6. Typical Control Rod With 6" (152.4 mm) Target Embedded outside the Slide Boundaries



Figure 2.7. Typical Floating Target Rod with Twin 4" (101.6 mm) Targets Embedded within Slide Boundaries

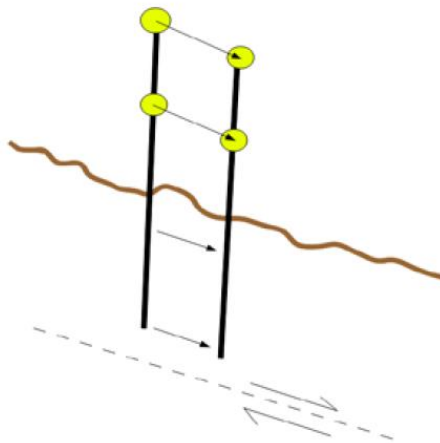


Figure 2.8. Idealized Movement of Styrofoam Spheres above a Planar Slip Surface, when the Base of the Rigid Rod is above the Shear Surface (Maerz et al., 2016)

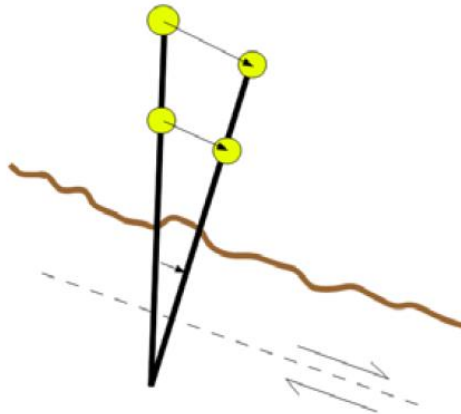


Figure 2.9. Idealized Movement of Styrofoam Spheres above a Planar Slip Surface when the Base of the Rigid Rod is below the Shear Surface (Maerz et al., 2016)

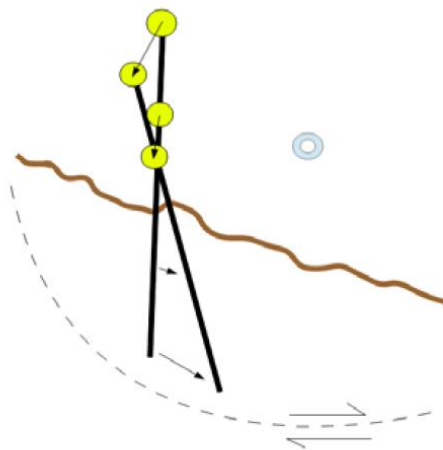


Figure 2.10. Idealized Movement of Styrofoam Spheres above a Circular Slip Surface when the Base of the Rigid Rod is above the Shear Surface (Maerz et al., 2016)

The first date of our survey campaign is referred to as the base date. The base date was July 19, 2015. On the base date 122 spheres and 71 rods were present. This includes both controls and floaters. The final date of our survey campaign was January 8, 2017. On the final date, there were 138 spheres and 79 rods present. Over the course of the survey campaign, some rods were removed from the slide and others were put in.

2.2.1.2 TLS equipment and setup. The following equipment was used to conduct the TLS survey campaign:

- Scanstation 2^{®i} from Leica Geosystems
 - Type
 - Pulsed laser
 - Range
 - Up to 300 meters (~984 feet)
 - Scan Rate
 - 50,000 pts/sec
 - Spot size
 - 4 mm @ 0-50 m
- Tripod and tribrach for TLS mounting
- Field laptop to navigate the data collection software
- Gasoline powered generator to ensure the presence of power at the site

The Leica Scanstation 2 can be seen post-setup in Figure 2.11. More information on the Leica Scanstation 2 can be found at http://hds.leica-geosystems.com/en/Leica-ScanStation-2_62189.htm.



Figure 2.11. Leica Scanstation 2 Post-setup

For each data collection session, a team of two was assembled to mobilize the equipment and venture to the slide site. A pickup truck fit all the equipment listed above and gave plenty of extra space for extra maintenance equipment and personal belongings. Once the team arrived on site, the TLS was setup as close to the base date scanning position as possible. The tripod was placed on the paved shoulder of the outer road, so that the tripod would not sink into the soil during the collection process. This location was selected because it was far enough away from the slide to keep the data collection team safe from vehicles driving on the highway, but close enough to give the Leica Scanstation 2 a sufficient range and view of the landslide. This scanning position is located about 75 m from the middle of the slide and marked with a spray painted white line. Although any deviation from this starting point is remedied during data processing, it was considered important to be as close to the base position as possible to avoid

unnecessary error. Then the tripod was set up by extending the three tripod legs to the ground surface. The legs needed to be sturdy in order to keep the LiDAR unit in the same position throughout the data collection. The position of the laser scanner can be seen in Figure 2.12. relative to the location of the landslide.

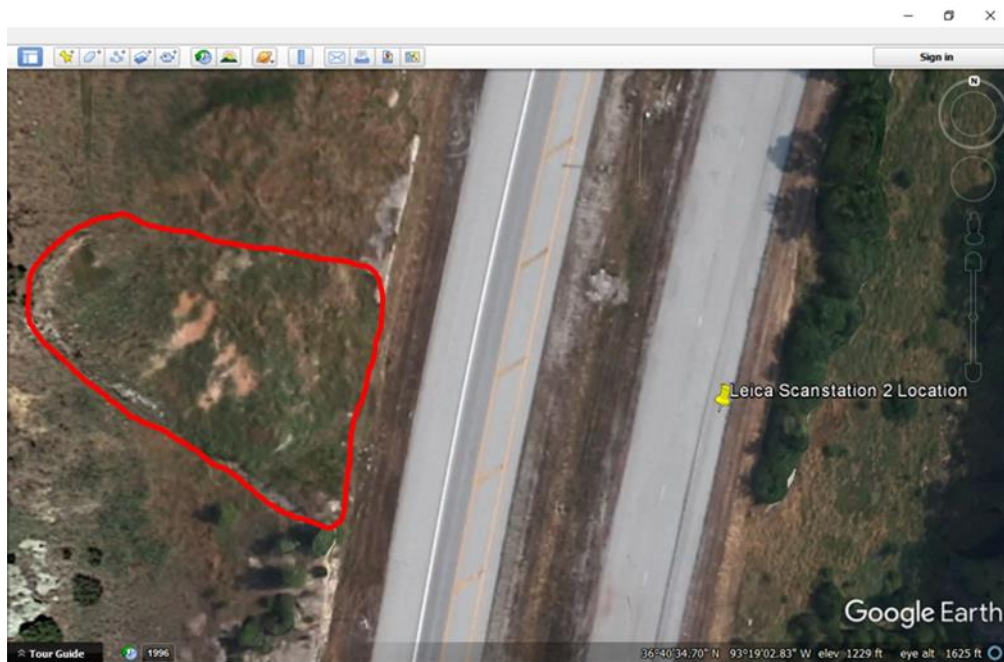


Figure 2.12. Google Earth View Scanner Position Relative to Landslide (Landslide Boundaries in Red)

After the tripod was setup on the pavement, a bubble leveling system known as a tribrach was mounted to the top. This leveling system consisted of three twisting levers that either raised or lowered that specific side of the system. The tribrach can be seen in Figure 2.13. A bubble level was present on the system to ensure that the Scanstation 2 would be properly leveled when placed on the tripod. The Leica Scanstation 2 was

removed from its container and mounted to the top of the tripod and locked into place using a three-point twist lock system on the tribrach. There was an additional bubble level located on the Scanstation 2 itself in case further leveling was needed. The front and top protective panels were removed from the Scanstation 2 to ensure the laser and camera could take measurements. The Scanstation 2 was then unlocked and allowed to spin freely. The Scanstation 2 was connected to a power source and connected to the field laptop to ensure the data could be transferred from the scanner to the field laptop. Once powered up, the Scanstation 2 ran through a startup process in which it tested all its movement capabilities to ensure that it could operate properly throughout data collection. This process took no longer than five minutes during any given survey. During the Scanstation 2 startup process, the field laptop was started and logged in to the Windows operating system. The entire data collection setup can be seen in Figure 2.14. This ended the setup process; the next step of the survey was to begin collecting data.



Figure 2.13. Tribrach Leveling System



Figure 2.14. Data Collection Equipment after Setup

2.2.1.3 Data collection. The software package used to navigate and collect the LiDAR data was Leica Cyclone[®]. Leica Cyclone is one of the market-leading point cloud processing software packages created and developed by Leica Geosystems. The particular version that was used over the course of our study was Version 7. Cyclone allowed for simple data logging as well as the ability to inspect the point cloud and other types of data before moving on to another scan or before leaving the site. The data collection software was navigated using an Argonaut OEM D15R-Series field laptop with sunlight readable display screen as a user interface which can be seen in Figure 2.15.



Figure 2.15. Argonaut OEM D15R-Series Field Laptop

Cyclone allows the user to select multiple parameters that are used by the Scanstation 2 during a scan. These parameters composed of project setup parameters, resolution parameters, and probe parameters. These can be seen in Figure 2.16 and Figure 2.17 during project selection and creation. The Cyclone software also allows the user to capture a color image of the scanning view prior to the start of the scan. This imaging process can be seen in Figure 2.18 and Figure 2.19.

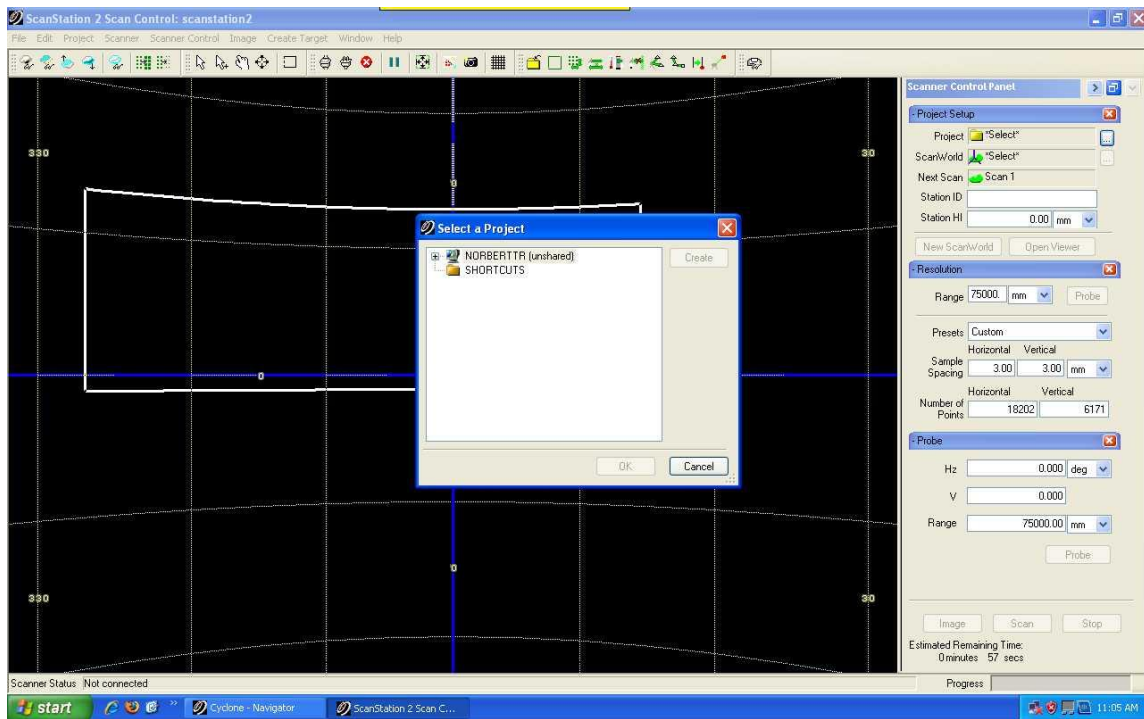


Figure 2.16. Cyclone Project Selection/Creation

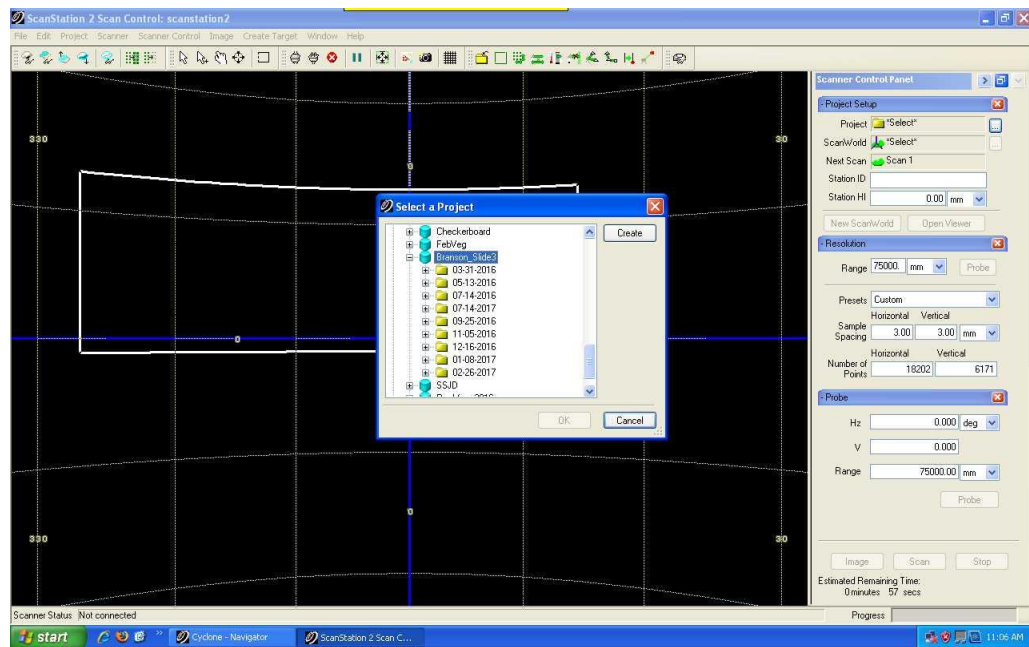


Figure 2.17. Cyclone Project Selection/Creation

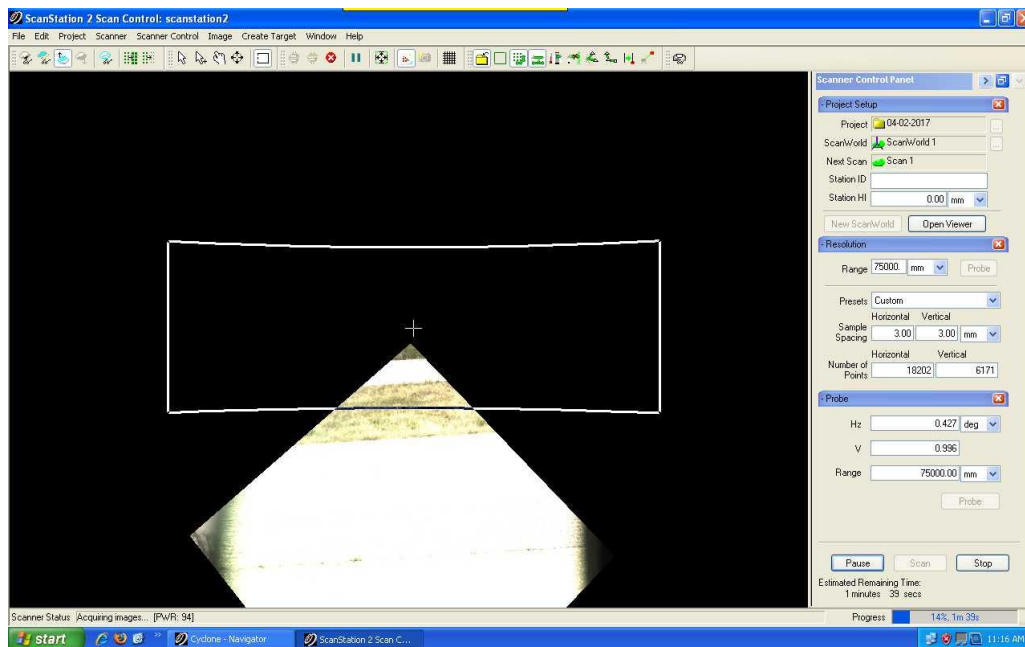


Figure 2.18. Beginning of Imaging Process

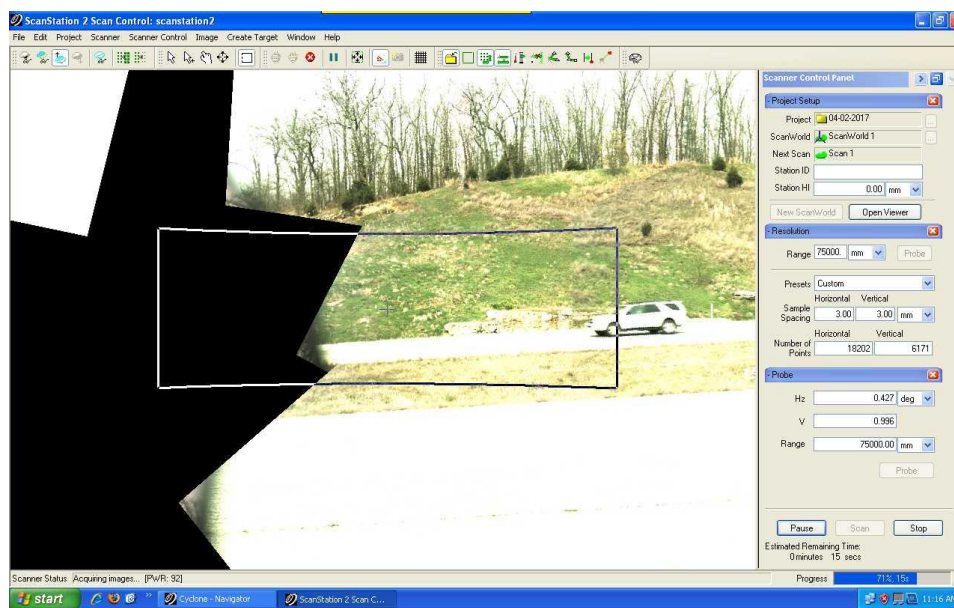


Figure 2.19. Cyclone Imaging Process

After creating a project that corresponds to the specific date of the scan, connecting to the laser scanner, imaging the slide, and selecting the proper parameters, a virtual fence is drawn around all present rods to limit the area scanned. Now the scan can be initiated. The beginning of the scanning process and the virtual fence can be seen in Figure 2.20. The time to complete each scan was approximately 60 to 90 minutes. This completion time is based on the resolution parameters and the size of the virtual fence.

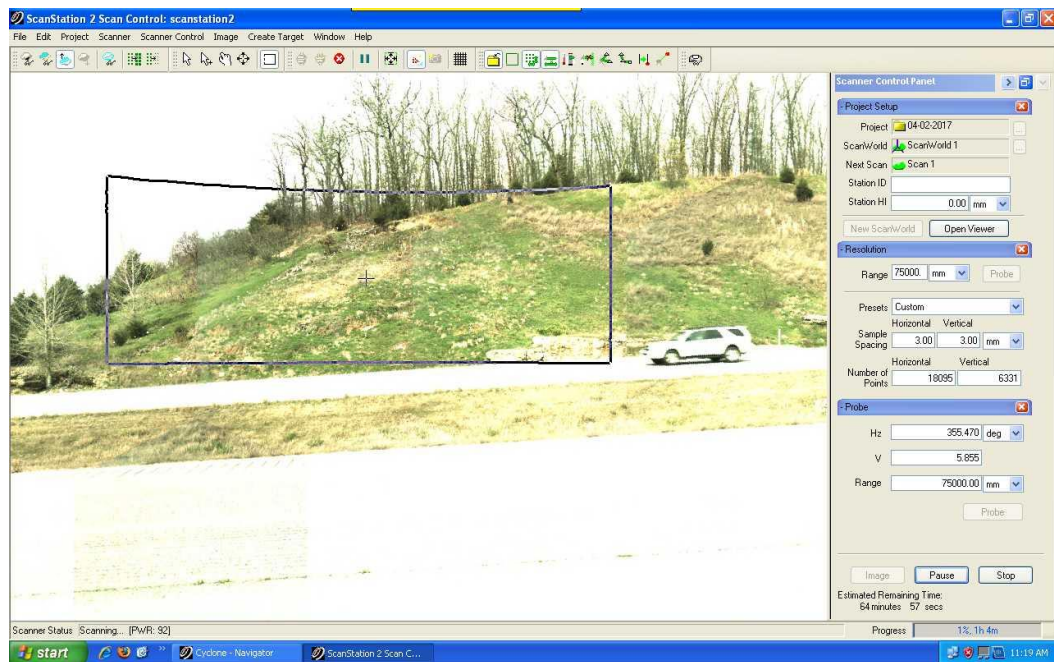


Figure 2.20. Cyclone Fencing/Scanning Process

As can be seen in Figure 2.20, the sampling interval that was used over the course of the study was 3 mm by 3 mm at a distance of 75 m. This allowed for the collection of about 1000 points per sphere leading to precise measurements of the location of each sphere. A resolution test was performed on similar spherical targets that were used at the

landslide to determine the appropriate number of returns needed on each sphere to properly calculate the center. This resolution test was performed at the Rock Mechanics and Explosives Research Center in the second-floor hallway. Eight spheres of varying sizes were placed at one end of the hallway and the Scanstation 2 was placed at the other end. Four spheres had 4.5 in. diameters, three spheres had 4 in. diameters, and one sphere had a diameter of 6 in. The distance between the Scanstation 2 and the spheres was 36 m (~118 ft.). The exact configuration of the spheres is shown in Figure 2.21.



Figure 2.21. Resolution Test Sphere Configuration

Scans were performed at varying resolutions to determine the optimal resolution needed for determining sphere centers. These scan resolutions were 1 mm, 2 mm, 3 mm, 5 mm, and 10 mm. Three scans were performed for each resolution for a total of fifteen scans. Each of the spheres were labeled as control points and processed through our self-developed software. Each scan's three-dimensional root mean square error was compared with every other scan for a total of 105 comparisons. It was found that having more than 1000 point values per sphere does not greatly increase the quality of the three-dimensional root mean square error. The three-dimensional root mean square error gives a sense of the resolution that is attained in the scan. The smaller root mean square error in this test means a higher resolution was attained. This means that having more than 1000 points per sphere does not give a more precise center calculation. Due to this data, it was determined that while collecting data at the Branson slide site a sampling interval of 3 mm by 3mm at a distance of 75 m from the slide attains around 1000 points per sphere. The typical scanning time at this resolution and distance was between 60 and 90 minutes. This saves considerable amounts of time compared to a sampling interval of 2 mm or 1 mm. The average distance of the Scanstation 2 to any point on the slide was about 75 m, so the input into the probing distance on the Cyclone software was 75,000 mm. The results of this test are presented in Table 2.1.

Table 2.1. Sphere Resolution Test Results

Scan Resolution (mm)	Average Root Mean Square Error
1	0.512
2	0.331
3	0.435
5	0.530
10	1.069

Maintenance was performed at the site on a regular basis to ensure that the best possible data was being collected. During the spring and summer months, the vegetation on the slide saw considerable growth. All the vegetation, if large and invasive enough, has the potential of getting in the way of the laser path. This can cause inaccuracies in the acquisition of data and may lead to incorrect measurements of sphere position. These inaccuracies are caused by the laser pulse back scattering and hitting a piece of vegetation rather than the actual sphere. During the course of the study, we employed the use of shears and a weed whip to keep the growth of the weeds near the spheres and rods under control. It was also necessary to make sure that each rod present on the slide was still in good condition and had good contact with the ground and subsurface. This was to ensure that the rods were moving in reference to the surface and subsurface. Over the course of the study, some rods were uprooted or had so much movement that they became near parallel to the slide surface. If the rods had been uprooted or had so much rotational movement that they became near parallel to the slide surface and were no longer able to be tracked, a new rod was placed as close as possible to the original rod's position in order to continue measuring the displacements of that area.

2.2.2 Geophysical Survey. A geophysical survey was conducted on November 5, 2016 to observe the subsurface conditions of the slide and correlate other data collected on the slide. Two graduate students in the Geophysics program brought along equipment to perform multiple profile tests using Electrical Resistivity Tomography (ERT). Three separate profiles were analyzed: one down the north side of the slide, one down the middle of the slide, and one down the south side of the slide as shown in Figure 2.22. These profiles were collected from west to east, which is from the top of the slope to the bottom of the slope. The team cleared vegetation from each lane to make it easier to drive each stake into the slide surface and connect each electrode to these metal stakes. Each test took about ninety minutes to complete. The setup of the ERT profiles and equipment can be seen in Figure 2.23, 2.24, and 2.25. The ERT data was acquired using an AGI SuperSting R8 multichannel electrode system which can be seen in Figure 2.26. During data acquisition, electrodes were spaced at 2 ft. (0.6 m) intervals covering a length of approximately 150 ft. (48 m) for each profile. A dipole-dipole array was utilized in this survey.



Figure 2.22. Plan View of ERT Profiles



Figure 2.23. Setup of Profile 1 (North Side of Slide)



Figure 2.24. Setup of Profile 2 (Middle Part of Slide)



Figure 2.25. Setup of Profile 3 (South Side of Slide)



Figure 2.26. AGI SuperSting R8 Multichannel Electrode System

2.2.3 General Surface Mapping. A surface map of the slide was created using satellite imagery obtained from Google Earth and on site visual observation and measurements. An image of the slide from March 2015 was obtained from Google Earth. Visual and physical measurements were conducted on January 8, 2017. The head scarp of the slide was measured to be between 56 and 65 in. high. The drainage trench on the south side of the slide is 11 ft. at its widest point. There were not distinguishable tension cracks on the boundary lines of the slide due to dense vegetation. Some divots towards the top middle portion of the side were distinguishable and could be due to slide movement. Different areas were labeled on the map due to their topography and vegetation cover. The map and corresponding legend can be seen in Figure 2.27.

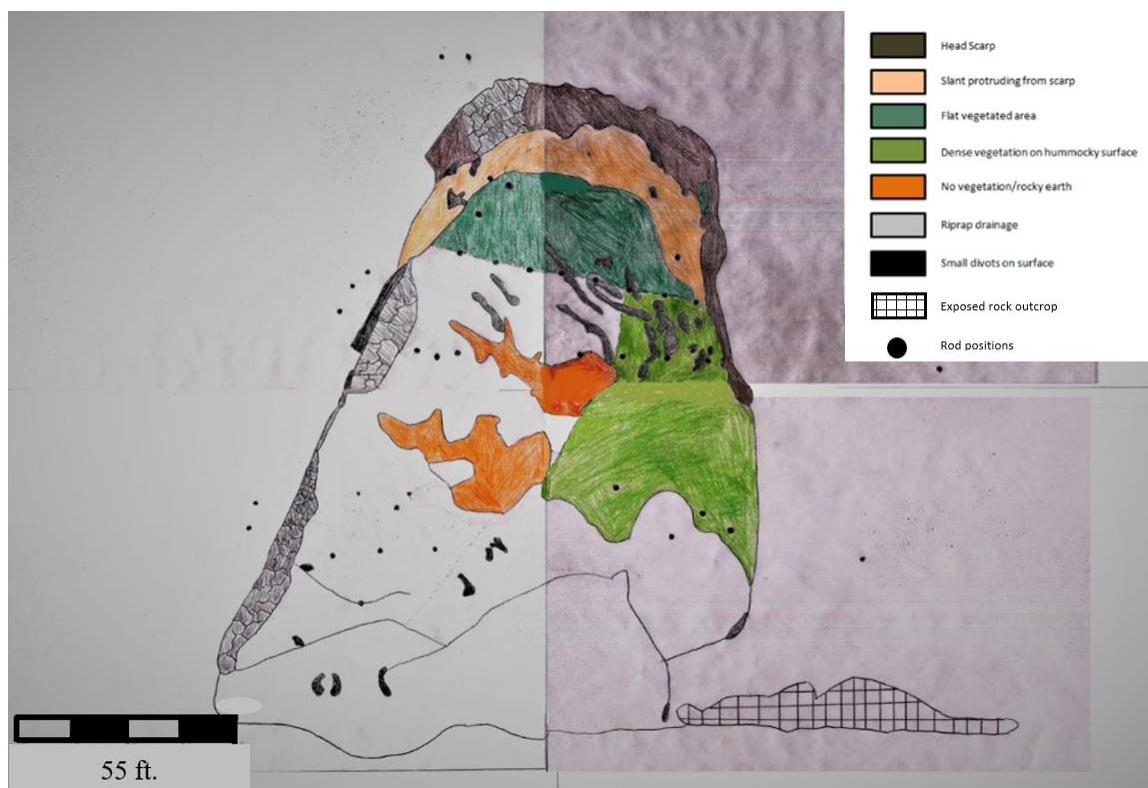


Figure 2.27. Ground Surface Map

2.3 LIDAR POINTCLOUD AND SPHERE CENTER DATA PROCESSING

2.3.1 Pre-processing and Data Exporting. After the point cloud data was collected and visually inspected to make sure that the scanner had collected the correct field of view, each scan was exported to an external hard drive and saved in a PTS file format. PTS files are text files that represent each point with seven parameters. These parameters are the x, y, and z coordinate of each point, along with the intensity return and the R, G, and B color value of the point. Each scan of the slide consisted of anywhere between 60 and 70 million points contained in the point cloud. These point files can contain rather large amounts of data. The sizes of these files ranged from 3 to 5 GB in size before processing. The PTS files of the scan are saved to a specific directory in the

external hard drive or to a separate computer to begin processing. Software developed for this project consists of various programs that the data sets are run through. Data sets are saved to specific directories in the user's hard drive. The PTS files must be saved in the "OutcropData" directory under the specific site of the particular scan. The "OutcropData" directory and its contents can be seen in Figure 2.28. Each site has a specific number attached to it. The Branson Slide was designated Site 6 and all data from that specific site is saved in the "OutcropData" directory under the folder "Site6". The PTS files are saved in the "pointfiles" directory within the "Site6" folder. This is shown in Figure 2.29. The software that we use to process the PTS files collected from the scanning of the Branson slide was developed specifically for spherical target processing research by Kenneth Boyko, a PhD candidate at Missouri University of Science and Technology. The software suite and its components are known as and will be referred to as lidarsw. The specific version of the software used is research-oriented. The procedure and result of each program will be described.

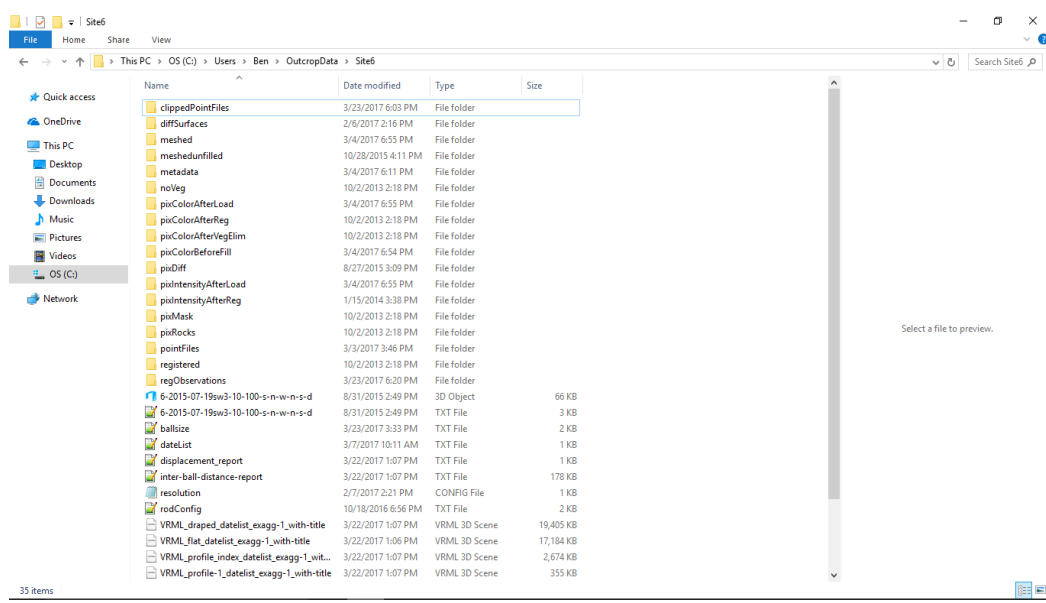


Figure 2.28. OutcropData Directory

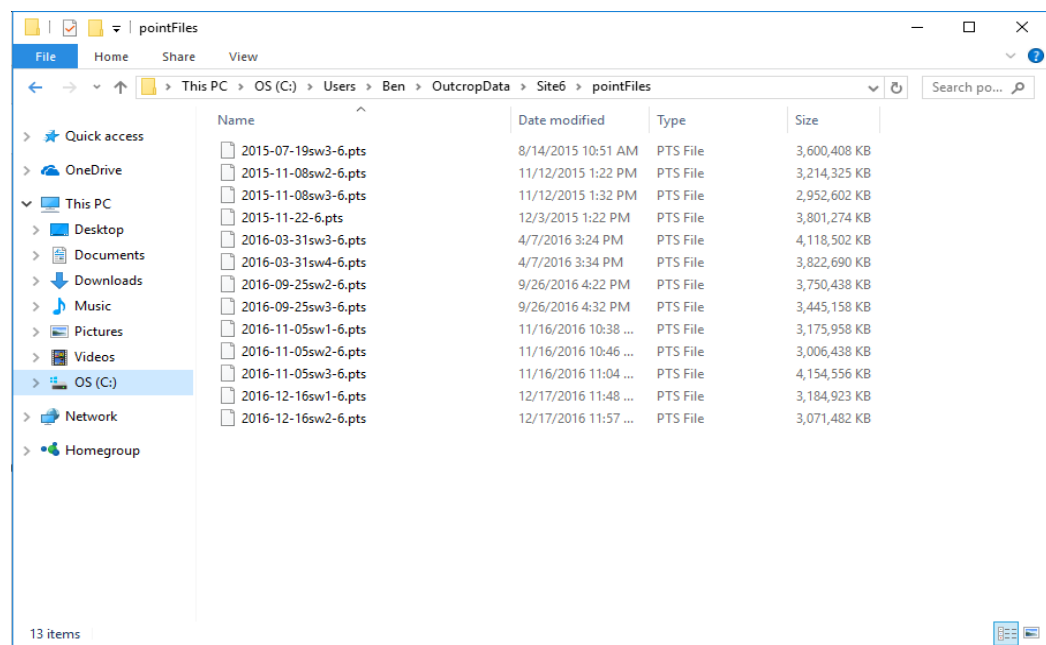


Figure 2.29. Location of Pointfiles within the Specific Site6 Directory

The operating environment of lidarsw is a terminal based system and uses the command prompt desktop application to run programs and utilities. The initial terminal can be seen in Figure 2.30.

The first step in processing the data after it has been exported from Cyclone on the field laptop to an external hard drive or a separate computing system is to open the command prompt application from the Windows Start menu or another command-line interpreter.

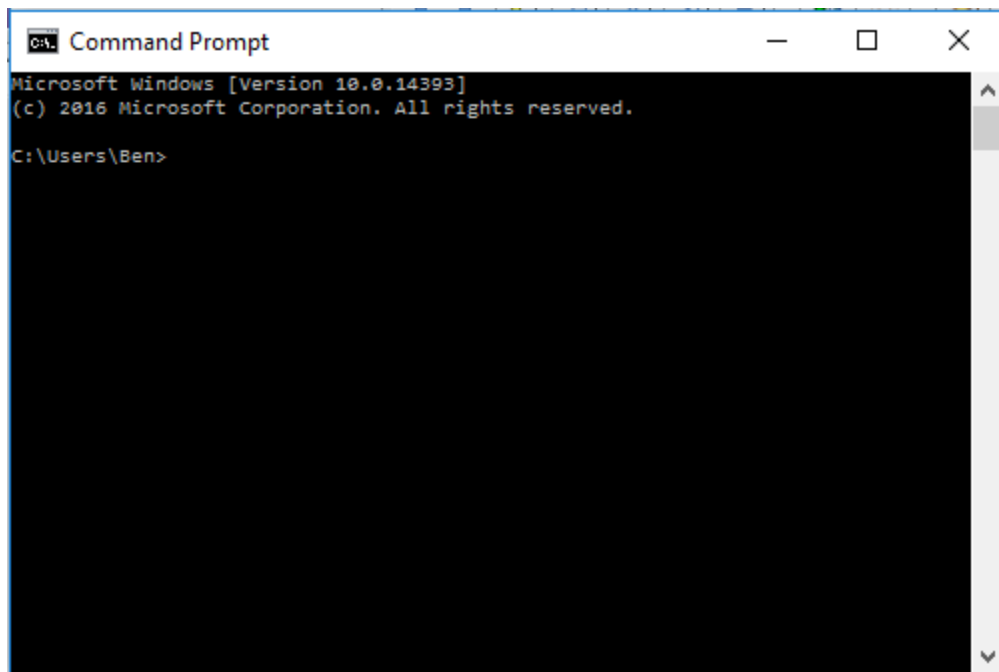


Figure 2.30. Initial Command Prompt Window

The next step in processing the data is to change directories from the “Username” directory in the to the “lidarsw” directory. The “cd lidarsw” command will change the

directory to the lidarsw directory in order to begin running the programs necessary to process the point cloud data. This input can be seen in Figure 2.31.

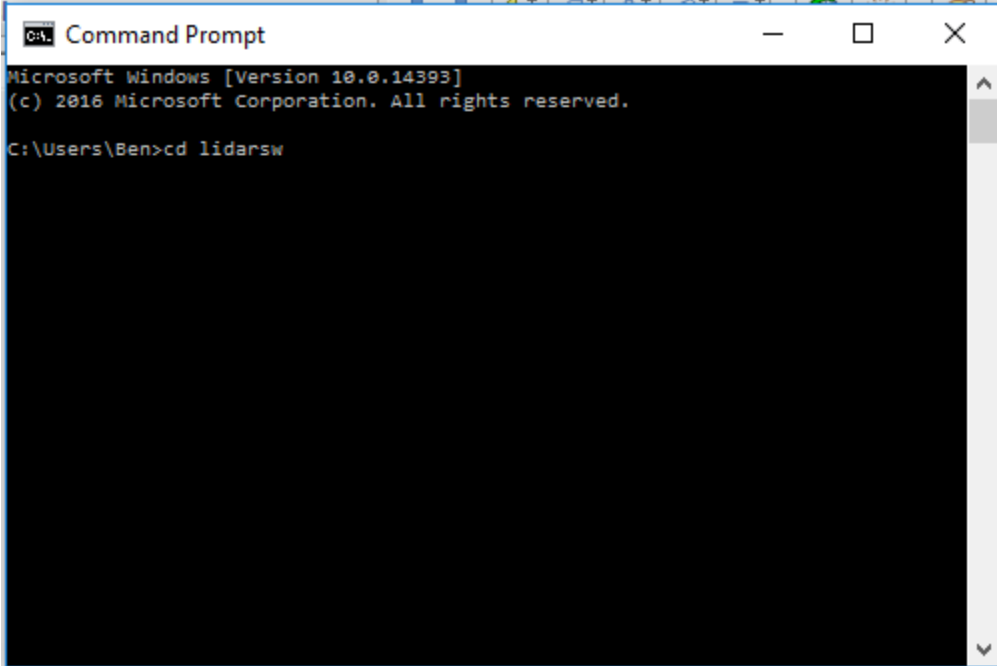
A screenshot of a Windows Command Prompt window. The title bar reads "Command Prompt". The window content shows the following text: "Microsoft Windows [Version 10.0.14393] (c) 2016 Microsoft Corporation. All rights reserved. C:\Users\Ben>cd lidarsw". The command prompt is currently at the end of the line "C:\Users\Ben>cd lidarsw".

Figure 2.31. Input of the “cd lidarsw” Command

2.3.2 FindMinMax Program. After the directory has been changed to the lidarsw directory true processing begins. The first program that is run is called “FindMinMax”. This program looks through a specific PTS file and establishes the minimum and maximum extents of the x, y, and z coordinates in the pointfiles. The program also establishes the minimum and maximum extent of the horizontal and vertical coordinates in the field of view. These extents of the x, y, and z coordinates as well as the extents of the horizontal and vertical coordinates are coupled with a user-selected mesh

resolution to build metadata which is used by later programs. This mesh is an array made up of individual cells. These cells divide up the field of view in order to populate it with specific values. In order to run the program, the name of the program must be input into the command prompt terminal followed by the site number, in our case 6, and the specific date which includes the pointfiles in a year-month-day format.

The “FindMinMax” program apart from using the pointFiles, also uses a resolution configuration file, setup as a text file, which is comprised of eight separate features:

- The mesh resolution. In most of our processing the resolution was between 14 and 18 mm
- The unit multiplier
 - The Leica Scanstation 2 collects distance measurements and coordinate measurements in units of millimeters. This unit multiplier can be changed if the user wants to process the data in a different unit.
- An Image option which allows the points to be colored in the form of RGB values
 - The color image option was turned on for our study due to the Scanstation 2 having the ability to collect color images
- A Map option, which designated either a ground plane or a spherical option
 - The spherical option was chosen to make identifying specific spheres easier
 - The spherical option gave a head-on view of the slide rather than a plan view of the slide in later processing steps
- A specific number of pointfiles option

- Each PTS file was processed through the programs one at a time so this number remained 1 throughout the processing
- A multi-hit option of lowest, highest, or average
 - This option is used if there are multiple LiDAR returns in one cell; the value that will be given to the specific cell. This option was set to take the average of the values for the length of the study
- The probing distance in millimeters
 - This is the value of the distance from the LiDAR to the middle of the slide area in millimeters, this was set to 75000 over the course of the study
- A z offset
 - This was set to zero for the Scanstation 2

The FindMinMax program determines the extent of the x, y, and z coordinates are within the bounds of the processing limits of the rest of the lidarsw programs. The maximum dimensions of the generated grid can be horizontally 4300 units and vertically 3400 units. If the extents of the coordinates are within those bounds, and no other problems occur during the running of the FindMinMax program, the metadata is then saved in the metadata directory within the OutcropData directory. The FindMinMax program is run through the command terminal as shown in Figure 2.32.

```

Command Prompt - findminmax 6 2017-01-08sw1
C:\Users\Ben\lidarsw>findminmax 6 2017-01-08sw1
external drive name: C:/Users/Ben/
opening: C:/Users/Ben//OutcropData/Site6/resolution.config
determining min max for raw lidar points site: 6 date: 2017-01-08sw1
cellRes: 14
unitMult: 1
imgOption: c
mapOption: s
numPointFiles: 1
multiHitOption: f
givenProbe: 75000
zOffset: 0
external drive name: C:/Users/Ben/

before loading - determining min-max for file: C:/Users/Ben//OutcropData/Site6/pointFiles/2017-01-08sw1-6.pts
cell res: 14
unitMult: 1
imgOption: c
mapOption: s
numPointFiles: 1
skipping this line (count for next scan in this pts file) : 58847094
first 5 points: 0 x: -29679.4 y: 54873.3 z: -166.604 brightness: -1679 r: 36 g: 38 b: 27
first 5 points: 0 x: -29694.5 y: 54902 z: -150.378 brightness: -1518 r: 34 g: 35 b: 27
first 5 points: 0 x: -29696.1 y: 54904.9 z: -148.494 brightness: -1716 r: 34 g: 35 b: 27
first 5 points: 0 x: -29688.8 y: 54891.4 z: -144.124 brightness: -1674 r: 34 g: 35 b: 27
first 5 points: 0 x: -29686.4 y: 54887 z: -139.503 brightness: -1389 r: 34 g: 35 b: 27
in findMinMax numpts: 1000000

```

Figure 2.32. Initial Running of the FindMinMax Program

2.3.3 Load Program. After the data has been processed through FindMinMax program, it is then processed through the “Load” program. This program transforms the PTS file of a scan into a binary data file that is used by the rest of the processing programs. This program also spatial orders the data in a readable fashion since the Scanstation 2 orders the data randomly during data collection. It uses the information gained from the metadata file created by the FindMinMax program in order to complete this process. The Load program decides which cell in the mesh that a specific point should be loaded in, and then assigns those point values and information to that specific cell. The information that is present with each point is position, intensity value based on the material, and color, which is retrieved if an image was taken by the Scanstation 2 before scanning.

This program goes through each of the 60 million to 70 million points and the processing time is based on the computing power of the system being used. When the Load program is almost complete, the program looks for any spots in the mesh of cells that have no data points retrieved from the point cloud. These empty cells are filled using a search mechanism performed by the Load program. The Load program looks for paired neighbors starting at 0 and 180 degrees azimuth. Then it rotates five degrees and looks for any paired neighbors on that azimuth. It continues to do this until the entire surrounding area has been searched. The neighbored pairs that have the minimum distance to the empty cell is used. From those neighbored pairs a linear interpolation is conducted to determine what information to load into the empty cell. Only originally loaded cells are used in this search process. The Load program being run can be seen in Figures 2.33 and 2.34.

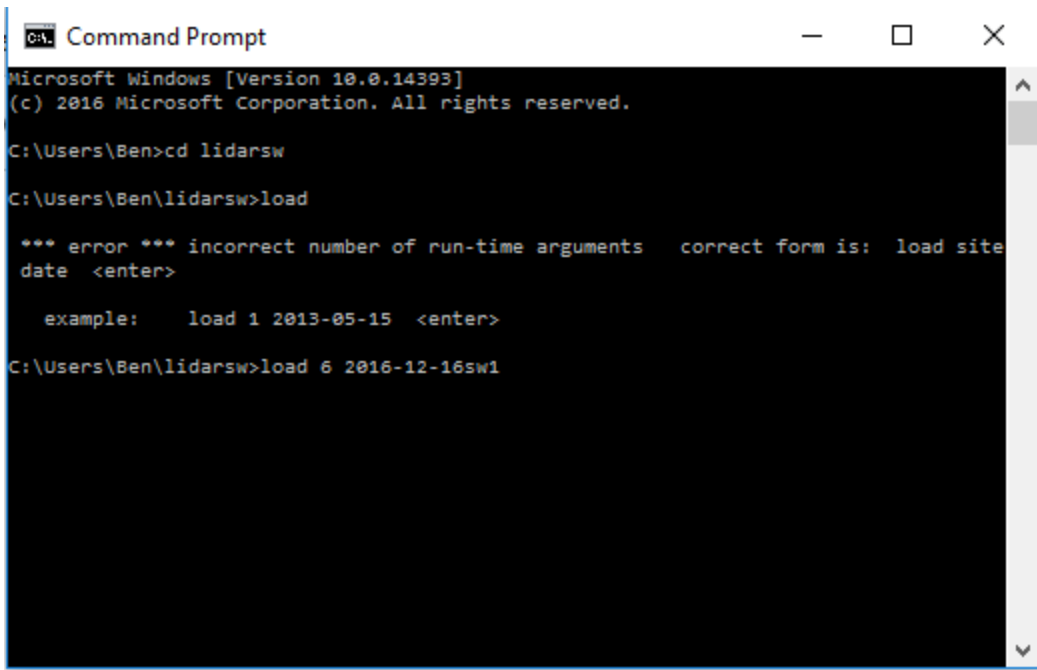


Figure 2.33. Load Prior to Running the Program

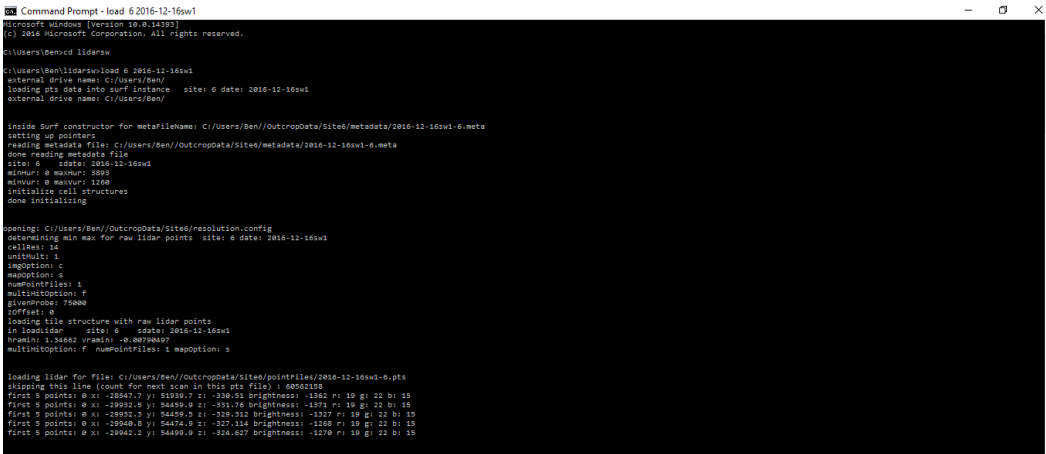


Figure 2.34. Initial Running of the Load Program

After the Load program is finished running, it compiles binary files and deposits them in the “meshed” directory and it also sends specific images, whether they are

intensity or color images, to other directories in the “OutcropData” directory. These images can be seen in Figures 2.35, 2.36, 2.37, 2.38.

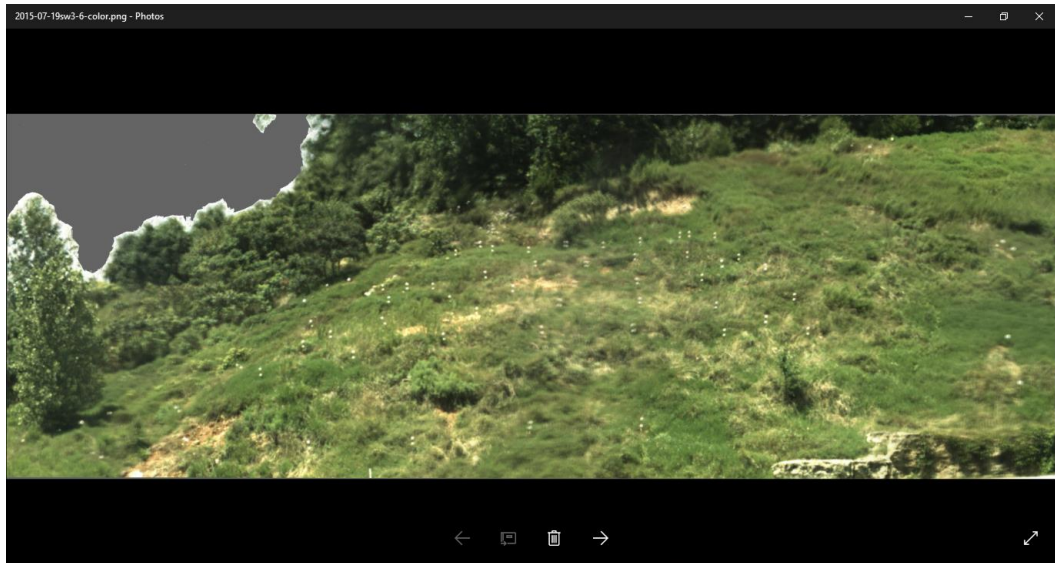


Figure 2.35. July 19, 2015 Color Image Generated by the Load Program



Figure 2.36. December 16, 2016 Color Image Generated by the Load Program



Figure 2.37. July 19, 2015 Intensity Image Generated by the Load Program



Figure 2.38. December 16, 2016 Intensity Image Generated by the Load Program

2.3.4 View2surf Program. After each cell in the mesh has the proper information the user can now view the surface and begin to point on each spherical target.

The program that performs this function is known as the view2surf program. This program allows the user to view two different surfaces side by side to compare and annotate them. These surfaces are generated using the information gained from the FindMinMax and Load programs. The view2surf program is used to assign manual pointings to each sphere for the next program to look for the points on each sphere. Each sphere is given a type, either a control sphere or a floating sphere. Control spheres are designated by a letter "C" followed by a dash and a specific number. Floating spheres are designated by a letter "F" followed by a dash and a specific number. The spheres are indexed this way every time that a data set is analyzed and processed. Floating spheres were accompanied by the second sphere on the same target rod, so the number of those partner spheres are adjacent in value (for example, F-233 and F-234 are mounted on the same rod). While viewing the surfaces control designators show up in the color green and floating designators show up in red when viewing the surfaces. These surfaces and designators can be seen in Figures 2.39 and 2.40. When manually pointing to each sphere, view2surf pairs the horizontal, vertical, and x, y, z coordinates with the specific designator (i.e. F-233 or C-151). This can be seen in Figure 2.41. This information is then written to a text file called a manual surface file, which is specific for each scan, and it is stored in the "regObservations" directory. This manual surface file is used during later data processing.


```
*** base offset point set h,v: 1810 707 xyz: -7950.72 69576 8739.86 base surface dist: 70572.1
*** base offset point set h,v: 1616 517 xyz: -4706.99 60561.2 5401.85 base surface dist: 60983.6
*** base offset point set h,v: 1973 411 xyz: -8413.69 57939.5 4040.79 base surface dist: 58686.5
```

Figure 2.41. Point Set of Horizontal, Vertical, and x, y, z Coordinates

The lowest number sphere is manually pointed out and designated first. When a certain designation number is selected during the viewing process, the letter and number is presented as orange, rather than green or red. This can be seen in Figure 2.42. Cycling through each designator can be done by pressing “+” or “-“ on the keyboard. The plus key cycles to the next largest designator by number and the minus key cycles to the next smallest designator by number. If the designator is not on a specific sphere then it can be moved by using the arrow keys on the keyboard. Up pans up one cell, down pans down, left pans left, and right pans right. The intensity plot gives the best contrast between the white polystyrene sphere and the darker background of the ground surface. This allows for better observation of the location of each sphere. After each control sphere and each floating sphere is paired with a designator it is time to move on to the next processing step. These designators are kept on the same spheres throughout the study to track and record specific spheres.

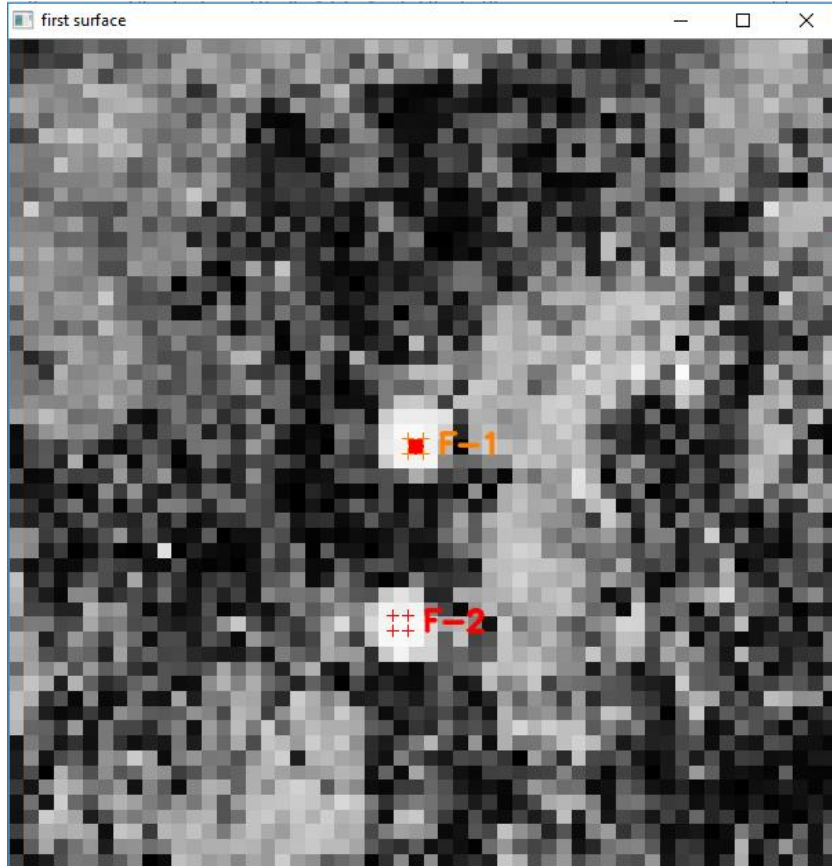


Figure 2.42. Specific Designator Selected in View2surf

2.3.5 ClipSpheres Program. The next program that the data is run through is called ClipSpheres. This program effectively removes all the points in the data that are not a return from a sphere. The program uses the information from the manual surface files to look for what points lay on a sphere. This input information can be seen being used in Figure 2.43. This makes further processing much less time consuming and more efficient. The ClipSpheres program uses a sphere or ball identification number, same as the designator, as well as the physical diameter of that specific ball to clip out all points that are not located on a sphere. Then the program writes these points to a WRL file for each sphere and saves it in the “clippedPointFiles” directory. The user can view these

clippedPointFiles to see the number of returns on each sphere. An example of this view is in Figure 2.44.

```
Command Prompt
ballType: f ballH: 3009 ballV: 271 surface xyz: -19380.6 55210.4 2504.43
center xyz: -19397.4 55258.3 2506.61

ballType: f ballH: 2904 ballV: 378 surface xyz: -19022.2 57789.3 3822.6
center xyz: -19040 57843.5 3826.18

ballType: f ballH: 2895 ballV: 367 surface xyz: -18971.4 57962.8 3706.25
center xyz: -18989.2 58017 3709.72

ballType: f ballH: 2877 ballV: 476 surface xyz: -20789 64245.5 5484.38
center xyz: -20804.6 64293.7 5488.49

ballType: f ballH: 2862 ballV: 467 surface xyz: -20631.7 64374.1 5376.1
center xyz: -20647.2 64422.4 5380.13

ballType: f ballH: 2785 ballV: 449 surface xyz: -18034.1 59182.7 4711.25
center xyz: -18048.8 59231.1 4715.11
```

Figure 2.43. Example of the ClipSpheres Input Data

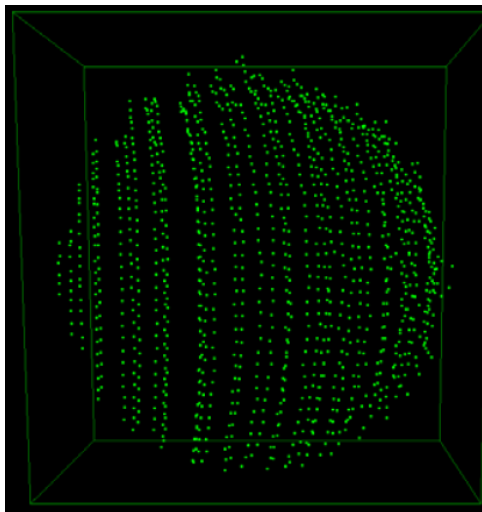


Figure 2.44. WRL File View of ClippedPointFiles

2.3.6 FindSpheres Program. Now that the lidarsw suite has filtered out all the points that do not lie on a spherical target, the next program can use the remaining points to calculate the centers of the spherical targets. FindSpheres runs through an iterative process on finding each sphere's center based on all the values of the returns from those spheres. The program uses the clipped pointfiles, ball identification, and a ball size file to complete this process. This process can be seen in Figure 2.45. FindSpheres then further refines the best center by using the best standard deviation of the points on the sphere from the calculated center point and this can be seen in Figure 2.46. These centers are written to a text file in the form of x, y, and z coordinates. These text files are called center manual files. These center manual files are saved in the "regObservations" directory along with the manual surface files. Each scan has a specific center manual file attached to it.

```

Command Prompt
*****
*****
manual pointing for ball: 1 manual-surface h,y: 1845 937
ball: 1 manual-surface h,y: 1845 937  surface x,y,z: 9540.92 85344.7 14834.4
now determining the refined center of the ball

in findSphereCenter surface xyz: 9540.92 85344.7 14834.4
ball target radius: 57.15 ballHorizRadius: 1.45947 ballVertRadius: 0.171053
ballTargetRadiusRA: 0.000491835

***** ball extended center based on manual-surface pointing and given radius: 9547.18 85400.7 14844.1

base PTS file to be examined to load prelimPTS: C:/Users/ben/OutcropData/Sites/clippedPointfiles/2016-11-05sw2-0.pts mmult: 1
pointfileCount: 100000 sphere points so far: 0
examination of base PTS file complete  number of points clipped from pts file: 670 points in clipped pointfile: 189366
about to return from findStartingPoint  stx,sty,stri: 9536.39 85399.9 14835.5
in calculateCenter with step: 10 best center: 9536.39 85399.9 14835.5
in calculateCenter with step: 7 best center: 9536.39 85399.9 14842.5
in calculateCenter with step: 4.9 best center: 9536.39 85403.8 14842.5
in calculateCenter with step: 3.43 best center: 9536.39 85400.4 14839.1
in calculateCenter with step: 2.401 best center: 9536.39 85399.7 14840.4
in calculateCenter with step: 1.6807 best center: 9536.39 85399.7 14840.8
in calculateCenter with step: 1.17649 best center: 9536.39 85399.7 14839.6
in calculateCenter with step: 0.823543 best center: 9536.39 85399.7 14840.4
in calculateCenter with step: 0.57648 best center: 9536.39 85400.1 14840.4
in calculateCenter with step: 0.403536 best center: 9536.39 85399.8 14840
in calculateCenter with step: 0.282475 best center: 9536.39 85399.5 14840
in calculateCenter with step: 0.197733 best center: 9536.39 85399.7 14840.2
in calculateCenter with step: 0.138413 best center: 9536.39 85399.7 14840.1
in calculateCenter with step: 0.096889 best center: 9536.39 85399.7 14840.2
in calculateCenter with step: 0.0692023 best center: 9536.39 85399.7 14840.1
in calculateCenter with step: 0.0474756 best center: 9536.39 85399.7 14840.1
in calculateCenter with step: 0.0323239 best center: 9536.36 85399.7 14840.1
in calculateCenter with step: 0.022631 best center: 9536.36 85399.7 14840.1
in calculateCenter with step: 0.0162841 best center: 9536.36 85399.7 14840.1
in calculateCenter with step: 0.0119889 best center: 9536.37 85399.7 14840.1

***** calculated center point: 9536.37 85399.7 14840.1

```

Figure 2.45. FindSpheres Calculating the Best Fit Centers

```

Command Prompt

***** calculated center point: 9536.37 85399.7 14840.1
best standard deviation: 1.69328
before first call to examineAllBallPts
minDist: 53.2042 maxDist: 63.1706 range of distances (fuzz depth): 9.96642 avgDist: 58.209
iDist: 53 count: 1
iDist: 54 count: 5
iDist: 55 count: 28
iDist: 56 count: 76
iDist: 57 count: 126
iDist: 58 count: 136
iDist: 59 count: 149
iDist: 60 count: 89
iDist: 61 count: 44
iDist: 62 count: 14
iDist: 63 count: 2
about to return from examineAllBallPts
after first call to examineAllBallPts
before first call to refineBallList      numpts: 670
after refining, numpts: 498
about to return from findStartingPoint  stx,sty,stri: 9536.83 85397.9 14836
in calculateCenter with step: 10 best center: 9536.83 85397.9 14836
in calculateCenter with step: 7 best center: 9536.83 85404.0 14843
in calculateCenter with step: 4.9 best center: 9536.83 85400 14838.1
in calculateCenter with step: 3.43 best center: 9536.83 85400 14841.5
in calculateCenter with step: 2.481 best center: 9536.83 85400 14839.1
in calculateCenter with step: 1.8807 best center: 9536.83 85400 14840.8
in calculateCenter with step: 1.17649 best center: 9536.83 85400 14839.6
in calculateCenter with step: 0.823543 best center: 9536 85400 14840.5
in calculateCenter with step: 0.57648 best center: 9536.58 85399.5 14839.9
in calculateCenter with step: 0.403336 best center: 9536.11 85399.9 14839.9
in calculateCenter with step: 0.282475 best center: 9536.46 85399.9 14840.2
in calculateCenter with step: 0.197733 best center: 9536.26 85399.7 14840
in calculateCenter with step: 0.138413 best center: 9536.26 85399.8 14840.1
in calculateCenter with step: 0.096889 best center: 9536.36 85399.8 14840.1
in calculateCenter with step: 0.0678223 best center: 9536.36 85399.7 14840
in calculateCenter with step: 0.0474756 best center: 9536.31 85399.8 14840.1
in calculateCenter with step: 0.0332329 best center: 9536.34 85399.7 14840
in calculateCenter with step: 0.0233631 best center: 9536.32 85399.7 14840
in calculateCenter with step: 0.0162841 best center: 9536.34 85399.8 14840.1
in calculateCenter with step: 0.0113989 best center: 9536.32 85399.8 14840.1

*** (refined) *** calculated center point: 9536.32 85399.8 14840.1
best standard deviation: 1.06507
before second call to examineAllBallPts
minDist: 56.1843 maxDist: 60.2662 range of distances (fuzz depth): 4.08194 avgDist: 58.225
iDist: 56 count: 24
iDist: 57 count: 120
iDist: 58 count: 140
iDist: 59 count: 150
iDist: 60 count: 64
about to return from examineAllBallPts
after second call to examineAllBallPts
refined ball center: 9536.32 85399.8 14840.1

file containing refined xyz centers: C:/Users/Ben/OutcropData/Site6/regObservations/center-manual-2016-11-09sw2.txt

```

Figure 2.46. FindSpheres Refining Best Fit Centers

2.3.7 Regballs Program. Now that the centers of each sphere are known, each sphere's position needs to be changed to the reference system of the base date. This process is known as registration. When all the sphere centers are in the reference system of the base date, the displacements and rate of movements of each sphere can be calculated. It further gives an indication on where the slide is moving, how fast it is moving, and whether there is any rotational movement present within the slide. The program that performs this processing step is called regballs. It compares all of the x, y, and z coordinates of the best fit centers from any two scans specified. The program running through this comparison can be seen in Figures 2.47 and 2.48. The output of this program is a "regballs report" which is saved to the "regObservations" directory. The

regballs report compiles and presents a multitude of results from the two-scan comparison. The two main sets of data that are presented are the control point transformation statistics and the displacements of the floating spheres. An example of this readout can be seen in Figure 2.49.

```
Command Prompt
***** Summary of spherical target statistics *****
3-D rms: 26.4289 mm      number of control points: 37
apparent displacement of lidar between base and later scans: 192.122 mm ( @-0.58021 feet)
apparent displacement (feet) in x: -0.635827 y: 0.45073 z: 0.439153
normalized velocity vector (ndv,ndy,ndz) (direction vector of lidar station displacement) : -0.078028 0.71580 0.696713
*** control point transformation statistics ***
ball number: 140 c   base date x,y,z: -24360.2 58969 871.196   later date x,y,z: -28177.2 56834.6 584.954   translated later x,y,z: -24338.3 58980.3 873.474   dx,dy,dz: 21.946 11.2515 2.27823   displacement: 24.7411
ball number: 141 c   base date x,y,z: -23985.1 62445.2 1428.59   later date x,y,z: -28075.1 59333.1 1363   translated later x,y,z: -23782.2 62450.7 1438.43   dx,dy,dz: 27.1119 9.1197 9.83623   displacement: 29.2185
ball number: 142 c   base date x,y,z: -22580.9 61801.3 1574.89   later date x,y,z: -28413.9 58281.1 1376.33   translated later x,y,z: -22325.9 61808.9 1542.97   dx,dy,dz: 26.6177 -4.7054 9.8766   displacement: 35.567
ball number: 143 c   base date x,y,z: -21839 83260.6 2241.88   later date x,y,z: -27989.5 80879.3 1866.7   translated later x,y,z: -21833 83269.5 2235.33   dx,dy,dz: 23.965 0.8632 -6.32667   displacement: 28.2218
ball number: 144 c   base date x,y,z: -14443.9 72332.8 3072.9   later date x,y,z: -12048.3 72327.8 3080.43   translated later x,y,z: -14448.9 72326.8 3051.4   dx,dy,dz: -33.2869 7.10593 -4.6376   displacement: 34.8891
ball number: 145 c   base date x,y,z: -13484.9 76552.1 3682.55   later date x,y,z: -11175.2 74622.5 3515.7   translated later x,y,z: -13438.6 76543.8 3686.25   dx,dy,dz: -45.7891 -8.31566 -4.29742   displacement: 46.8842
ball number: 146 c   base date x,y,z: -12280.8 77339.8 3888.88   later date x,y,z: -10020.6 76214.8 3781.21   translated later x,y,z: -12347.3 77328.8 3889.4   dx,dy,dz: -18.7187 -9.28888 -18.6603   displacement: 47.3226
ball number: 147 c   base date x,y,z: -7586.22 88318.7 15962.3   later date x,y,z: -16588.1 88939.9 15988.2   translated later x,y,z: -7597.73 88320.8 15963.8   dx,dy,dz: 0.446229 2.17346 1.54389   displacement: 2.78197
ball number: 148 c   base date x,y,z: -7182.11 89214.6 16140.3   later date x,y,z: -15107.1 87201.1 15768.9   translated later x,y,z: -7091.43 89214.3 16141.1   dx,dy,dz: 0.45274 9.45272 2.82018   displacement: 40.2114
ball number: 149 c   base date x,y,z: -6469.73 89322.1 16457.5   later date x,y,z: -15451.8 87908.8 16087.7   translated later x,y,z: -6468.18 89323.1 16458.7   dx,dy,dz: 1.54807 6.50386 5.14802   displacement: 9.63822
ball number: 150 c   base date x,y,z: -5615.88 89388.8 16571.7   later date x,y,z: -14844.4 87526.2 16340.7   translated later x,y,z: -5607.73 89388.6 16570.8   dx,dy,dz: 0.190709 1.18893 1.06888   displacement: 21.6074
ball number: 151 c   base date x,y,z: -3788.8 87588.8 20432.4   later date x,y,z: -1838.48 88832.1 20571.9   translated later x,y,z: -3778.8 87588.5 20431.8   dx,dy,dz: 18.0715 11.6119 1.04848   displacement: 22.7
ball number: 152 c   base date x,y,z: -10827.2 87562.2 20388.4   later date x,y,z: -9972.2 88878.7 20114.   translated later x,y,z: -10805.8 87536.7 20388   dx,dy,dz: 18.0008 18.4577 5.59181   displacement: 21.56
ball number: 153 c   base date x,y,z: -13788.8 87588.8 20432.4   later date x,y,z: -14559.5 87888.4 20804   translated later x,y,z: -13778.8 87588.5 20431.8   dx,dy,dz: -4.83807 -15.3244 -8.08511   displacement: 18.4646
ball number: 154 c   base date x,y,z: -2247 78333.3 13355.7   later date x,y,z: -15580.8 72869.9 13339.3   translated later x,y,z: -2246.7 78331.7 13352.3   dx,dy,dz: -1.34618 -3.18284 -1.18307   displacement: 9.44447
ball number: 155 c   base date x,y,z: -12023.9 69375.1 10993.9   later date x,y,z: -15423.2 70975.8 10973.2   translated later x,y,z: -12023.9 69375.1 10993.9   dx,dy,dz: 7.41896 -6.63833 -1.2443   displacement: 8.4672
ball number: 156 c   base date x,y,z: -15168.9 59483 3483.25   later date x,y,z: -13812.7 60876.3 3274.6   translated later x,y,z: -15168.9 59398.8 3472.32   dx,dy,dz: -8.55916 -12.1897 -10.9271   displacement: 18.3511
Average control dx: 4.20739e-008 Average control dy: 5.60855e-008 Average control dz: -3.15754e-008 Average control displacement: 20.8268
```

Figure 2.47. Regballs Displacements of Control Spheres

```
Command Prompt
Average control dx: 4.20739e-008 Average control dy: 5.60855e-008 Average control dz: -3.15554e-008 Average control displacement: 20.8268
*** displacements of floating balls ***
ball number: 130 f   base date x,y,z: 8759.87 62549.2 6189.82   later date x,y,z: 2514.82 61841 5575.77   translated later x,y,z: 8811.63 61517.8 5818.88   dx,dy,dz: 36.5977 -1031.39 -374.974   displacement: 1209.64
ball number: 131 f   base date x,y,z: 8520.95 62556.6 6446.82   later date x,y,z: 2573.55 61774.1 5762.23   translated later x,y,z: 8503.86 61346.1 6006.07   dx,dy,dz: 42.9122 -1210.5 -444.747   displacement: 1089.24
ball number: 132 f   base date x,y,z: 18679.9 60847.2 7534.88   later date x,y,z: 3703.26 60442.9 7231.28   translated later x,y,z: 18642.4 60418.8 7474.76   dx,dy,dz: -16.5207 -17.3469 -406.155   displacement: 141.880
ball number: 133 f   base date x,y,z: 18695.5 60868 7774.3   later date x,y,z: 3815.31 60445.9 7450.98   translated later x,y,z: 18615.5 60794.7 7312.5   dx,dy,dz: -14.0842 -331.95 -45.7971   displacement: 146.454
ball number: 134 f   base date x,y,z: 9567.2 68172.7 9385.23   later date x,y,z: 2593.73 68432.8 9011.26   translated later x,y,z: 9575 67963.8 9278.29   dx,dy,dz: 7.78822 -208.807 -14.637   displacement: 216.478
ball number: 135 f   base date x,y,z: 9566.33 68173.8 9384.93   later date x,y,z: 2593.22 68432.2 9236.98   translated later x,y,z: 9576.88 67958.8 9049.12   dx,dy,dz: 9.74871 -212.367 -143.211   displacement: 241.881
ball number: 136 f   base date x,y,z: 8644.65 71426.2 10326.6   later date x,y,z: 3128.44 71596.8 9899.59   translated later x,y,z: 8633.43 71246.6 10165.5   dx,dy,dz: -11.2181 -189.594 161.128   displacement: 246.037
ball number: 137 f   base date x,y,z: 8649.47 71599 10581.3   later date x,y,z: 3128.08 71587.7 10129.9   translated later x,y,z: 8627.41 71118.8 10189.2   dx,dy,dz: -12.1187 -188.774 -161.084   displacement: 248.687
ball number: 138 f   base date x,y,z: 7597.81 69055.1 10607.05   later date x,y,z: 4611.08 69035.7 9508.43   translated later x,y,z: 7574.53 69215.8 9838.8   dx,dy,dz: -26.2543 -199.274 -159.488   displacement: 250.887
ball number: 139 f   base date x,y,z: 7571.39 69584.4 9961.53   later date x,y,z: 431.453 69573.9 9584.11   translated later x,y,z: 7541.32 69315.5 9833.75   dx,dy,dz: -38.8782 -265.007 -171.778   displacement: 286.546
ball number: 140 f   base date x,y,z: 7743.89 74616.2 11925.4   later date x,y,z: 51.389 74614 11588.4   translated later x,y,z: 7684.1 74589 11342.1   dx,dy,dz: -38.8782 -267.232 -128.886   displacement: 281.86
ball number: 141 f   base date x,y,z: 7752.38 74622.1 12183.9   later date x,y,z: 65.411 74620.9 11783.1   translated later x,y,z: 7699.78 74373.7 11864   dx,dy,dz: -52.6883 -251.453 119.828   displacement: 283.544
ball number: 142 f   base date x,y,z: -10480.9 58373.3 121.081   later date x,y,z: -10922 58269.6 -83.1184   translated later x,y,z: -10379.7 58581.7 258.812   dx,dy,dz: 16.0977 21.5681 83.814   displacement: 145.658
ball number: 143 f   base date x,y,z: -13168.5 58676.7 15805.92   later date x,y,z: -14806.9 59197.8 2754.22   translated later x,y,z: -13684.9 57845.4 3077.87   dx,dy,dz: -334.252 -1031.33 -328.852   displacement: 1890.22
ball number: 144 f   base date x,y,z: -13133.9 58695.4 1651.69   later date x,y,z: -14043.2 55252.8 2585.45   translated later x,y,z: -13686.6 57188.8 2828.47   dx,dy,dz: 547.678 1495.18 -823.424   displacement: 1876.84
ball number: 145 f   base date x,y,z: -13180.4 61732.1 5152.3   later date x,y,z: -15068.9 61964.9 3253.13   translated later x,y,z: -13866.6 60957.5 4151.98   dx,dy,dz: -135.23 -2009.65 -1188.31   displacement: 2641.64
ball number: 146 f   base date x,y,z: -11893.4 61778.2 5876.2   later date x,y,z: -15892.6 60813.1 3787.62   translated later x,y,z: -11992 59803.3 4824.55   dx,dy,dz: -1180.59 -1976.24 -1841.65   displacement: 2459.35
ball number: 147 f   base date x,y,z: -12466.6 67789.7 6882.88   later date x,y,z: -14881.5 62288.9 3488.98   translated later x,y,z: -12474.7 66211.1 3823.81   dx,dy,dz: -1488.26 -1477.87 -468.871   displacement: 2116.39
ball number: 148 f   base date x,y,z: -12618.8 67762.1 6588.8   later date x,y,z: -28858.5 64420.7 5388.1   translated later x,y,z: -12618.8 65445.7 3727.87   dx,dy,dz: -13467.15 -1416.44 -853.731   displacement: 2145.75
ball number: 149 f   base date x,y,z: -10844.9 62813.4 5820.31   later date x,y,z: -13844.6 59220.4 4718.19   translated later x,y,z: -11024.5 60015.1 5843.93   dx,dy,dz: -1608.24 -1898.31 -776.578   displacement: 2116.03
ball number: 150 f   base date x,y,z: -10031.6 62868 5074.55   later date x,y,z: -17864.9 59321.9 4648.93   translated later x,y,z: -11862.9 61882.5 4824.39   dx,dy,dz: -1809.98 -1883.31 -751.766   displacement: 2207.54
ball number: 151 f   base date x,y,z: -9728.87 72191.7 9069.54   later date x,y,z: -17558.9 68479.8 8331.76   translated later x,y,z: -10378.9 71059.4 8676.73   dx,dy,dz: -650.84 -1232.35 -382.311   displacement: 1447.6
ball number: 152 f   base date x,y,z: -9717.86 72284.6 8580.87   later date x,y,z: -17530.8 68828.1 8322.28   translated later x,y,z: -9833.8 71386.8 8473.16   dx,dy,dz: -637.92 -1128.65 -387.789   displacement: 1448.45
ball number: 153 f   base date x,y,z: -8418.8 71769.9 9072.8   later date x,y,z: -16327 69135.5 8345.25   translated later x,y,z: -9187.84 70590.9 8684.86   dx,dy,dz: -769.84 -1178.98 -387.844   displacement: 1446.11
ball number: 154 f   base date x,y,z: -8421.12 71767.8 8844.77   later date x,y,z: -16209 67163.3 8115.28   translated later x,y,z: -9102.8 70618.6 8408.21   dx,dy,dz: -778.794 -1151.88 -388.159   displacement: 1447.83
ball number: 155 f   base date x,y,z: -8536.84 67288 9394.02   later date x,y,z: -16218 64911.5 8538.79   translated later x,y,z: -8831.58 68381.2 7486.86   dx,dy,dz: -889.31 -1586.81 -761.926   displacement: 1422.78
ball number: 156 f   base date x,y,z: -8543.92 67807.1 7716.83   later date x,y,z: -16253.3 64844.7 6628.71   translated later x,y,z: -9548.87 66416.8 6958.88   dx,dy,dz: -784.147 -1488.15 -728.15   displacement: 1524.44
ball number: 157 f   base date x,y,z: -8431.15 64412.1 6388.49   later date x,y,z: -15643.7 58711.1 6444.74   translated later x,y,z: -8275.77 68284.4 6963.85   dx,dy,dz: -844.619 -2484.17 -4366.73   displacement: 2778.34
ball number: 158 f   base date x,y,z: -8346.95 62318.4 6128.81   later date x,y,z: -15362.6 59817.4 4355.31   translated later x,y,z: -8272.42 68831.9 4867.2   dx,dy,dz: -924.488 -2879.1 -1201.81   displacement: 2682.59
ball number: 159 f   base date x,y,z: -8277.82 59980.7 4607.5   later date x,y,z: -15451.3 58685.8 3165.64   translated later x,y,z: -8658.81 67462.8 3425.33   dx,dy,dz: -611.889 -4408.78 -1153.92   displacement: 1542.68
ball number: 160 f   base date x,y,z: -9188.84 58961.8 4564.75   later date x,y,z: -14441.5 58878.8 2984.89   translated later x,y,z: -8657.83 57517.9 3212.71   dx,dy,dz: -476.901 -1476.81 -1152.84   displacement: 1932.88
ball number: 161 f   base date x,y,z: -7114.88 72812 5111.43   later date x,y,z: -15882.6 66441 8403.98   translated later x,y,z: -7917.6 70783.3 8818.47   dx,dy,dz: -792.025 -1243.74 -292.959   displacement: 1503.65
ball number: 162 f   base date x,y,z: -7115.88 72812 5111.43   later date x,y,z: -15882.6 66441 8403.98   translated later x,y,z: -7917.6 70783.3 8818.47   dx,dy,dz: -792.025 -1243.74 -292.959   displacement: 1503.65
ball number: 163 f   base date x,y,z: -6488.35 77725.8 11789.4   later date x,y,z: -14438.8 76234.1 11898.2   translated later x,y,z: -6547.34 77435.3 11388   dx,dy,dz: -142.888 -178.519 -483.397   displacement: 588.515
ball number: 164 f   base date x,y,z: -6411.46 77746.1 11493.4   later date x,y,z: -14445.3 76212.1 10792.1   translated later x,y,z: -6554.41 77429.7 11088.8   dx,dy,dz: -143.913 -389.359 -483.619   displacement: 515.731
```

Figure 2.48. Regballs Displacements of Floating Spheres


```

C:\Users\Ben\OutropData\Site\veg\Observations\regballs-report-2015-07-19w3-to-2017-01-01\01w1.txt - Notepad++
File Edit Search View Encoding Language Settings Tools Macro Run Plugins Window ?
regballs-report-2015-07-19w3-to-2017-01-01\01w1.txt
1 ***** Summary of Spherical Target Statistics *****
2
3 3-D rmse: 22.838 mm      number of control points: 17
4
5 apparent displacement of lidar between base and later scans: 151.83 mm ( 0.50 feet)
6
7 apparent displacement (feet) in x: 0.35 y: 0.03 z: 0.36
8
9 normalized velocity vector (ndx,ndy,ndz) direction vector of lidar station displacement: 0.69 0.06 0.72
10
11
12
13 *** control point transformation statistics ***
14 ball number: 140 initial position: -24360.20 +58969.00 +871.20 transformed final position: -24362.93 +58974.15 +870.76 residual dx,dy,dz: -2.73 +5.15 -0.43 residual:
15 ball number: 141 initial position: -23905.30 +62445.40 +1429.59 transformed final position: -23903.47 +62443.76 +1440.28 residual dx,dy,dz: +1.83 -1.44 +11.69 residual:
16 ball number: 142 initial position: -22350.50 +61585.20 +1734.09 transformed final position: -22351.49 +61581.33 +1734.34 residual dx,dy,dz: +88.01 -3.87 +0.25 residual:
17 ball number: 143 initial position: -21639.00 +63260.60 +2241.88 transformed final position: -21599.67 +63270.90 +2231.21 residual dx,dy,dz: +39.33 +10.30 -10.67 residual:
18 ball number: 144 initial position: -14431.50 +75213.50 +8672.90 transformed final position: -14444.87 +75211.35 +8667.74 residual dx,dy,dz: -13.37 -2.15 -5.16 residual:
19 ball number: 145 initial position: -13044.90 +76552.10 +9692.55 transformed final position: -13029.33 +76547.97 +9692.86 residual dx,dy,dz: -15.57 +4.13 -4.69 residual:
20 ball number: 146 initial position: -12306.60 +77339.60 +10080.00 transformed final position: -12325.00 +77333.76 +10067.48 residual dx,dy,dz: -18.40 -5.84 -12.52 residual:
21 ball number: 148 initial position: -7598.22 +89318.70 +15962.30 transformed final position: -7605.97 +89320.08 +15972.57 residual dx,dy,dz: -7.75 +1.38 +10.27 residual:
22 ball number: 149 initial position: -7102.12 +89524.80 +16240.30 transformed final position: -7107.56 +89522.13 +16250.63 residual dx,dy,dz: -5.44 +2.33 +10.33 residual:
23 ball number: 150 initial position: -6463.71 +88322.20 +16457.50 transformed final position: -6466.84 +88326.55 +16466.03 residual dx,dy,dz: -3.13 +4.35 +8.53 residual:
24 ball number: 151 initial position: -5413.69 +89288.20 +16527.10 transformed final position: -5415.78 +89293.16 +16536.30 residual dx,dy,dz: -2.06 +4.96 +9.20 residual:
25 ball number: 152 initial position: +17895.90 +87590.90 +20429.50 transformed final position: +17901.37 +87604.14 +20434.01 residual dx,dy,dz: +15.47 +12.24 +4.51 residual:
26 ball number: 153 initial position: +19027.20 +87526.20 +20380.40 transformed final position: +19043.30 +87538.53 +20383.50 residual dx,dy,dz: +16.10 +12.33 +3.10 residual:
27 ball number: 155 initial position: +21794.00 +69308.50 +11168.00 transformed final position: +21787.51 +69294.12 +11152.24 residual dx,dy,dz: -6.49 -14.38 -15.76 residual:
28 ball number: 156 initial position: +22417.00 +70335.30 +11555.70 transformed final position: +22408.62 +70331.32 +11539.04 residual dx,dy,dz: -8.38 -3.98 -16.66 residual:
29 ball number: 157 initial position: +26623.90 +69175.10 +10993.90 transformed final position: +26620.18 +69167.75 +10976.77 residual dx,dy,dz: -3.71 -7.35 -17.13 residual:
30 ball number: 158 initial position: +19168.90 +59403.00 +5483.25 transformed final position: +19154.05 +59387.72 +5513.40 residual dx,dy,dz: -14.85 -15.28 +30.15 residual:
31
32 average control dx: +0.0000000 average control dy: +0.0000001 average control dz: +0.0000001 average control displacement: +20.4883243
33
34
35 *** displacements of floating balls ***
36
37 ball number: 120 initial position: +8795.07 +62549.20 +6195.02 transformed final position: +8825.29 +61516.85 +5808.34 dx,dy,dz: +30.22 -1032.35 -386.68 displacement: :
38 ball number: 121 initial position: +8920.95 +62556.60 +6449.62 transformed final position: +8856.90 +61345.29 +5994.04 dx,dy,dz: +35.95 -1211.31 -454.78 displacement: :
39 ball number: 122 initial position: +10478.90 +65047.20 +7534.88 transformed final position: +10458.38 +64922.80 +7463.87 dx,dy,dz: -20.52 -124.40 -71.01 displacement: :
40 ball number: 123 initial position: +10496.30 +65002.00 +7774.30 transformed final position: +10476.62 +64872.00 +7701.98 dx,dy,dz: -19.68 -130.00 -72.32 displacement: :
41 ball number: 124 initial position: +9567.20 +68172.70 +9385.23 transformed final position: +9572.04 +67963.55 +9262.57 dx,dy,dz: +4.84 -209.15 -122.66 displacement: :
42 ball number: 125 initial position: +9564.33 +69171.30 +9610.33 transformed final position: +9570.89 +67957.93 +9497.64 dx,dy,dz: +6.56 -213.97 -122.69 displacement: :
43 ball number: 126 initial position: +8644.68 +71426.20 +10326.60 transformed final position: +8630.66 +71240.78 +10159.98 dx,dy,dz: -14.02 -185.42 -166.62 displacement: :
44 ball number: 127 initial position: +8649.42 +71399.00 +10561.10 transformed final position: +8634.92 +71212.30 +10393.73 dx,dy,dz: -14.50 -186.70 -167.37 displacement: :

```

Figure 2.49. Regballs Report Example

From the control point transformation statistics, the three-dimensional root mean square error (RMSE) is computed for the two-scan comparison. These RMSE values designate the stress between a set of observations, usually the observations of a specific reference date, and the observations of the control points or spheres of the base date. This reference date is taken through a least-squares adjustment based on a seven-parameter conformal transformation. This transformation is based on a three-dimensional similarity transform developed by Chris McGlone and documented in his co-authored book on photogrammetry (Mikhail et al, 2001). The transform was converted from the FORTRAN programming language to the C++ programming language and wrapped in the Transform7ls class wrapper by the LiDAR Applications Team on May 25, 2011 for use in the lidarsw software suite. The seven-parameter conformal transformation is capable of translation in x, y, and z, rotation about the x, y, and z axes, and it can also apply a universal scalar. This conformal transform cannot perform differential scaling, twisting,

flipping, or warping. A matrix representation of the transform can be seen in the 4 X 4 array in Figure 2.50. This is a compact way of representing the transform.

A *transformation* of the projective space is a mapping $M : \mathbb{P}^3 \rightarrow \mathbb{P}^3$ given by

$$\begin{pmatrix} s \\ u \\ v \\ w \end{pmatrix} \mapsto \begin{pmatrix} m_{11} & m_{12} & m_{13} & m_{14} \\ m_{21} & m_{22} & m_{23} & m_{24} \\ m_{31} & m_{32} & m_{33} & m_{34} \\ m_{41} & m_{42} & m_{43} & m_{44} \end{pmatrix} \begin{pmatrix} s \\ u \\ v \\ w \end{pmatrix}.$$

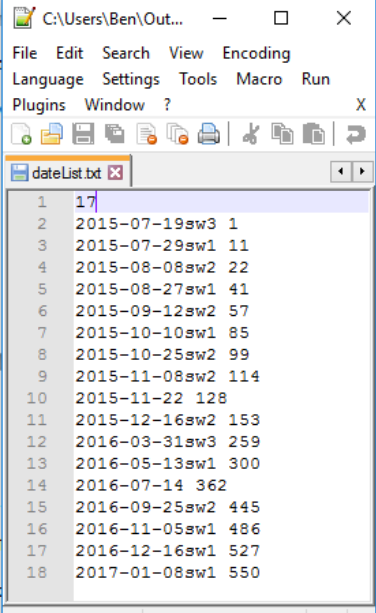
The 4×4 matrix (m_{ij}) is called the *homogeneous transformation matrix* of M . If the matrix is non-singular, then M is called a *non-singular transformation*. If $m_{41} = m_{42} = m_{43} = 0$ and $m_{44} \neq 0$, then M is said to be an *affine transformation*. Affine transformations correspond to translations, scalings, rotations, reflections, etc. of the three-dimensional space.

Figure 2.50. Homogeneous Transformation Matrix of M
(Jia, 2016)

The RMSE values are a representation of the change in the overall shape of the control point arrangement from the base date. The residual displacement values of the control points are also consulted to discern if any outliers are present. If all absolute values of the magnitudes of dx, dy, dz for the control point residuals are equal or near equal then the transform was successful and has kept the floaters in the correct position. An example of these dx, dy, and dz magnitudes can be seen in Figure 2.49. The regballs program also creates a base coordinates file for that specific date. This base coordinates file is a text file of the all the sphere coordinates from a later date in the reference system of the base date.

2.3.8 Surf2vrml Program. There is one more step in the processing of the data which allows a three-dimensional viewing of the slide and the movement of each rod. It

can also create profiles of the slide. The surface files are transformed into vrmf files. The tool that performs this procedure is surf2vrmf. The surf2vrmf program uses a “datelist” text file, a “rodConfig” text file, and a “vrmfConfig” text file. The datelist text file can be seen in Figure 2.51 and the vrmfconfig file can be seen in Figure 2.52. The “datelist” file is a simple text file that contains the number of dates being used, each scan date followed by the day number the scan was collected. The base date has a number 1. The “rodConfig” file contains each rod number, the diameter of the rod, the sphere numbers mounted on the rod, the height in inches the rod is above the ground surface, and the depth in inches the rod is below the ground surface. This configuration file needs to be updated each time new rods are placed on the slide.



```

1 17
2 2015-07-19sw3 1
3 2015-07-29sw1 11
4 2015-08-08sw2 22
5 2015-08-27sw1 41
6 2015-09-12sw2 57
7 2015-10-10sw1 85
8 2015-10-25sw2 99
9 2015-11-08sw2 114
10 2015-11-22 128
11 2015-12-16sw2 153
12 2016-03-31sw3 259
13 2016-05-13sw1 300
14 2016-07-14 362
15 2016-09-25sw2 445
16 2016-11-05sw1 486
17 2016-12-16sw1 527
18 2017-01-08sw1 550

```

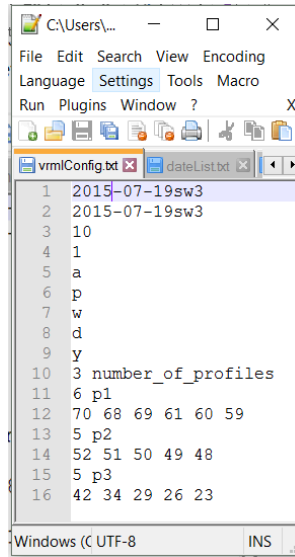
Figure 2.51. dateList.txt File

The vrmconfig file is a text file composed of 14 features shown in Figure 2.52 below.

These features are as follows:

1. Ground plane display date
2. Base date
3. Step factor
4. Vector multiplier
5. Rod options
6. Ground plane display option
7. Ground plane color option
8. Vector display option
9. Rod label option
10. # of x profiles
11. # of rods in first profile
12. Rod IDs in first profile
13. # of rods in second profile
14. Rod IDs in the second profile

This configuration file changes how the displacements, profile, and ground plane is represented in three-dimensional viewing files. These files show the displacement data in a three-dimensional format.



```

1 2015-07-19sw3
2 2015-07-19sw3
3 10
4 1
5 a
6 p
7 w
8 d
9 y
10 3 number_of_profiles
11 6 p1
12 70 68 69 61 60 59
13 5 p2
14 52 51 50 49 48
15 5 p3
16 42 34 29 26 23

```

Figure 2.52. vrmIconfig.txt File

2.3.9 Precision and Repeatability Tests of Sphere Center Positions. To

ensure the accuracy and precision of the processing software and method, a repeatability test was performed using similar spherical Styrofoam targets and measuring their actual displacement versus the displacement measured by the Scanstation 2. This test was performed indoors in a controlled environment. The accuracy was calculated using spheres mounted to a displacement rig. This rig is shown below in Figure 2.53.



Figure 2.53. Displacement Rig
(Maerz et al., 2016)

This displacement rig could accurately displace the spherical targets mounted on it to a known distance. The displacement measurements of the rig were accurate to 0.025 mm. The four spheres mounted on a hinged rectangular plate in the middle of the rig were displaced by turning the dial plate attached to a 10 thread per inch screw. Turning the dial plate 360° resulted in a displacement of 2.323 mm for the top sphere and 0.411 mm for the bottom sphere with the remaining two having a range of displacements in between. The spheres in the four corners were in a fixed position throughout the test so they could be used as reference targets. All of the spheres used in the test were 100 mm (~4 in.) in diameter.

The Scanstation 2 was set up at 26 m from the displacement rig. The rig was scanned once then the dial plate was rotated one turn and the Scanstation 2 was displaced 3 m to accurately represent the re-setup of the scanner. Another scan was then collected. Both scans were processed through the lidarsw suite and the measured displacement of the sphere centers was compared to the actual displacement of the sphere centers. The comparison of the data is shown below in Table 2.2.

Table 2.2. Comparison of LiDAR Measured Displacement with the Actual Displacement of the Four Target Balls.

Target Ball	LIDAR Measured Displacement	Actual Displacement (calculated)	Difference (Accuracy)
Top	2.695 mm	2.323 mm	-0.372 mm
Upper middle	1.590 mm	1.677 mm	0.087 mm
Lower middle	1.600 mm	1.035 mm	-0.565 mm
Bottom	0.450 mm	0.411 mm	-0.039 mm

This comparison shows that the Scanstation 2 can detect and measure small displacements of spherical targets in a controlled setting. A similar outdoor field test was performed which showed similar results. A scan of the displacement rig was performed using a scanning resolution of 1 mm at a distance of 56.4 m. Two separate scans were conducted, moving the spheres on the displacement rig in between the scans. The Scanstation 2 was also move approximately 0.3 m to change the coordinate system, which then in turn required a registration process. The second scan was registered to the

first scan using the to the first using the 7-parameter conformal three-dimensional transform based on the four fixed control points on the displacement rig. The average displacement error that was calculated, based on the actual measured displacement, was less than 0.3 mm. The results of this test are presented below in Table 2.3.

Table 2.3. Results of Displacement Field Test

Ball #	Measured Displacement	Actual Displacement	Difference (Accuracy)
Top (F-8)	0.81 mm	0.915 mm	-0.105 mm
Upper Middle (F-7)	0.05 mm	0.670 mm	-0.620 mm
Lower Middle (F-6)	0.14 mm	0.418 mm	-0.278 mm
Bottom (F-5)	0.34 mm	0.173 mm	-0.167 mm

2.3.10 Data Representation. An Excel spreadsheet was developed to better analyze the information generated by the entire processing suite, specifically the data output from the regballs program. The spreadsheet contained multiple columns in which to put the x, y, and z coordinates of each of the sphere centers generated by the regballs program. All the x, y, and z coordinates are in the reference system of the base date so that they can be properly compared with each other. The changes in the x, y, and z coordinates of each sphere was calculated from each date to the base date, as well as from each date to the date directly preceding it. These changes in each coordinate were represented in columns labeled dx, dy, and dz. A $d\theta$ data column was also created for

each date to represent the rotation of a specific rod from either the base date to a later date, or a specific date to another later date. This change in rotational angle was calculated for each floating rod on the slide by using the position of the top sphere and bottom sphere on each rod, as well as their change in positions between each date. This $d\theta$ column was calculated using the following equation:

$$d\theta = \text{Arccos}\left(\frac{\{(y_{bot}-y_{top})*(y_{bot+dy_{bot}})-(y_{top+dy_{top}})\}+\{(z_{bot}-z_{top})*(z_{bot+dz_{bot}})-(z_{top+dz_{top}})\}}{\sqrt{[(y_{bot}-y_{top})^2+(z_{bot}-z_{top})^2]*\{(y_{bot+dy_{bot}})-(y_{top+dy_{top}})\}^2+\{(z_{bot+dz_{bot}})-(z_{top+dz_{top}})\}^2}}}\right) \quad (4)$$

Where:

y_{bot} is the y coordinate of the bottom sphere in the base date reference system

y_{top} is the y coordinate of the top sphere in the base date reference system

z_{bot} is the z coordinate of the bottom sphere in the base date reference system

z_{top} is the z coordinate of the top sphere in the base date reference system

dy_{bot} is the change y coordinate of the bottom sphere from the base date to the later date

dy_{top} is the change y coordinate of the top sphere from the base date to the later date

dz_{bot} is the change z coordinate of the bottom sphere from the base date to the later date

dz_{top} is the change z coordinate of the top sphere from the base date to the later date

3 RESULTS

3.1 GENERAL DISPLACEMENTS AND RATES OF MOVEMENT

Over the course of the survey, there were 17 separate LiDAR point cloud data collection periods. These point cloud data collection periods correspond to the following 17 dates:

- July 19, 2015
- July 29, 2015
- August 8, 2015
- August 27, 2015
- September 12, 2015
- October 10, 2015
- October 25, 2015
- November 8, 2015
- November 22, 2015
- December 16, 2015
- March 31, 2016
- May 13, 2016
- July 14, 2016
- September 25, 2016
- November 5, 2016
- December 16, 2016
- January 8, 2017

The total number of days from the base date (July 19, 2015) to the final date (January 8, 2017) is 550. This is a monitoring period of about 1.5 years. The results and processed data gathered over this period shows the feasibility of the method and shows that the method can give an indication of how the Stone County Landslide moves and reacts during specific seasons of the year. Displacement measurements rates of movement across the entire slide give a general sense of how this landslide is behaving. These measurements were taken from the regballs program readout of each date after processing the point cloud data. The average displacements of all targets between each date and the daily rate of movement can be seen in Table 3.1 below.

Table 3.1. General Displacements and Rates of Movement Measured by Scanstation 2

Date	Day	Displacement from base date (mm)	Rate from previous date (mm/day)
July 19, 2015	1	0	0
July 29, 2015	11	25.3	2.53
August 8, 2015	22	36.08	0.98
August 27, 2015	41	65.75	1.56
September 12, 2015	57	89.52	1.49
October 10, 2015	85	120.28	1.1
October 25, 2015	99	160.66	2.88
November 8, 2015	114	203.27	2.84
November 11, 2015	128	208.23	0.35
December 16, 2015	153	344.48	5.45
March 31, 2016	259	1146.92	7.57
May 13, 2016	300	1171.42	0.6
July 14, 2016	362	1196.2	0.4
September 25, 2016	445	1225.88	0.36
November 5, 2016	486	1246.33	0.5
December 16, 2016	527	1257.1	0.26
January 8, 2017	550	1263.36	0.27

The same data is presented below in a visual format in Figure 3.1.

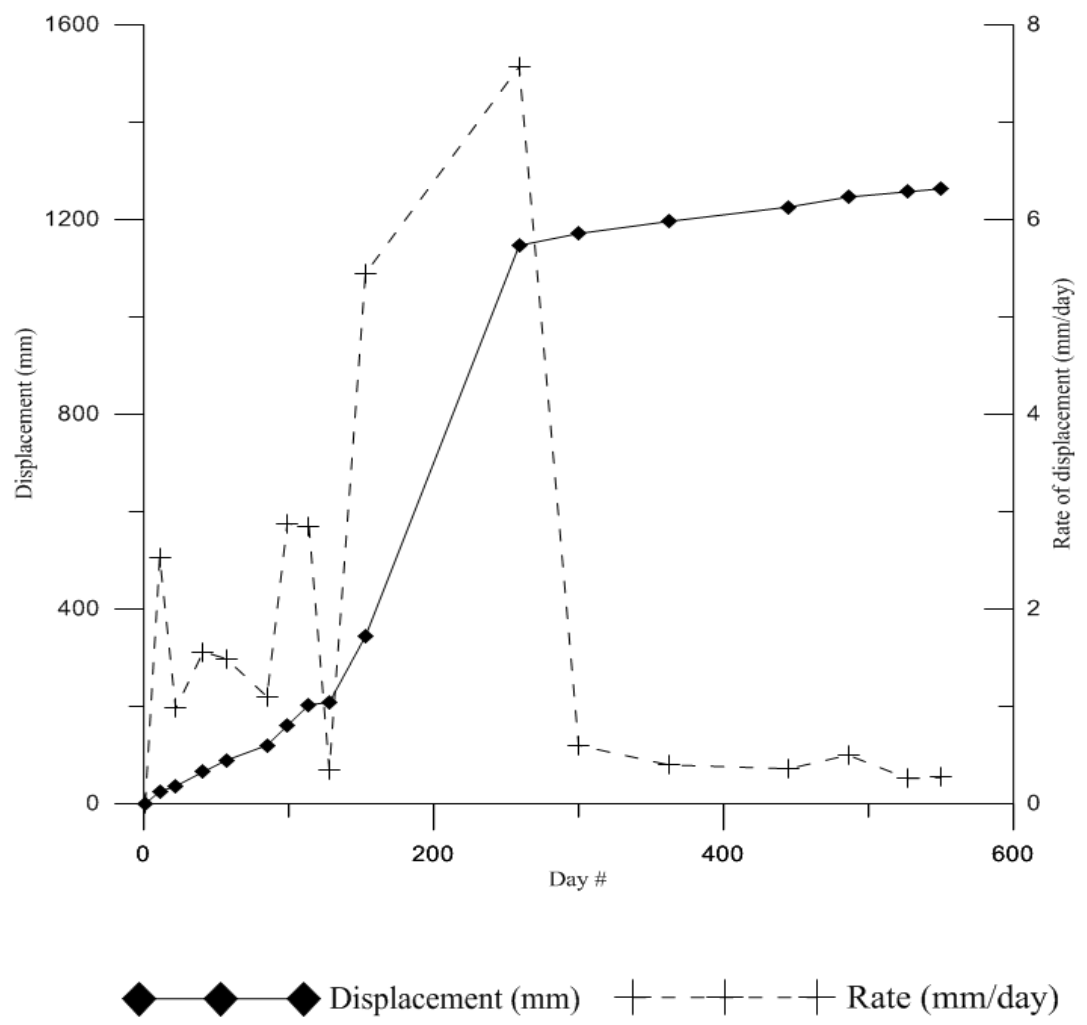


Figure 3.1. General Displacement and Rate Report from Base to Final Date

As can be seen in Table 3.1 and Figure 3.1, the largest amount of displacement and the largest rate of movement occurred during the winter season of late 2015 and early 2016. The two largest rates of movement occurred between November 22, 2015 and December 16, 2016 and from December 16, 2015 to March 31, 2016. These rates are 5.45 mm/day and 7.57 mm/day respectively. The average rate of movement of all the measured rates is 1.82 mm/day. If the two largest rates mentioned above are removed, the average rate of movement across the entire slide drops to 1.15 mm/day.

The general displacement measurements with a linear trendline can be seen below in Figure 3.2 and the linear trend statistics of the general displacement measurements can be seen below in Figure 3.3.

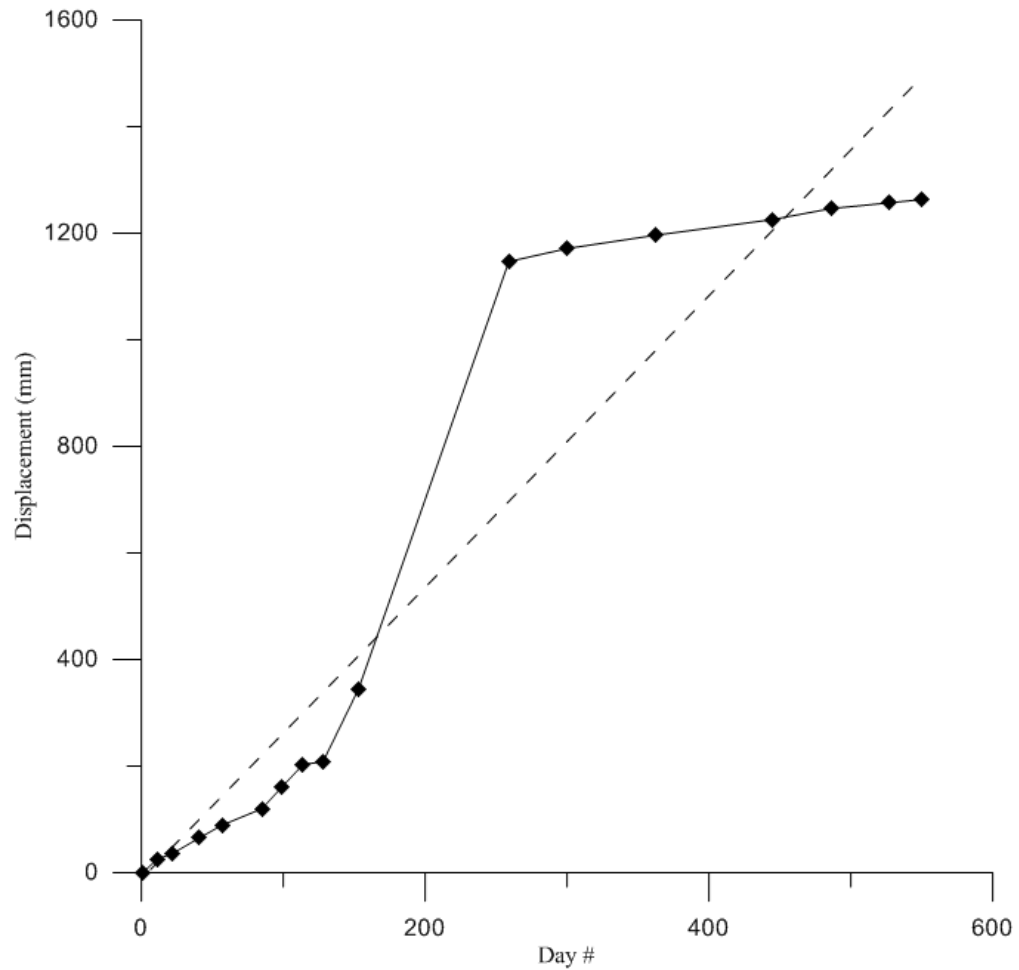


Figure 3.2. General Displacement Report with Linear Trendline

Fit Results

Linear Trend
Equation $Y = 2.736086943 * X - 11.68096899$
Number of data points used = 17
Average X = 214.118
Average Y = 574.164
Residual sum of squares = 523906
Regression sum of squares = 4.48076E+006
Coef of determination, R-squared = 0.895316
Residual mean square, $\sigma\text{-hat-sq'd}$ = 34927.1

Figure 3.3. General Displacement Report Linear Trendline Statistics

The movement of specific areas of the slide are better analyzed by assigning each rod a change in x position, a change in y position, a change in z position, and a rotational angle based on the regballs readout between two scans and plotting each of these parameters on separate contour plots. These contour plots were generated using Surfer software. In each of these contour plots, the parameters are designated as follows:

- Positive X is movement towards the right (north) side of the slide
- Negative X is movement towards the left (south) side of the slide
- Positive Y is movement towards the head of the slide (away from the scanner)
- Negative Y is movement towards the toe of the slide (towards the scanner)
- Positive Z is an increase in elevation
- Negative Z is a decrease in elevation
- Downslope rotation angle is based on the relative positions of the top sphere and bottom sphere of each rod and is calculated using Equation 4

The x coordinate and y coordinate positions of each rod are relative to the scanner position. In a three-dimensional coordinate system, the laser emitter on the terrestrial laser scanner is the origin in the system. The overall change in x, y, z, and rotation angle can be seen in Figures 3.4, 3.5, 3.6, and 3.7 respectively.

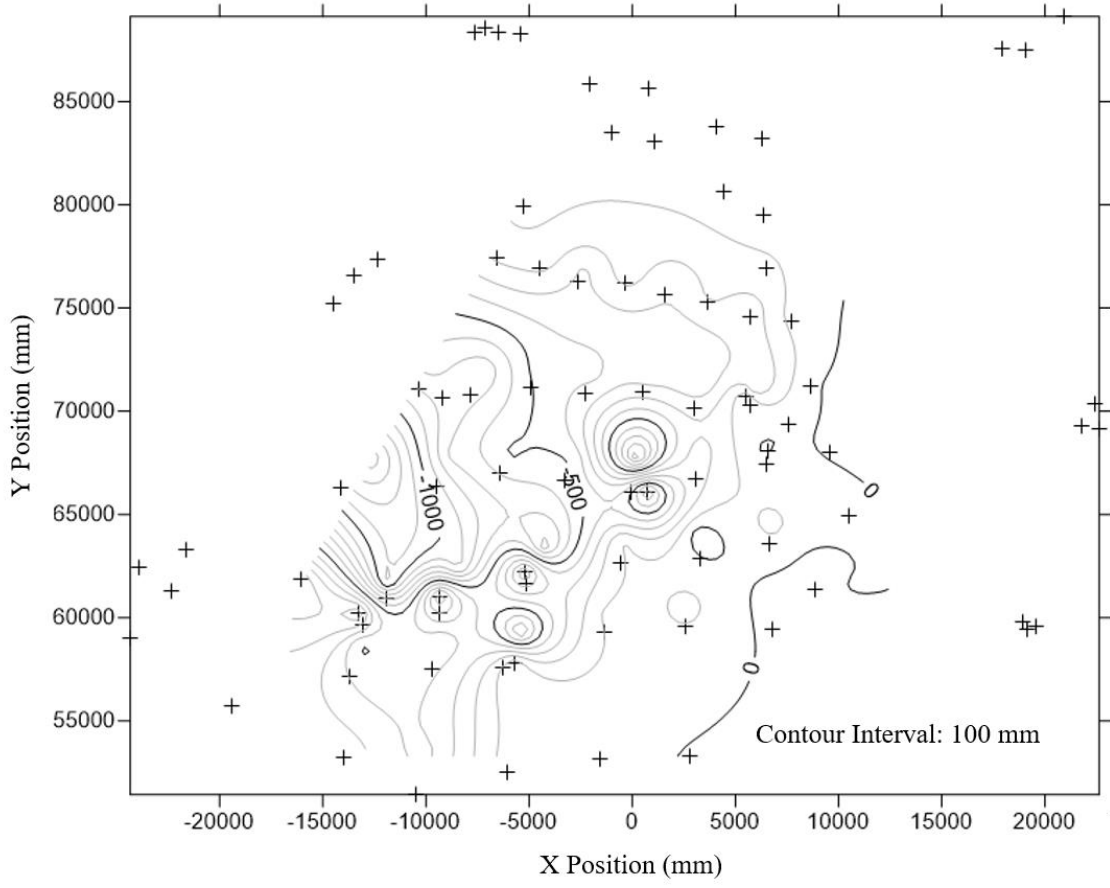


Figure 3.4. Overall Change in Top Sphere X Position between July 19, 2015 and January 8, 2017
+ Symbols Represent Target Positions. Positive X is movement toward the right of the plot.

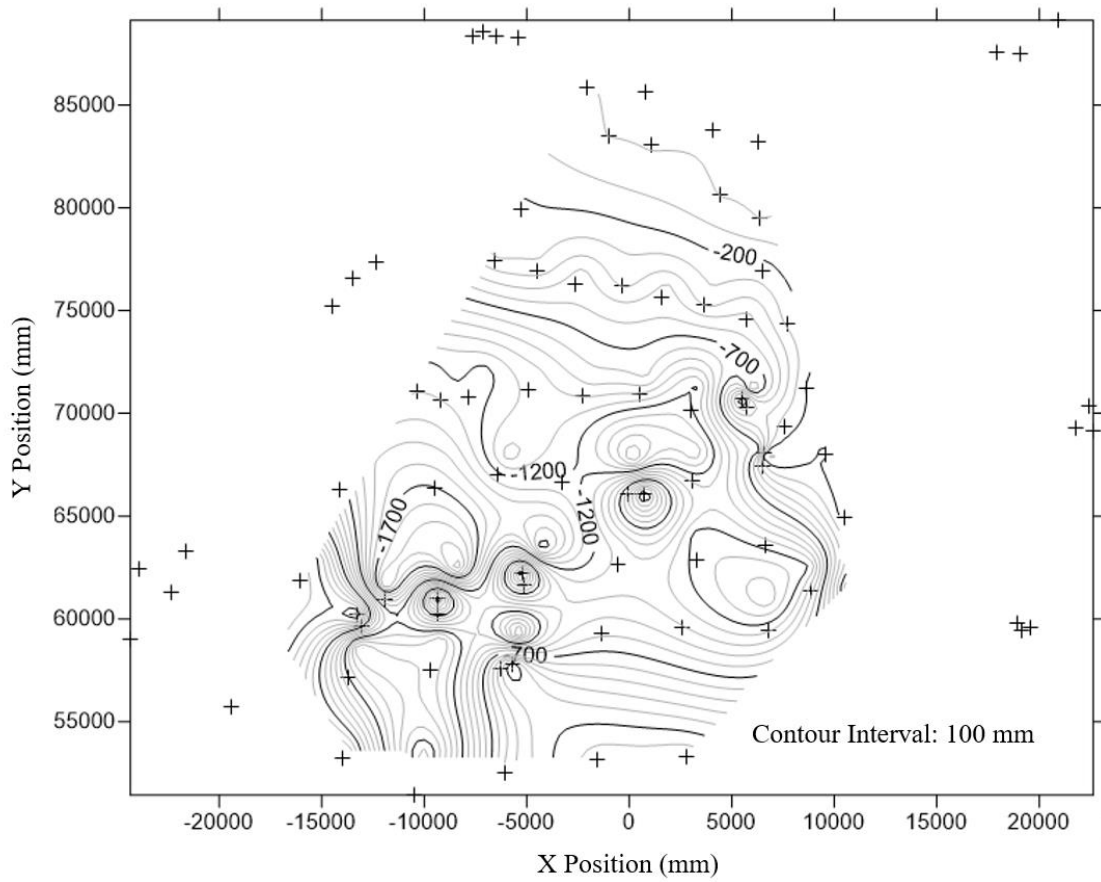


Figure 3.5. Overall Change in Top Sphere Y Position between July 19, 2015 and January 8, 2017

+ Symbols Represent Target Positions. Positive Y is movement toward the top of the plot.

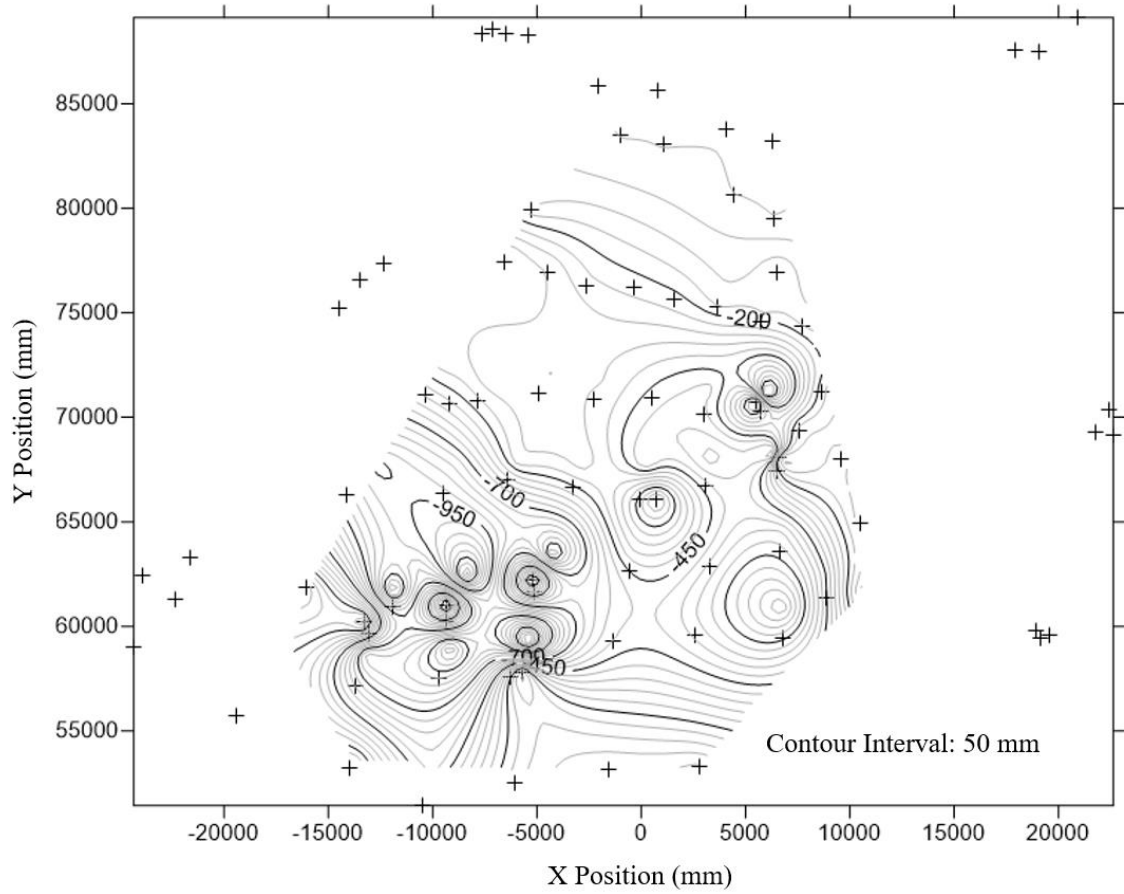


Figure 3.6. Overall Change in Top Sphere Z Position between July 19, 2015 and January 8, 2017

+ Symbols Represent Target Positions. Positive Z is movement out of the page.

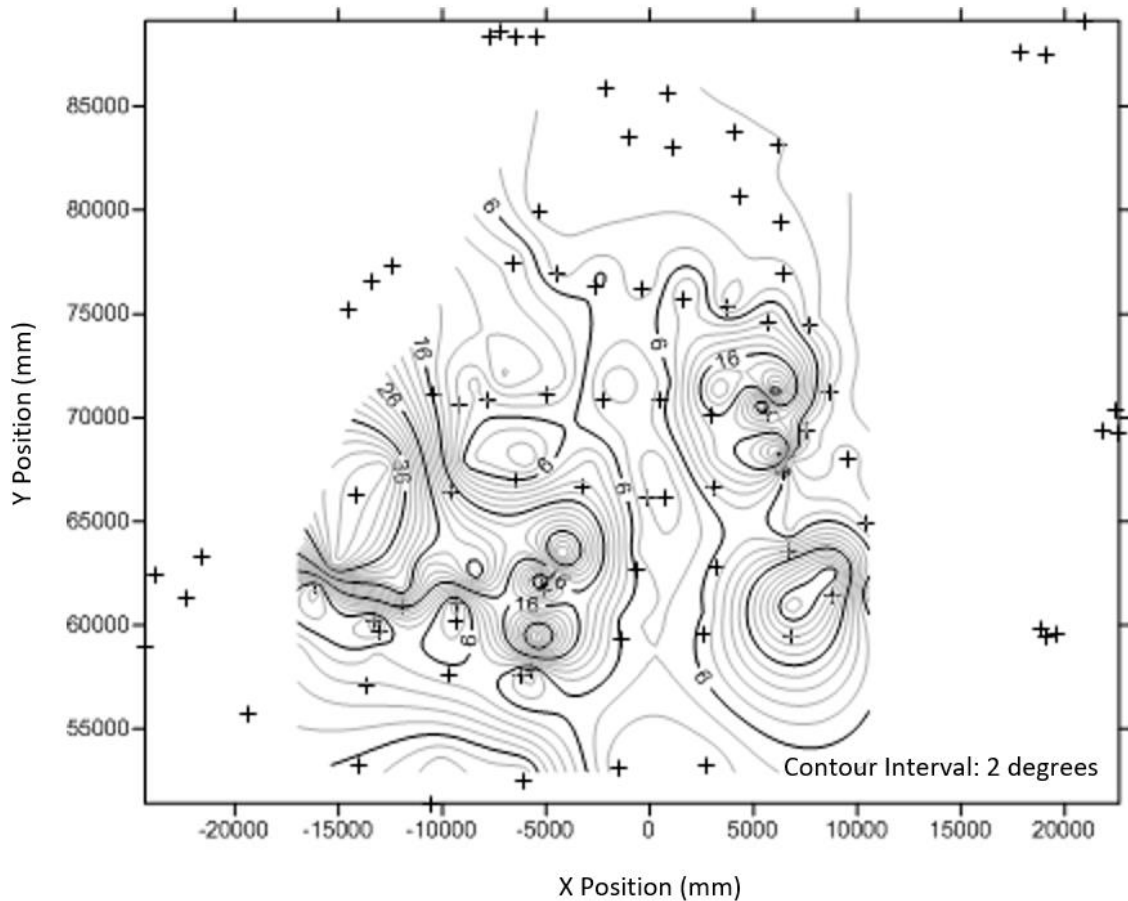


Figure 3.7. Overall Rod Rotation between July 19, 2015 and January 8, 2017
 + Symbols Represent Target Positions. Positive angle measurement is downslope rotation.

These contour plots show that the greatest amount of movement during the monitoring period occurred on the lower left to middle left portion of the slide. The largest magnitude of movement was in the negative y direction, which is towards the toe of the slide and the scanner position and not in the z direction. This is typical movement of a landslide that has a slope less than 45 degrees, which is a characteristic of the Stone County Landslide. The second largest amount of movement is occurring in the negative z

direction. This is also typical of a soft slope landslide movement. As material move further downslope, the material decreases in relative elevation. These large movements were able to be observed by the relative positions of the rods. An example of large rod movement and therefore large material movement can be seen in Figure 3.8. This rod has almost been completely overturned and changed position so much that it could not be measured by the scanner for a portion of the study.



Figure 3.8. Example of Large Rod Movement
(2 ft. Carpenter's Rule for scale)

During the surface mapping that took place on January 8, 2017, it was observed that there are some divots in the upper middle and right portion of the slide that could be due to the material being under tension due to the large southeasterly movement in the lower left portion of the slide. The location of these divots can be observed in the ground surface map of the slide in Figure 2.22. The divots can be seen in Figure 3.9 below. This picture was taken standing on the upper middle portion of the slide, looking towards the south side of the slide.



Figure 3.9. Divot on Upper Middle Portion of the Slide
(Divot Boundaries Outlined in Red)

A relatively large amount of movement took place in the areas of the slide that had minimal vegetation. An example of this large movement on the non-vegetated areas

can be seen in 3.10 where the original target rod has tilted forward so far forward. The rods present in the foreground are rods 30 and 82. Rod 30 is partially painted red, while rod 82 does not have any paint on it. Rod 82 was driven into the slide as close to rod 30 as possible in order to continue measuring the movement of that specific area. Rod 82 was added on March 31, 2016. A similar situation can be seen in the background of Figure 3.10, with respect to rod 38 and rod 83. Rod 83 was driven into the slide as close to rod 38 as possible to continue the monitoring of that area. Rod 83 was also added on March 31, 2016.



Figure 3.10. Example of Movement within a Non-Vegetated Area (New Rods Placed March 31, 2016)
(Rod 30 and Rod 82 in foreground, Rod 38 and Rod 83 in background)

3.2 SEASONAL DISPLACEMENT MOVEMENT REPORTS

To better observe the seasonal trends of the Stone County Landslide, the general displacement report was broken up into three separate periods. The first period is the summer and fall seasons of 2015. The second period is the winter season of 2015 through 2016. The third period is the spring, summer, and fall seasons of 2016.

3.2.1 Summer and Fall Seasons of 2015. The summer and fall seasons of 2015 are represented by the time between July 19, 2015 and November 22, 2015. The displacement report for these dates is shown below in Figure 3.11. The linear trend statistics for the displacement report is shown below in 3.12.

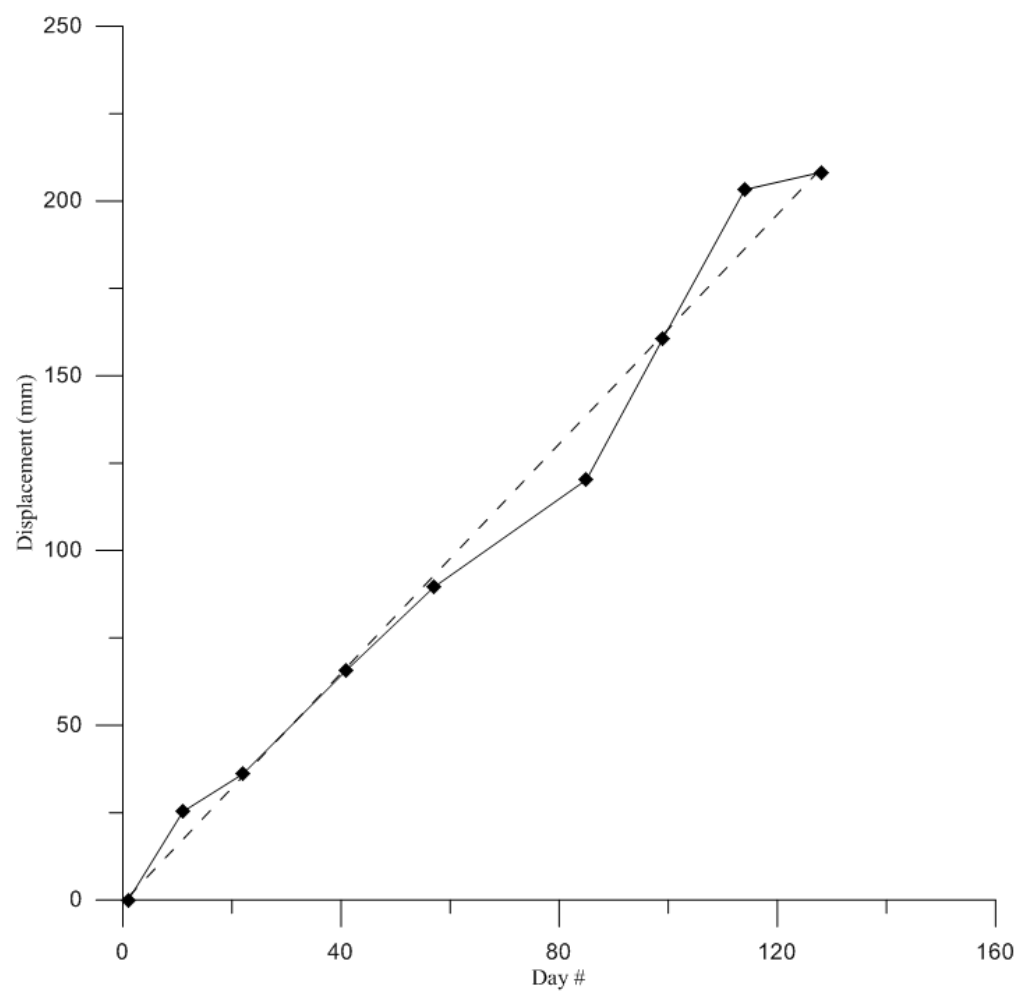


Figure 3.11. Summer and Fall 2015 Displacement Report with Linear Trendline

Fit Results

Linear Trend
Equation $Y = 1.640852646 * X - 0.7228640609$
Number of data points used = 9
Average X = 62
Average Y = 101.01
Residual sum of squares = 706.583
Regression sum of squares = 46702.3
Coef of determination, R-squared = 0.985096
Residual mean square, sigma-hat-sq'd = 100.94

Figure 3.12. Summer and Fall 2015 Displacement Report Linear Trendline Statistics

The summer and fall seasonal displacement of 2015 was further analyzed by employing the use of contour plots similar to those present in the general displacement analysis. The contour plot representing the change in the top sphere's x position, y position, z position, and the rotation of the rod can be seen in Figure 3.13, 3.14, 3.15, and 3.16 respectively. These plots show that the movement during the summer and fall of 2015 followed the overall trend of movement that occurred over the course of the study. The bottom left and middle left portions of the slide showed the most movement and this movement was in the negative X direction, or to the left. It can also be seen that there are very small movements occurring in the bottom and middle right portion of the slide which are occurring in the positive X direction, or to the right.

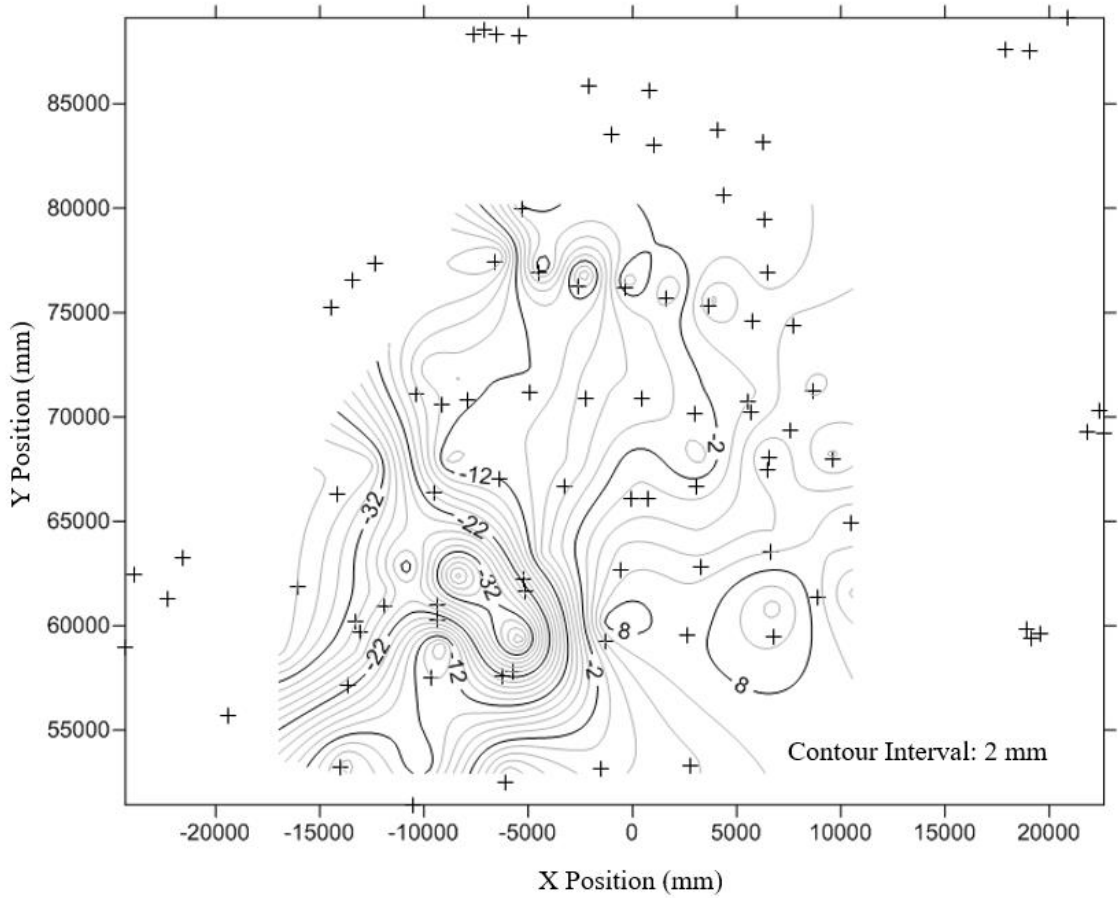


Figure 3.13. Summer and Fall 2015 Change in Top Sphere X Position between July 19, 2015 and November 22, 2015
+ Symbols Represent Target Positions. Positive X is movement toward the right of the plot.

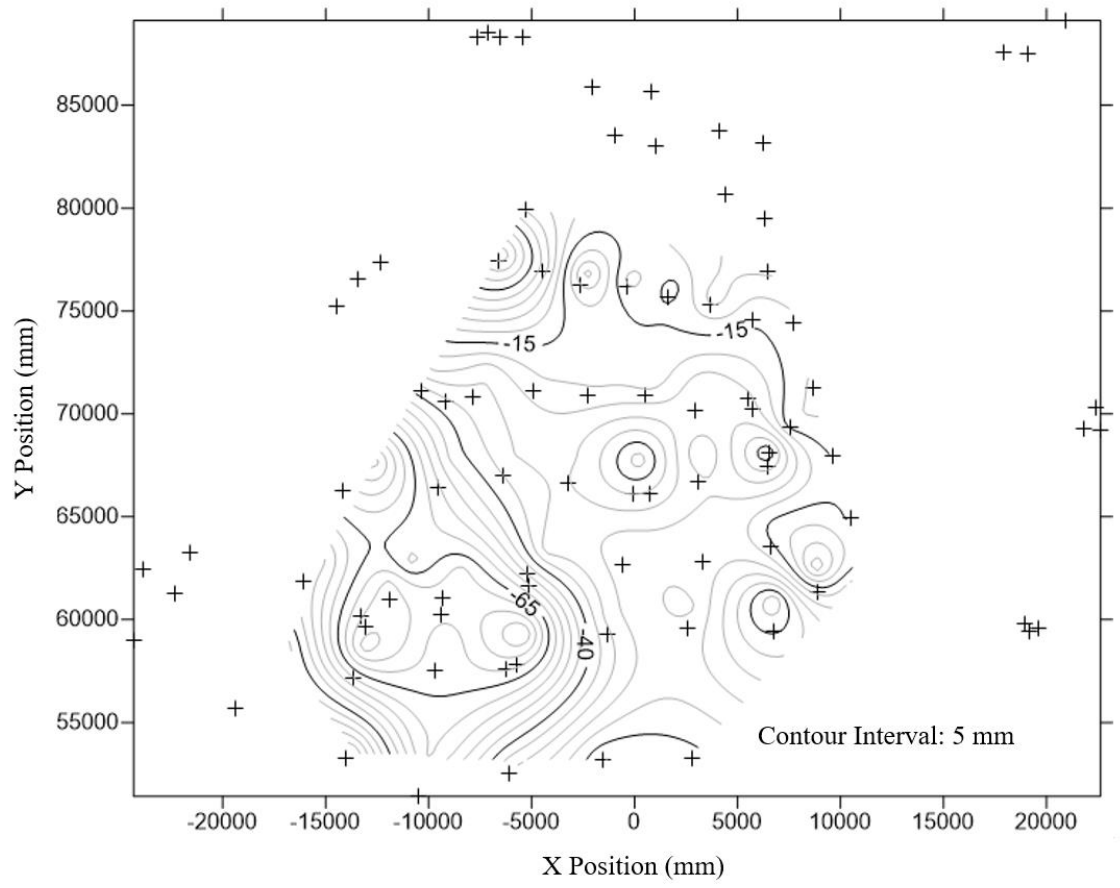


Figure 3.14. Summer and Fall 2015 Change in Top Sphere Y Position between July 19, 2015 and November 22, 2015
+ Symbols Represent Target Positions. Positive Y is movement toward the top of the plot.

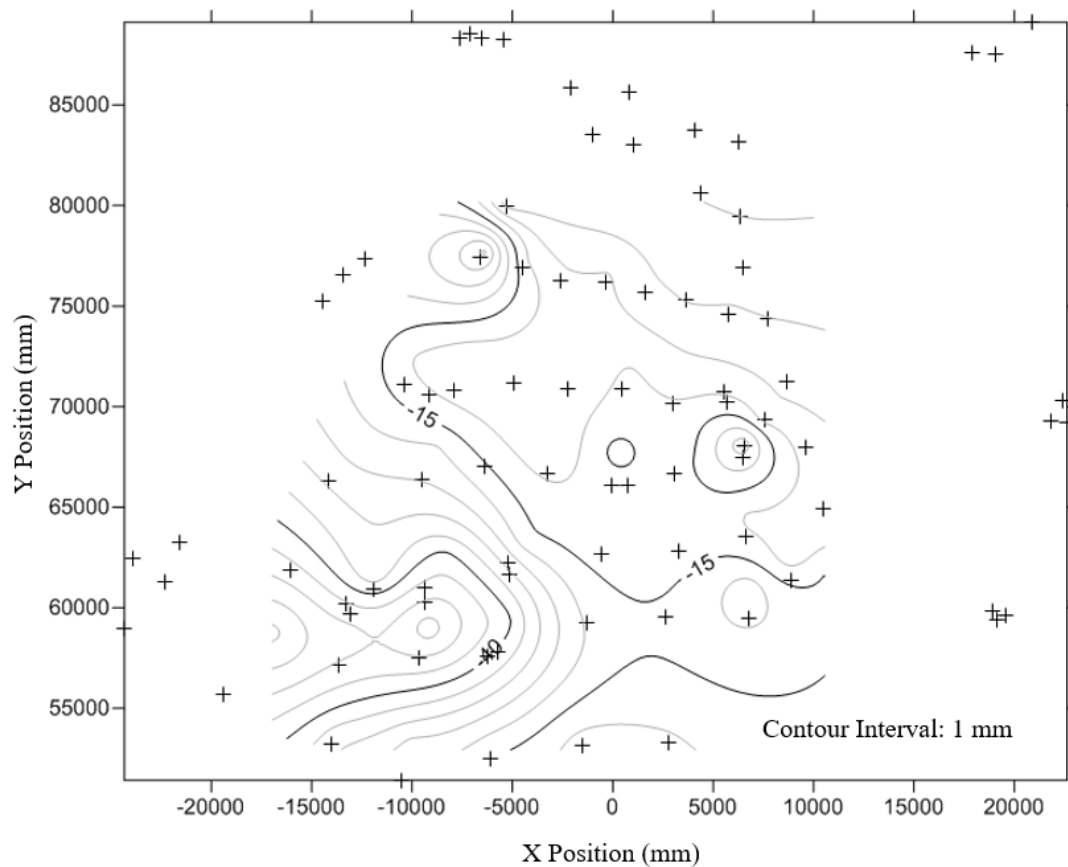


Figure 3.15. Summer and Fall 2015 Change in Top Sphere Z Position between July 19, 2015 and November 22, 2015
+ Symbols Represent Target Positions. Positive Z is movement out of the page.

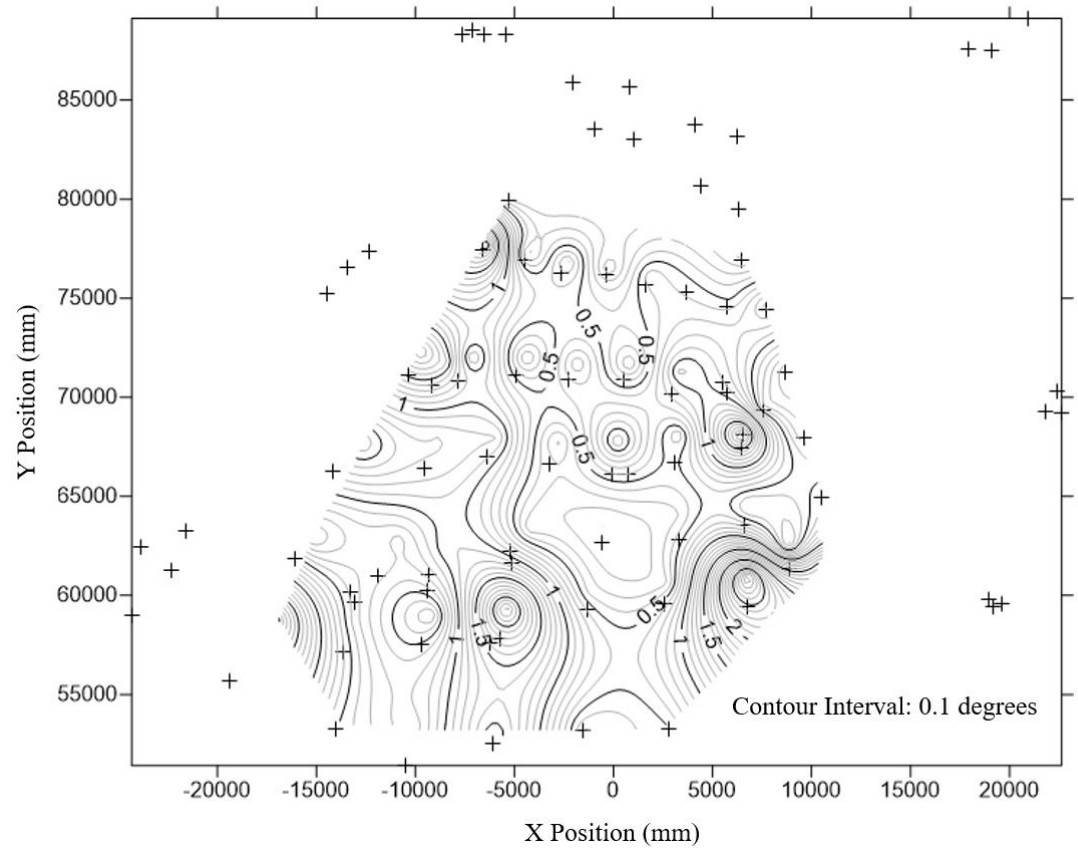


Figure 3.16. Summer and Fall 2015 Rod Rotation between July 19, 2015 and November 22, 2015
+ Symbols Represent Target Positions. Positive angle measurement is downslope rotation.

3.2.2 Winter Season of 2015 through 2016. The winter season of 2015 through 2016 is represented by the time between December 16, 2015 and May 13, 2016. The displacement report for these dates is shown below in Figure 3.17. The linear trend statistics for the displacement report is shown below in Figure 3.18.

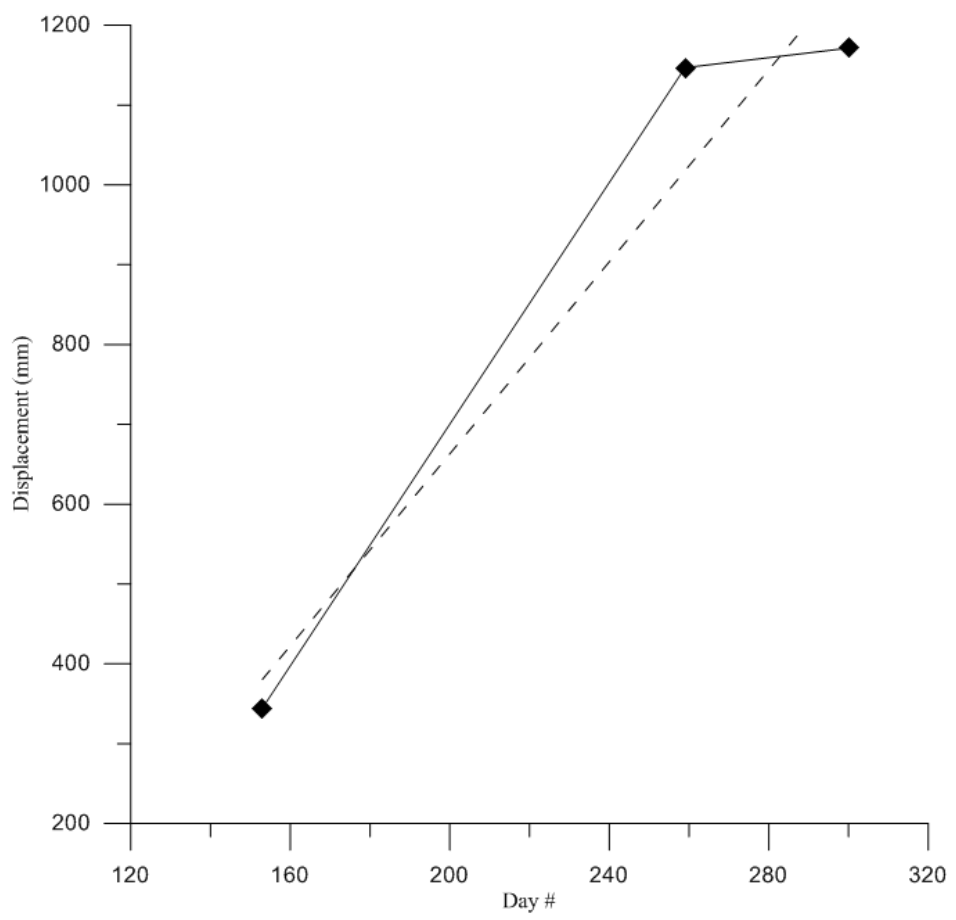


Figure 3.17. Winter 2015 through 2016 Displacement Report with Linear Trendline

Fit Results

Linear Trend
Equation $Y = 6.013535307 * X - 539.6057128$
Number of data points used = 3
Average X = 237.333
Average Y = 887.607
Residual sum of squares = 26596.6
Regression sum of squares = 416183
Coef of determination, R-squared = 0.939933
Residual mean square, $\sigma^2 = 26596.6$

Figure 3.18. Winter 2015 through 2016 Displacement Report Linear Trendline Statistics

The winter displacement was further analyzed by employing the use of contour plots similar to those present in the general displacement analysis. The contour plot representing the change in the top sphere's x position, y position, z position, and the rotation of the rod can be seen in Figure 3.19, 3.20, 3.21, and 3.22 respectively. These contour plots are quite like the contour plots that represent the overall movement of the slide from base date to final date. This is due to most the movement of the slide occurring during this particular season. The largest magnitudes of movement as well as the largest rod rotation are present in the lower left or south portion of the slide. These large magnitudes and relatively large rotations can be observed can once again be seen in Figure 3.8 and Figure 3.10.

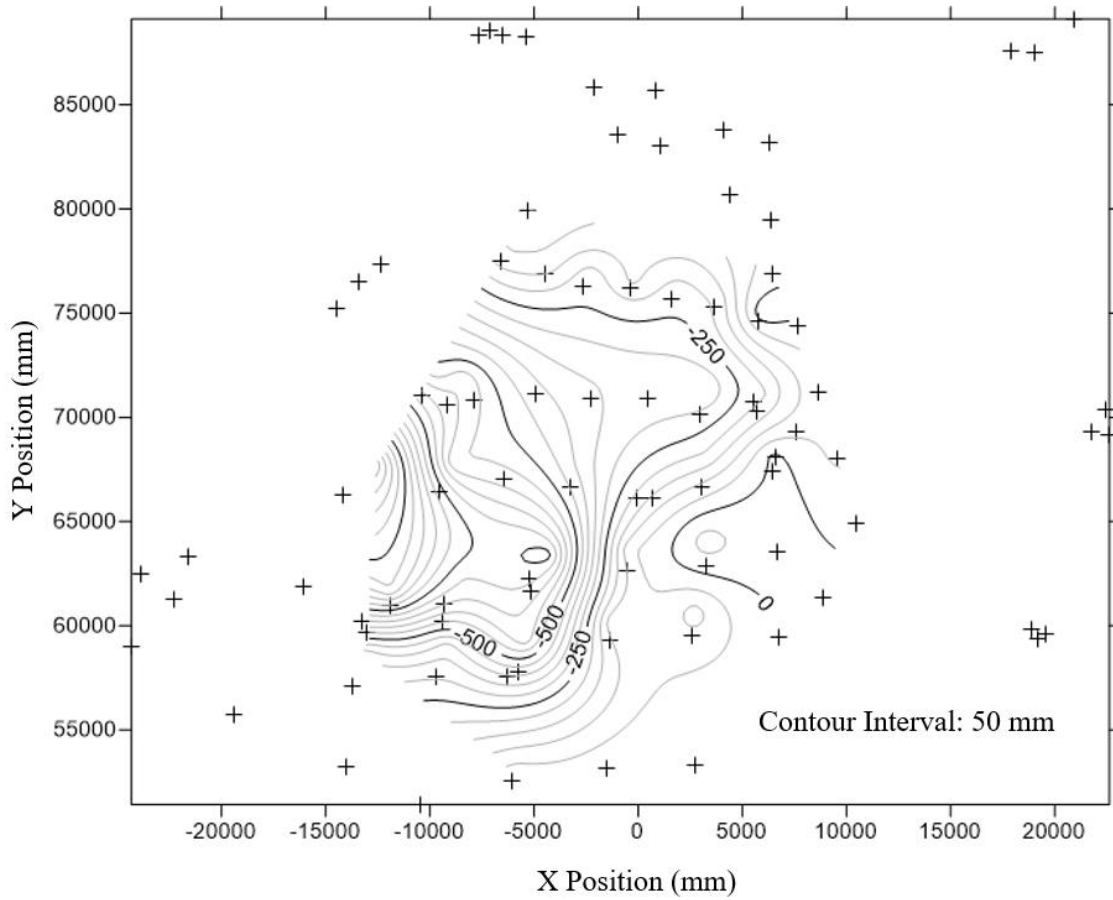


Figure 3.19. Winter season of 2015 through 2016 Change in Top Sphere X Position between December 16, 2015 and May 13, 2016
 + Symbols Represent Target Positions. Positive X is movement toward the right of the plot.

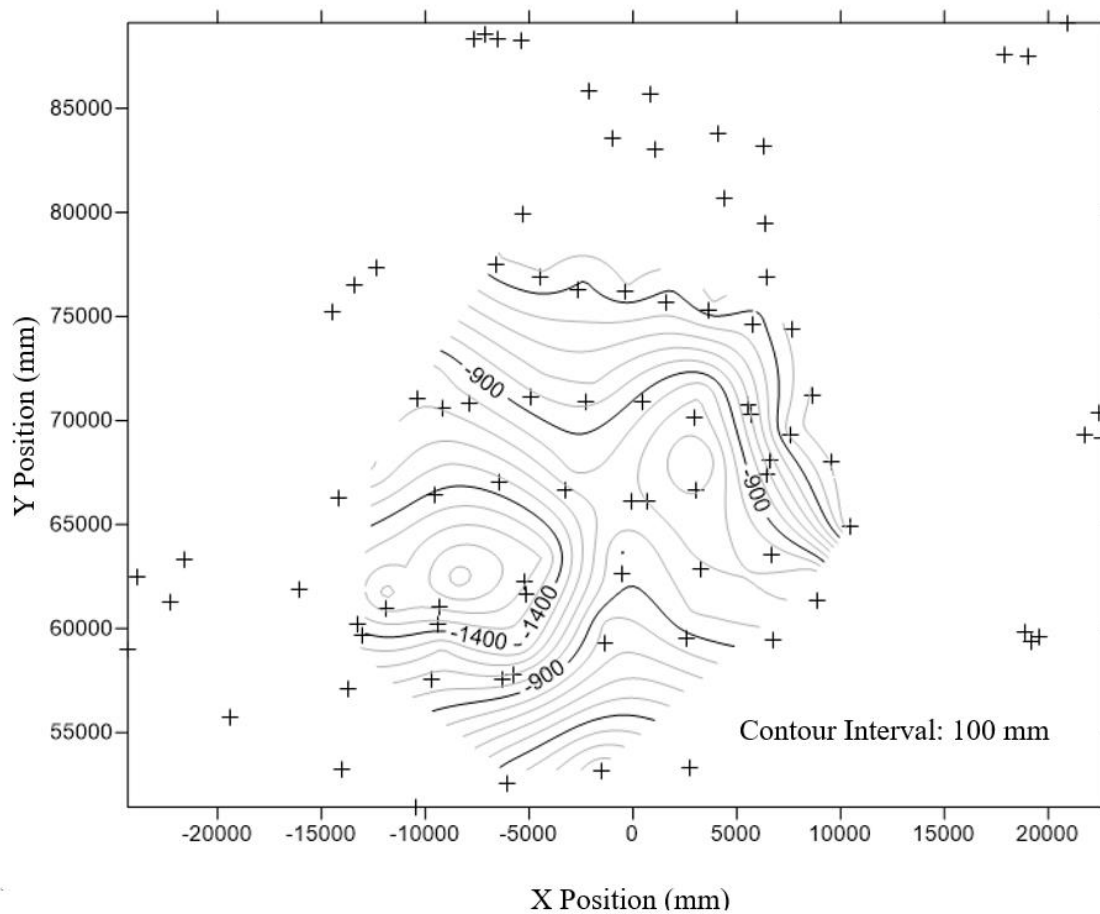


Figure 3.20. Winter season of 2015 through 2016 Change in Top Sphere Y Position between December 16, 2015 and May 13, 2016
 + Symbols Represent Target Positions. Positive Y is movement toward the top of the plot.

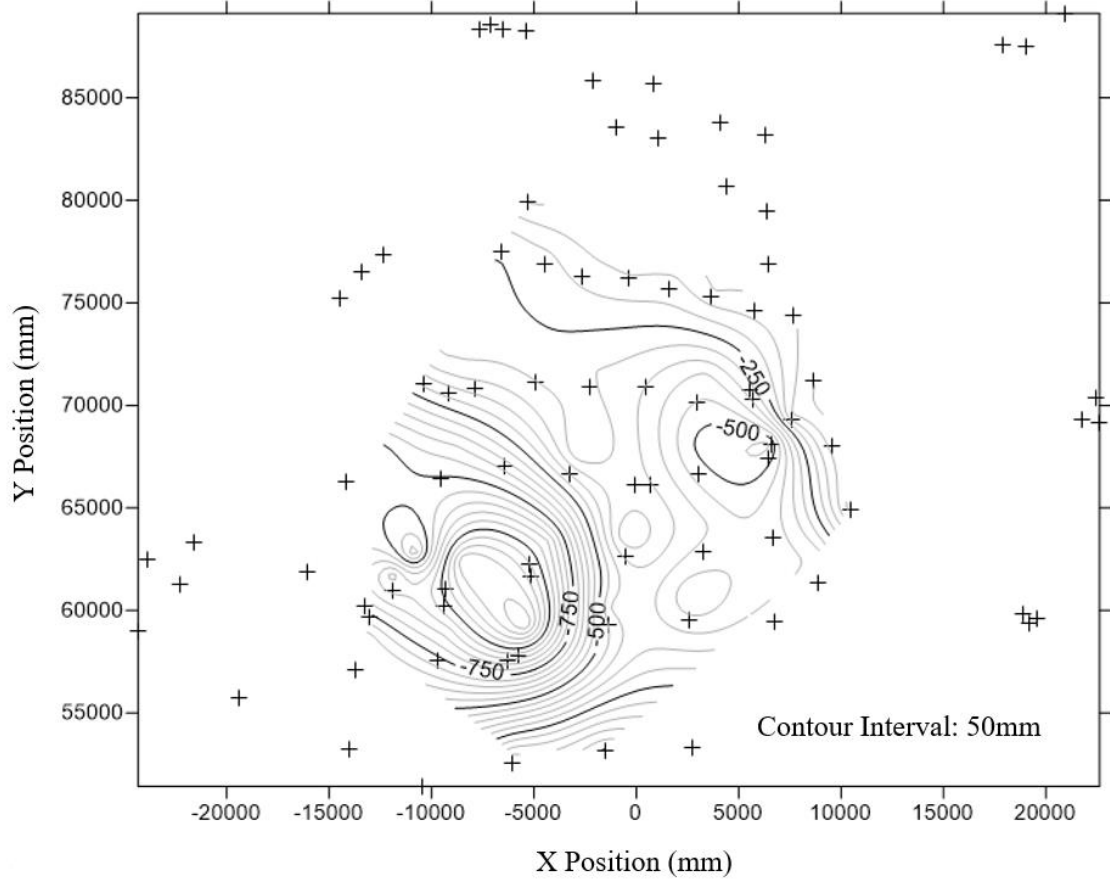


Figure 3.21. Winter season of 2015 through 2016 Change in Top Sphere Z Position between December 16, 2015 and May 13, 2016
+ Symbols Represent Target Positions. Positive Z is movement out of the page.

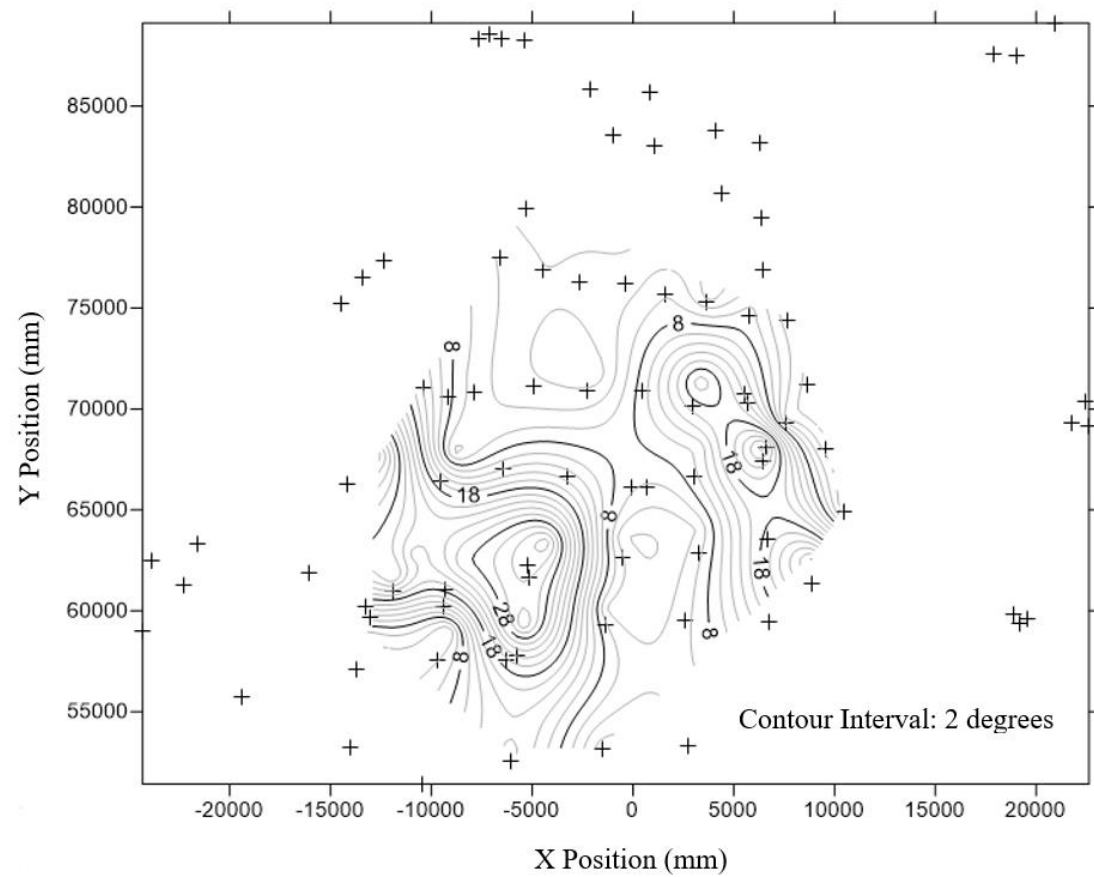


Figure 3.22. Winter season of 2015 through 2016 Rod Rotation between December 16, 2015 and May 13, 2016
+ Symbols Represent Target Positions. Positive angle measurement is downslope rotation.

3.2.3 Spring through Fall Seasons of 2016. The spring through fall seasons of 2016 are represented by the time between March 31, 2016 and November 5, 2016. The displacement report for these dates is shown below in Figure 3.23. The linear trend statistics for the displacement report is shown below in Figure 3.24.

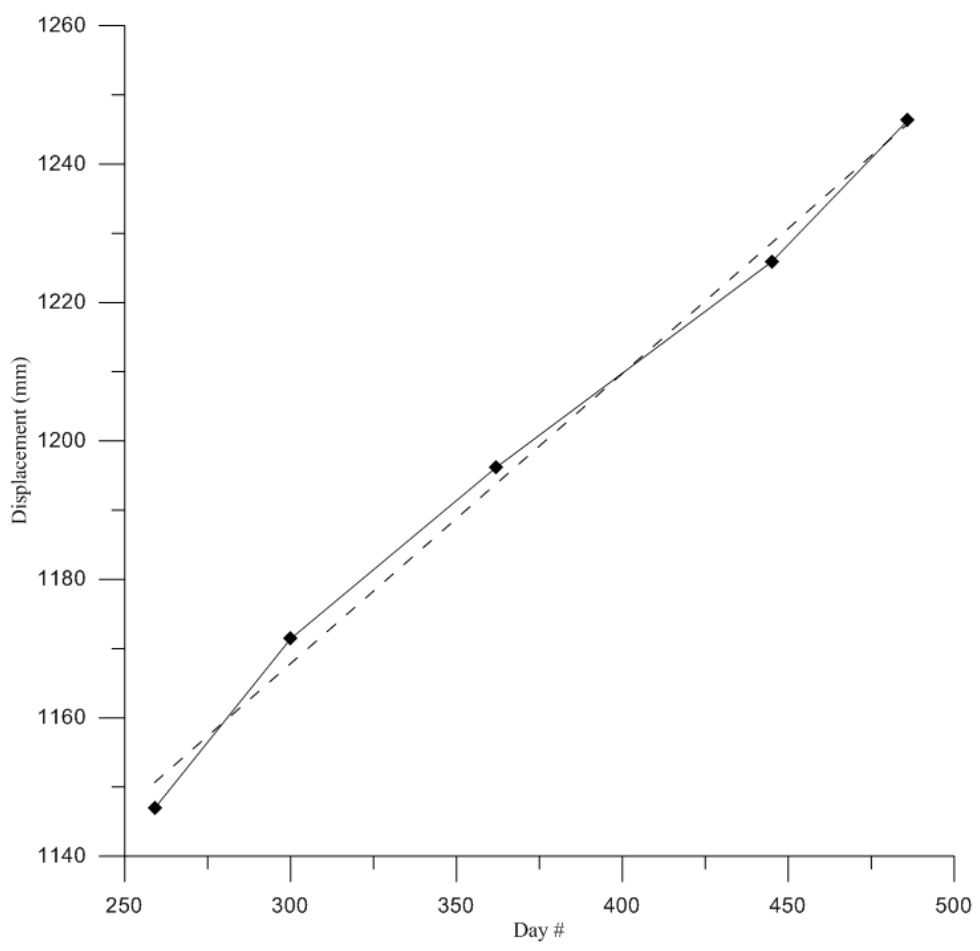


Figure 3.23. Spring through Fall 2016 Displacement Report with Linear Trendline

Fit Results
Fit 2: Linear
Equation $Y = 0.4191771254 * X + 1042.086793$
Number of data points used = 5
Average X = 370.4
Average Y = 1197.35
Residual sum of squares = 40.1639
Regression sum of squares = 6389.71
Coef of determination, R-squared = 0.993754
Residual mean square, sigma-hat-sq'd = 13.388

Figure 3.24. Spring through Fall 2016 Displacement Report Linear Trendline Statistics

The spring through fall seasons of 2016 displacements were further analyzed by employing the use of contour plots similar to those present in the general displacement analysis. The contour plot representing the change in the top sphere's x position, y position, z position, and the rotation of the rod can be seen in Figure 3.25, 3.26, 3.27, and 3.28 respectively. These contour plots show a slight change in the distribution of movement compared to the previous seasons and the overall displacement of the slide. The contour plot showing the change in a particular rod's top sphere in the x direction shows that there is a greater amount of movement occurring in the middle to top right (north) portion of the slide. The first date in this time series (March 31, 2016) is one of the dates where a collection of new rods was installed in areas where rods had either been removed or were no longer able to be seen by the scanner due to large movement. The movements during this season were quite small compared to the movements during the previous winter season.

The contour plot showing the change in a particular rod's top sphere in the z direction has greater magnitudes of movement than the contour plot showing the change in a particular rod's top sphere in the y direction. This deviates from the norm that the magnitudes of movement in the negative y direction are the greatest, which is shown in the overall movement contour plots as well as the two epochs prior to the Spring through Fall seasons of 2016. The areas with the largest magnitudes of movement in the negative z direction are associated with areas that also have the largest change in rod rotation.

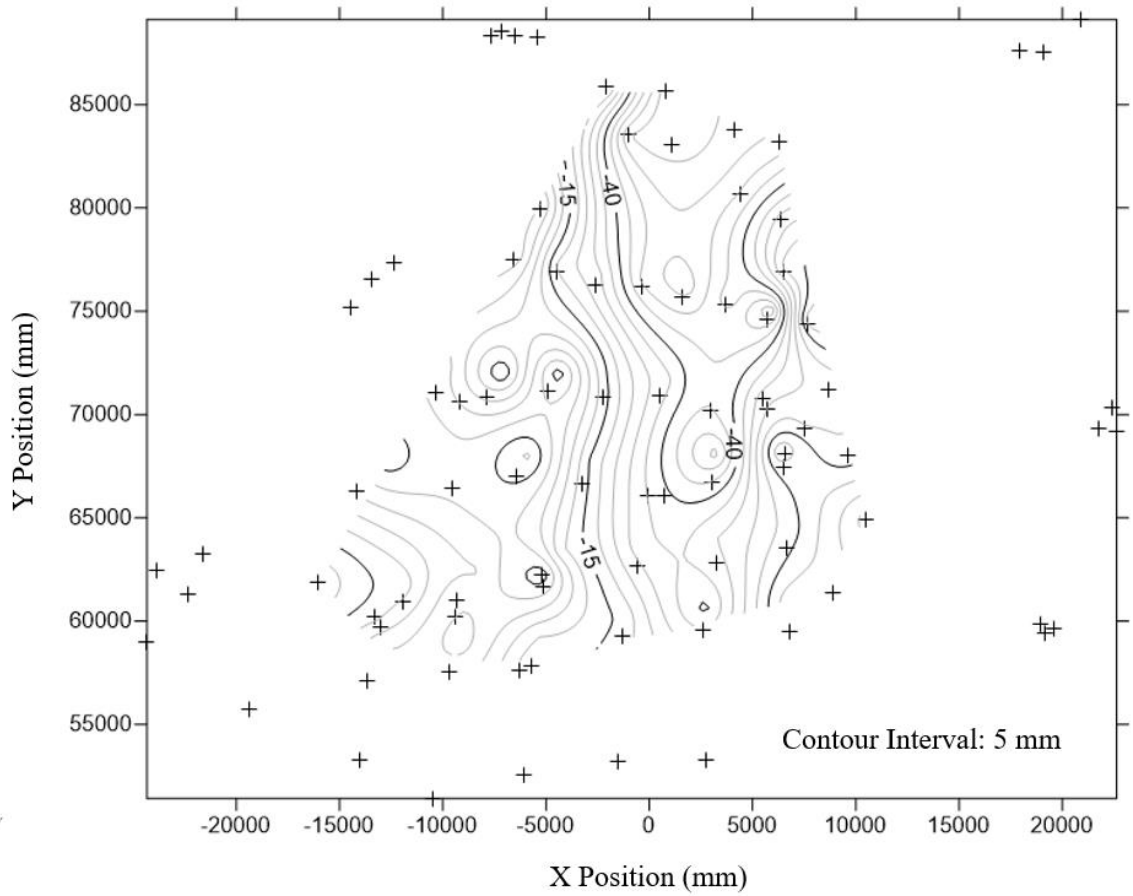


Figure 3.25. Spring through Fall 2016 Change in Top Sphere X Position between March 31, 2016 and November 5, 2016

+ Symbols Represent Target Positions. Positive X is movement toward the right of the plot.

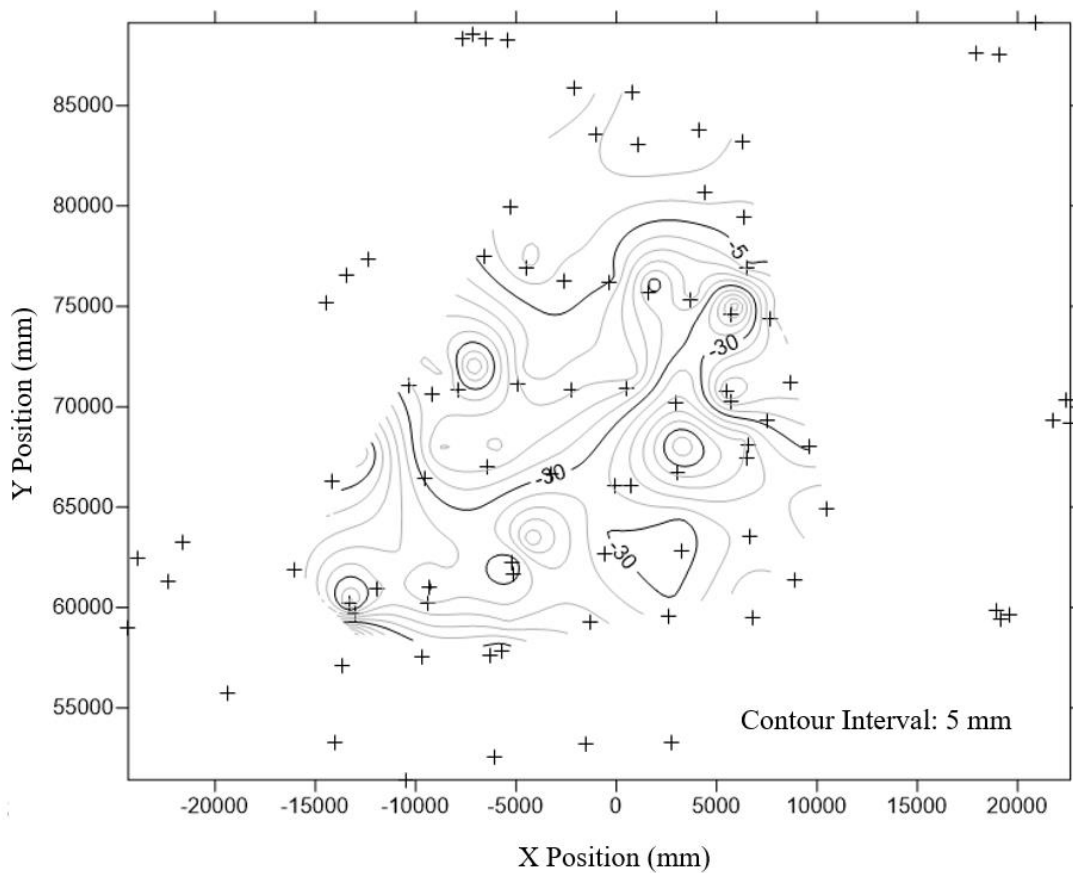


Figure 3.26. Spring through Fall 2016 Change in Top Sphere Y Position between March 31, 2016 and November 5, 2016

+ Symbols Represent Target Positions. Positive Y is movement toward the top of the plot.

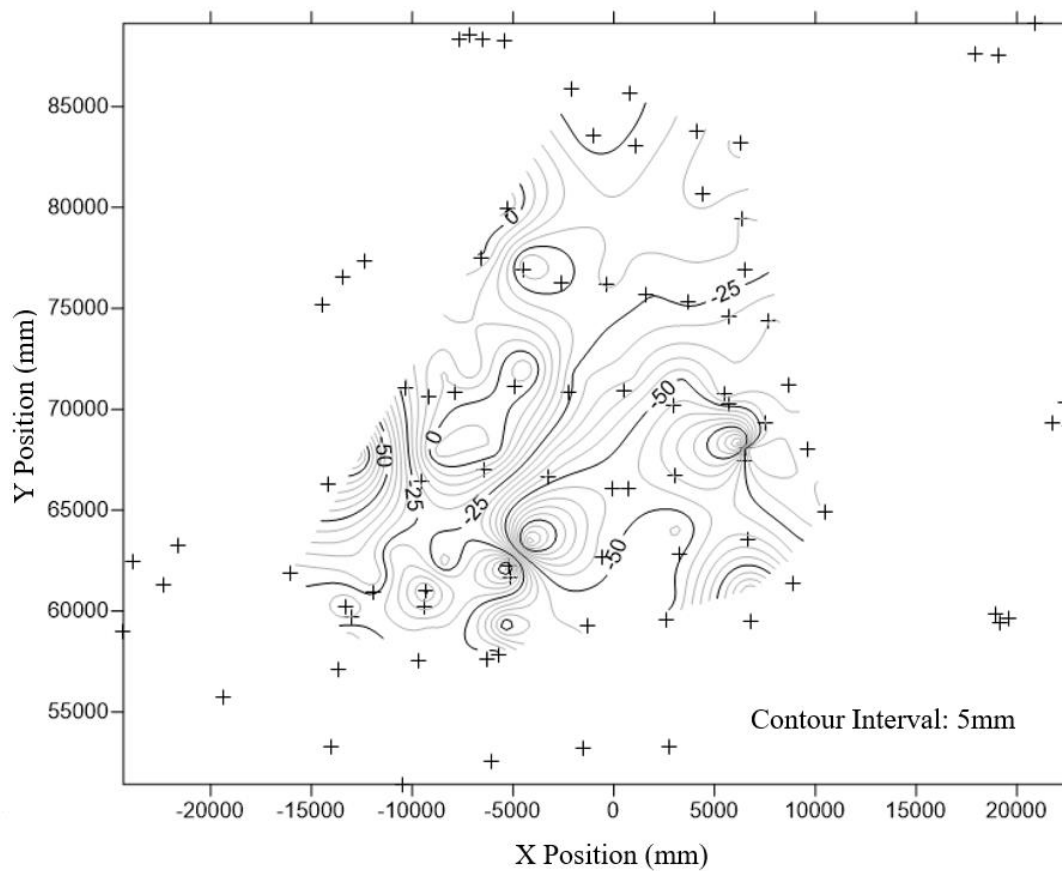


Figure 3.27. Spring through Fall 2016 Change in Top Sphere Z Position between March 31, 2016 and November 5, 2016
+ Symbols Represent Target Positions. Positive Z is out of the page.

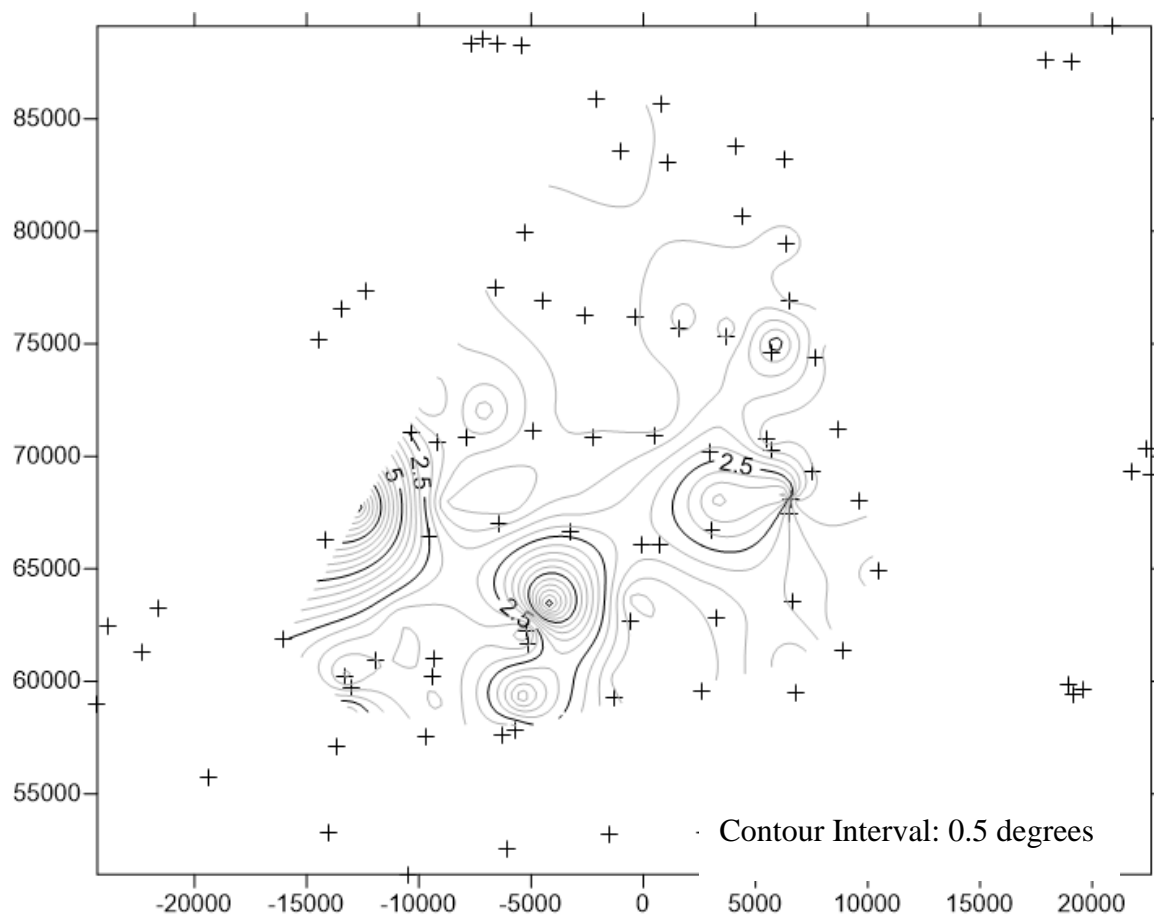


Figure 3.28. Spring through Fall 2016 Change in Rod Rotation between March 31, 2016 and November 5, 2016

+ Symbols Represent Target Positions. Positive angle measurement is downslope rotation.

3.3 GEOPHYSICAL RESISTIVITY RESULTS AND INTERPRETATION

The geophysical resistivity data collected on November 5, 2016 was processed through RES2DINV^{®ii} software to generate two-dimensional representations of the subsurface below the profile surface lines. This software was developed by GEOTOMO Software^{®iii}. The field data was processed by Aleksey Khamzin, a Postdoctoral Fellow at Missouri University of Science and Technology, and Nathainail Bashir, a PhD candidate at Missouri Univeristy of Science and Technology, both of whom have done work in

geophysics. The general location of each of the profiles can be seen above in plan view in Figure 2.17. The processed data is presented for each profile below along with an interpretation of a slide plane for each profile with the nearest rods to the profile superimposed. The rod positions and movement were obtained from specifically generated vrml files which contained the three-dimensional representation of the rods at the base date and then at the final date as well as the movement between the two dates. This vrml file and the corresponding rod locations can be seen in Figure 3.29. There are also zoomed in view of a profile in Figure 3.30. This gives an indication of how the rods are behaving in accordance with the material they are driven into and whether or not the rods have pierced the slip plane of the landslide in each profile. The slip plane was interpreted by delineated the contact between materials with low resistivity and materials with intermediate or high resistivity values. This interpretation assumes that there is a dry layer sliding on top of a moist layer.

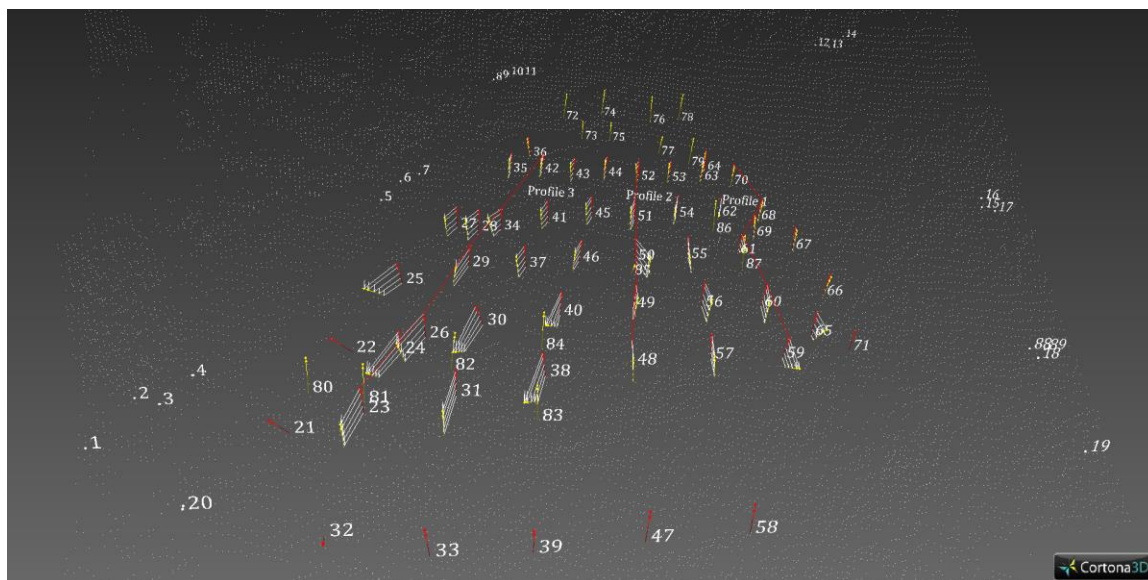


Figure 3.29. Three-Dimensional View of Landslide with Profile and Rod Positions

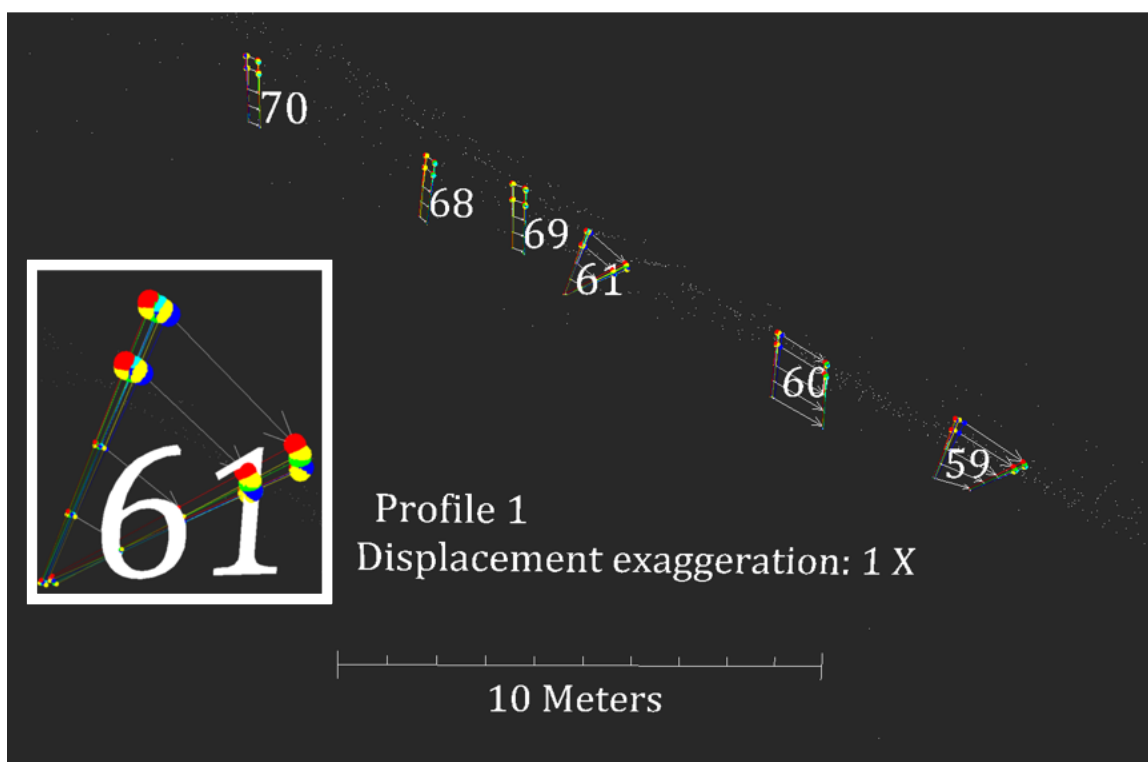
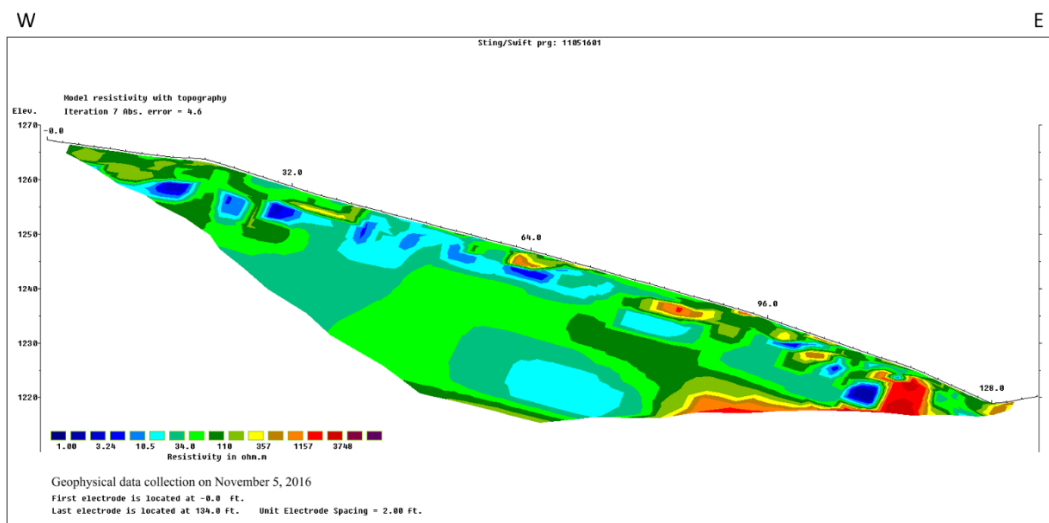


Figure 3.30. Close-up of Profile 1 with Zoomed in View of Rod 61

ERT Profile 1 representing the subsurface of north side of the landslide, can be seen in Figure 3.32. According to the data, most of the subsurface is composed of materials that have a intermediate values of resistivity with areas of low and high resistivity materials dispersed throughout. There are pockets of material with low resistivities across the entire length of the profile, some of which are relatively close to the ground surface. These areas could contain higher amounts of moisture or be clay filled zones. According to the data, there is a very highly resistive area of material near the toe of the slide. Since high resistivity values are attributed to intact rock, this could be connected to the exposed dolomite rock outcrop that is present at the northeast corner of the landslide. This outcrop can be seen on the landslide in Figure 3.31. ERT Profile 1 with an interpreted slide plane and superimposed rods can be seen in Figure 3.33. Two rods appear to be rotating forward while the others are simply translating down the landslide in this profile. The two rods that are rotating have been driven into an area of higher moisture, which has been assumed to be below the slip surface.



Figure 3.31. Exposed Dolomite Outcrop on Northeast Corner of Landslide



ERT Profile #1. collected W→E

Resistivity in ohm·m

Figure 3.32. ERT Profile 1 (North Side of Landslide)

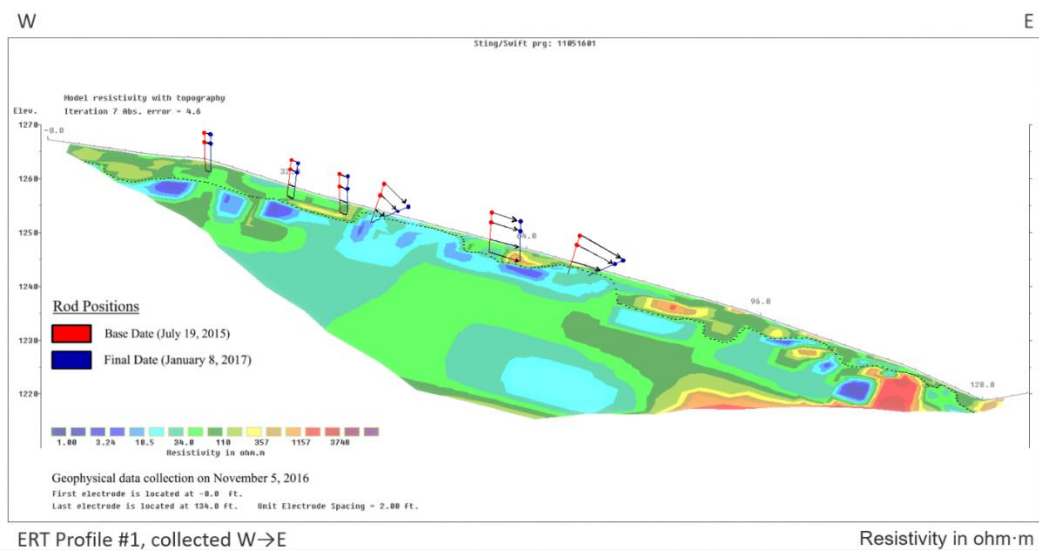
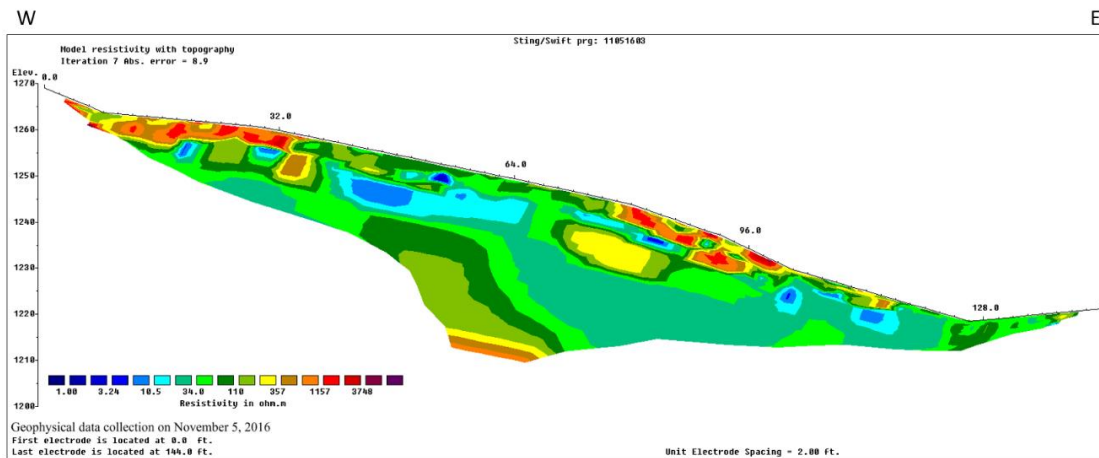


Figure 3.33. ERT Profile 1 with Slide Plane Interpreted and Rods Superimposed

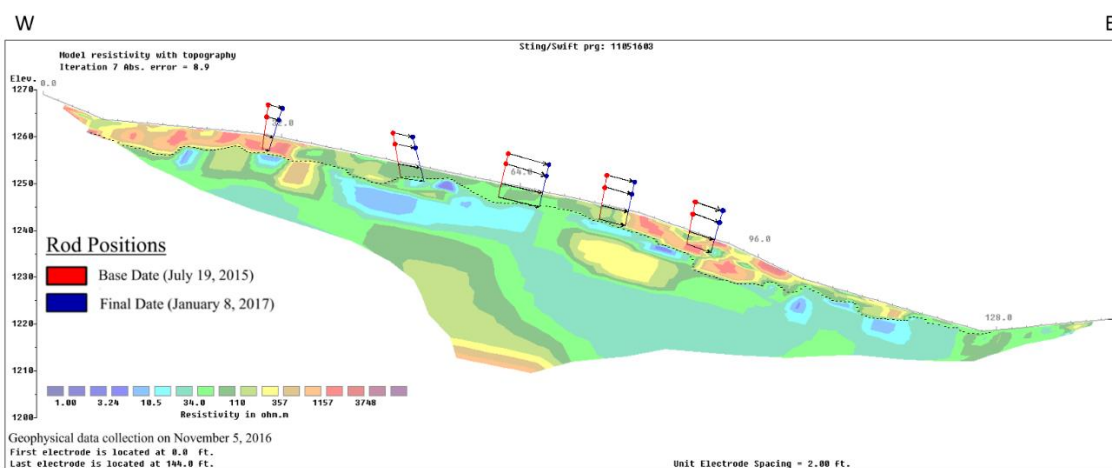
ERT Profile 2, representing the subsurface of the middle portion of the landslide, can be seen in Figure 3.34. According to the data collected from this profile, there are materials much closer to the ground surface that have a high resistivity value. According to the data, these areas could contain rock or dense fill. This is congruent with observations of non-vegetated areas of fill present on the middle portion of the slide. These areas can be seen in Figure 3.36. Zones of higher moisture content can once again be seen in the subsurface, but they are deeper than in ERT Profile 1. ERT Profile 2 with an interpreted slide plane and superimposed rods can be seen in Figure 3.35. The two rods that are closer to the head of the slide appear to be slightly rotating while the other rods are simply translating downslope. The rotation of the rod closest to the head of the scarp is occurring due to the rod moving to a more steep portion of the slope as it moves downslope. The rotation of the second rod from the head of the landslide may be happening due to the rod piercing the slip plane at that point.



ERT Profile #2, collected W→E

Resistivity in ohm·m
All distances and elevations are in feet

Figure 3.34. ERT Profile 2 (Middle Portion of Landslide)



ERT Profile #2, collected W→E

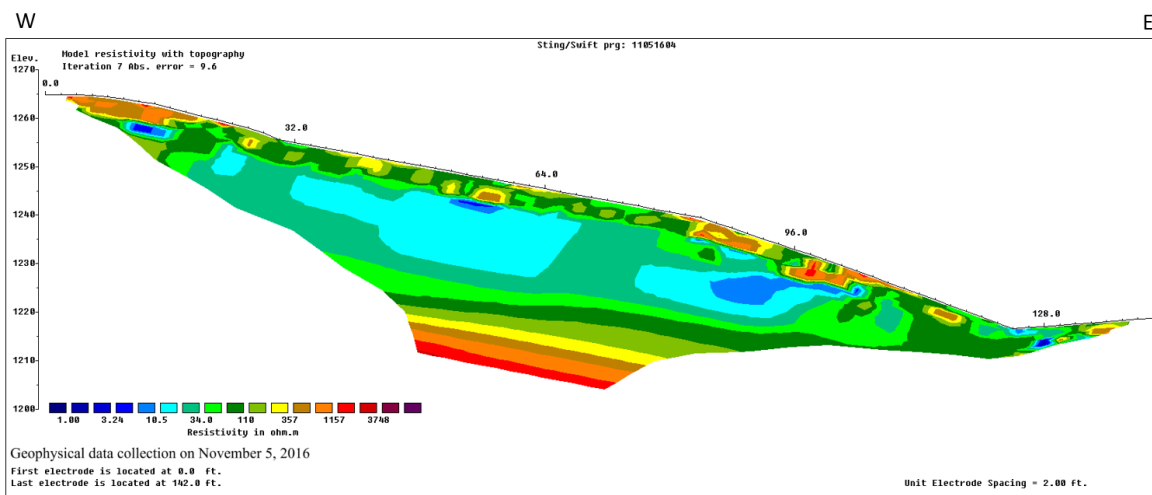
Resistivity in ohm·m
All distances and elevations are in feet

Figure 3.35. ERT Profile 2 with Slide Plane Interpreted and Rods Superimposed



Figure 3.36. Non-Vegetated Areas of Dense Fill (Example in Red)

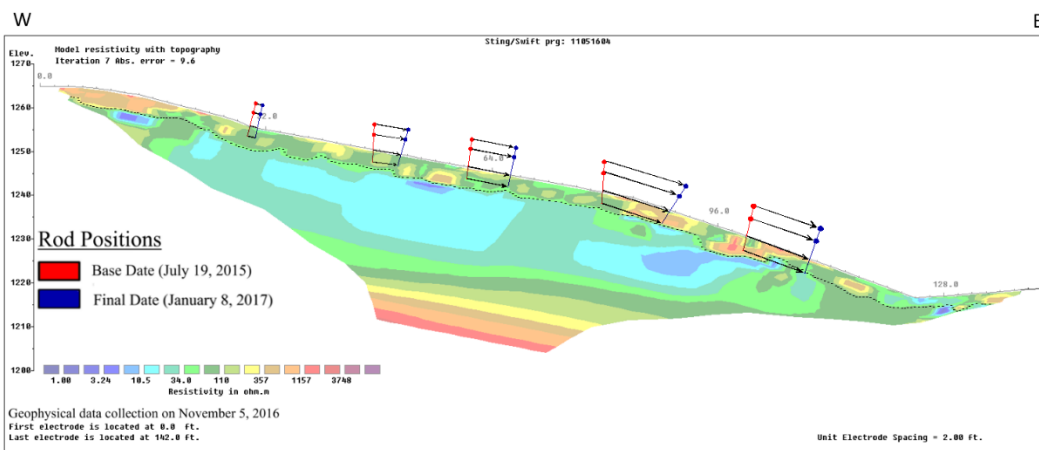
ERT Profile 3, representing the subsurface of the south side of the landslide, can be seen in Figure 3.37. According to the subsurface data collection in this profile, it looks rather similar to ERT Profile 2. The areas of high resistivity are in similar positions close to the ground surface. The large yellow ellipsoid that was present in ERT Profile 2 is not present in ERT Profile 3. ERT Profile 3 with an interpreted slide plane and superimposed rods can be seen in Figure 3.38. It appears that all of the rods present in this profile are translating downslope with very little rotational movement. The rods in this profile have most likely not pierced the slip plane of the landslide.



ERT Profile #3, collected W→E

Resistivity in ohm-m
All distances and elevations are in feet

Figure 3.37. ERT Profile 3 (South Side of Landslide)



ERT Profile #3, collected W→E

Resistivity in ohm-m
All distances and elevations are in feet

Figure 3.38. ERT Profile 3 with Slide Plane Interpreted and Rods Superimposed

4 CONCLUSIONS

From the measured data and observable movement throughout the slide, this method could show and track the behavior of the landslide at specific sections. With the help of the geophysical survey only a limited amount of useful data was able to be collected about the geometry and dimensions of the slip surface. From this data, the majority of the slide movement occurred in the bottom left portion of the slide during the winter season of 2015 to 2016. The slip surface appears to be parallel in nature with some undulation up to the surface throughout. The slip surface does not appear to have substantial rotational movement.

4.1 LIMITATIONS OF CURRENT PROCEDURE

At this point in the research of the Stone County Landslide, the geometry of the slip surface cannot be accurately inferred or interpreted. This is due to the small number of rods that pierced the slip surface when being placed on the landslide. This problem and potential suggestions to remedy it will be discussed in the next section on future research.

4.2 FUTURE RESEARCH AND DEVELOPMENT OF METHOD

There were some problems and hurdles that occurred during the study which either limited our data or hindered the potential analysis of the slide surface and subsurface behavior. A problem that occurred during the analysis of the results of this study was that only a handful of rods showed rotational movement, and most of the rods that did show this movement were not close to the ERT profiles that were collected. If the research into this method is continued, a larger number of longer rods is suggested. A majority of the floating rods present on the landslide at this time are four feet in length, two feet above

the surface and two feet below the surface. Rods with lengths of five or six feet would allow deeper penetration into the landslide and would heighten the potential that a rod would pierce the slip plane. This would add to the confidence of the geometry of the slide plane. Much shorter length rods could also be placed near these long rods to achieve more of a sense of what type of translational and rotational movement is occurring in a specific area of the landslide.

The continuation of measuring the change in x, y, and z positions of each sphere will make the future of the study more complete. This will prevent sections of data from getting lost during future studies. Along with the measuring of change in positions, during each data collection period a detailed inventory of the rods present should be taken and their condition recorded. If a rod needs to be replaced or the area around it needs to be cleared, these detailed inventories will give a sense of what materials need to be brought along during the next data collection period. It is important that each section of the landslide is properly represented by one or more rods that are actually recording the movement of that section.

The frequency at which scans are completed should be increased during seasons that exhibit a large amount of rainfall. The largest amount of movements on landslides typically happen during or after large rainfall events, so the greater amount of scans could give further insight into these large movements.

The rods that were placed in the head scarp of the slide did not show a great amount of displacement from their original position over the course of the study. This was due to their placement on the slide on March 31, 2016 which was day 259 of the study. The rods may have missed initial movements of the head scarp, and they were

placed on the scarp after the large displacement during the winter of 2015 through 2016. If the research of this monitoring method is continued into this slide, it is suggested to continue to monitor the movement of these head scarp rods.

In future research and development of this landslide tracking method, it is suggested that movement measurements be further controlled by employing the use of another monitoring tool, such as an extensometer. This will ensure the accuracy of the sphere center tracking method. Performing a similar study on another slow moving soft slope landslide would greatly increase the confidence in the method if similar results shown.

APPENDIX

INFORMATION ON REGISTERED TRADEMARKS USED IN THESIS

The following endnotes state the owners of the registered trademarks used in this thesis. They are as follows:

- i. Leica Scanstation 2 is a registered trademark of Leica Geosystems
- ii. RES2DINV is a registered trademark of GEOTOMO Software
- iii. GEOTOMO Software is a registered trademark of Geotomo LLC

BIBLIOGRAPHY

- AASHTO (1988). Manual on Subsurface Investigation. American Association of State Highway and Transportation Official, Inc., Washington D. C., 391.
- Abellan, A., Derron, M.-H., and Jaboyedoff, M. (2016). ““Use of 3D Point Clouds in Geohazards” Special Issue: Current Challenges and Future Trends.” *Remote Sensing*, 8(2), 130.
- Angeli, M.-G., Pasuto, A., and Silvano, S. (2000). “A critical review of landslide monitoring experiences.” *Engineering Geology*, 55(3), 133–147.
- Aryal, A., Brooks, B. A., and Reid, M. E. (2015). “Landslide subsurface slip geometry inferred from 3-D surface displacement fields.” *Geophysical Research Letters*, 42(5), 1411–1417.
- Aryal, A., Brooks, B. A., Reid, M. E., Bawden, G. W., and Pawlak, G. R. (2012). “Displacement fields from point cloud data: Application of particle imaging velocimetry to landslide geodesy.” *Journal of Geophysical Research: Earth Surface*, 117(F1).
- Ashkenazi, V., Dodson, A. H., Sykes, R. M., and Crane, S. A. (1980). “Remote measurement of ground movements by surveying techniques.” *Civil Eng. Survey*, 5(4), 15–22.
- Barbarella, M. (2013). “Monitoring of large landslides by Terrestrial Laser Scanning techniques: field data collection and processing.” *European Journal of Remote Sensing*, 126–151.
- Barbarella, M., Fiani, M. and Lugli, A. (2015) Landslide monitoring using multitemporal terrestrial laser scanning for ground displacement analysis, *Geomatics, Natural Hazards and Risk*, 6:5-7, 398-418
- Baum, R. L., Johnson A. M., and Fleming, R. W. (1988). “Measurement of slope deformation using quadrilaterals.” *US Geological Survey Bulletin*, 1842, B1-B23.
- Cruden, D. M. (1991). “A simple definition of a landslide.” *Bulletin of the International Association of Engineering Geology*, 43(1), 27–29.
- Cruden, D., and Varnes, J. (1996). “Landslide types and processes.” *Landslides Investigation and Mitigation, Transportation Research Board Special Report*, 247, 36–75.

- Dewitte, O., Jasselette, J.-C., Cornet, Y., Eeckhaut, M. V. D., Collignon, A., Poesen, J., and Demoulin, A. (2008). "Tracking landslide displacements by multi-temporal DTMs: A combined aerial stereophotogrammetric and LIDAR approach in western Belgium." *Engineering Geology*, 99(1-2), 11–22.
- Dunning, S., Massey, C., and Rosser, N. (2009). "Structural and geomorphological features of landslides in the Bhutan Himalaya derived from Terrestrial Laser Scanning." *Geomorphology*, 103(1), 17–29.
- Fleming, R. W., and Taylor, F. A. (1980). "Estimating the cost of landslide damage in the United States." *US Geological Survey, Circular*, 832, 21–21.
- Franz, M., Carrea, D., Abellán, A., Derron, M.-H., and Jaboyedoff, M. (2016). "Use of targets to track 3D displacements in highly vegetated areas affected by landslides." *Landslides*, 13(4), 821–831.
- Ghuffar, S., Székely, B., Roncat, A., and Pfeifer, N. (2013). "Landslide Displacement Monitoring Using 3D Range Flow on Airborne and Terrestrial LiDAR Data." *Remote Sensing*, 5(6), 2720–2745.
- Gili, J. A., Corominas, J., and Rius, J. (2000). "Using Global Positioning System techniques in landslide monitoring." *Engineering Geology*, 55(3), 167–192.
- Gonzales de Vallejo, L. I., and Ferrer, M. (2011). *Geological Engineering*. Taylor & Francis Group, London, UK, pp. 678.
- Glenn, N. F., Streutker, D. R., Chadwick, D. J., Thackray, G. D., and Dorsch, S. J. (2006). "Analysis of LiDAR-derived topographic information for characterizing and differentiating landslide morphology and activity." *Geomorphology*, 73(1-2), 131–148.
- Giussani, A., Scaioni, M., (2004). "Application of TLS to support landslides study: survey planning, operational issues and data processing." *International Archives of Photogrammetry, Remote Sensing and Spatial Information Sciences*. 36 (Part 8/W2), 318–323.
- Gruen, A., & Akca, D. (2005). Least squares 3D surface and curve matching. *ISPRS Journal of Photogrammetry and Remote Sensing*, 59(3), 151-174.
- Hungr, O., Evans, S. G., Bovis, M. J., and Hutchinson, J. N. (2001). "A review of the classification of landslides of the flow type." *Environmental & Engineering Geoscience*, 7(3), 221–238.
- Hutchinson, J. N. (1983). "Methods of Locating Slip Surfaces in Landslides." *Environmental & Engineering Geoscience*, xx(3), 235–252.

- Jaboyedoff, M., Oppikofer, T., et al. (2010). "Use of LIDAR in landslide investigations: a review." *Natural Hazards*, 61(1), 5–28.
- Jia, Y.-B. (2016). "Transformations in Homogeneous Coordinates." *Com S 477/577 Notes*, lecture, Iowa State University, Ames, IA.
- "Leica ScanStation 2." (n.d.). *Leica ScanStation 2 - Affordable, Entry-level Scanner that's Versatile & Fast - Leica Geosystems - HDS*, <http://hds.leica-geosystems.com/en/Leica-ScanStation-2_62189.htm> (Jan. 30, 2017).
- Lichti, D. D., and Jamtsho, S. (2006). "Angular resolution of terrestrial laser scanners." *The Photogrammetric Record*, 21(114), 141–160.
- Keaton, J., and DrGraff, j., 1996. Surface observation and Geological Mapping. Landslides Investigation and Mitigation, Transportation Research Board Special Report 247, pp. 178-230.
- Keefer, D. K. (1984). "Landslides caused by earthquakes." *Geological Society of America Bulletin*, 95(4), 406.
- Kenner, R., Bühler, Y., Delaloye, R., Ginzler, C., and Phillips, M. (2014). "Monitoring of high alpine mass movements combining laser scanning with digital airborne photogrammetry." *Geomorphology*, 206, 492–504.
- Kersten, T. P., Mechelke, K., Lindstaedt, M., and Sternberg, H. (2009). "Methods for Geometric Accuracy Investigations of Terrestrial Laser Scanning Systems." *Photogrammetrie - Fernerkundung - Geoinformation*, 2009(4), 301–315.
- Krauter, E. (1989). "Special lecture: applicability and usefulness of field measurements on unstable slopes." *International Journal of Rock Mechanics and Mining Sciences & Geomechanics Abstracts*, 26(3-4).
- "Leica ScanStation 2." (n.d.). *Leica ScanStation 2 - Affordable, Entry-level Scanner that's Versatile & Fast - Leica Geosystems - HDS*, <http://hds.leica-geosystems.com/en/Leica-ScanStation-2_62189.htm> (Dec. 19, 2016).
- Li, Z. (1994). "A comparative study of the accuracy of digital terrain models (DTMs) based on various data models." *ISPRS Journal of Photogrammetry and Remote Sensing*, 49(1), 2–11.
- Lowry, B., Gomez, F., Zhou, W., Mooney, M. A., Held, B., and Grasmick, J. (2013). "High resolution displacement monitoring of a slow velocity landslide using ground based radar interferometry." *Engineering Geology*, 166, 160–169.

- Mikhail, E. M., Bethel, J. S., and McGlone, J. C. (2001). *Introduction to modern photogrammetry*. John Wiley & Sons, New York.
- Mikkelsen, P. E. (1996). "Field instrumentation." *Special Report - National Research Council, Transportation Research Board*, 247, 278–316.
- Mohamed, A., and Wilkinson, B. (2009). "Direct Georeferencing of Stationary LiDAR." *Remote Sensing*, 1(4), 1321–1337.
- Monserrat, O., and Crosetto, M. (2008). "Deformation measurement using terrestrial laser scanning data and least squares 3D surface matching." *ISPRS Journal of Photogrammetry and Remote Sensing*, 63(1), 142–154.
- Palenzuela, J. C. A. A., Irigaray, C., Jiménez-Perálvarez, J. D., and Chacón, J. (2013). "Application of Terrestrial Laser Scanner to the Assessment of the Evolution of Diachronic Landslides." *Landslide Science and Practice*, 517–523.
- Petley, D. (2012). "Global patterns of loss of life from landslides." *Geology*, 40(10), 927–930.
- Prokop, A., and Panholzer, H. (2009). "Assessing the capability of terrestrial laser scanning for monitoring slow moving landslides." *Natural Hazards and Earth System Science*, 9(6), 1921–1928.
- Reid, M. E., LaHusen, R. G., Baum, R. L., Kean, J. W., Schulz, W. H., and Highland, L. M. (2012). "Real-Time Monitoring of Landslides." *US Geological Survey Fact Sheet 2012-3008*, 1–4.
- Rowlands, K., Jones, L., and Whitworth, M. (2003). "Landslide Laser Scanning: a new look at an old problem." *Quarterly Journal of Engineering Geology and Hydrogeology*, 36(2), 155–157.
- Salvi J, Matabosch C, Fofi D, Forest J (2007) A review of recent range image registration methods with accuracy evaluation. *Image Vision Computing* 25(5):578–596.
- Scaioni, M., Giussani, et al. (2004). "Monitoring of geological sites by laser scanning techniques." *International Archives of the Photogrammetry, Remote Sensing and Spatial Information Sciences*, 35, 708–713.
- Sowers, G., and Royster, G., 1978. Field investigation. *Landslide Analysis and Control*. Transportation Research Board Special Report 176, pp. 81-111.
- Teza G, Galgaro A, Zaltron N, Genevois R (2007) Terrestrial laser scanner to detect landslide displacement fields: a new approach. *Int J Rem Sens* 28(16):3425–3446.

Varela-González, M., González-Jorge, H., Riveiro, B., & Arias, P. (2013). Performance testing of LiDAR exploitation software. *Computers & Geosciences*, 54, 122-129.

Whitfield, J. W. (2004). Bedrock Geologic Map of the Garber 7.5' Quadrangle Stone and Taney Counties. *United States Geologic Survey*.
<http://dnr.mo.gov/geology/statemap/harrison/ha200402.htm>.

VITA

Benjamin “Ben” Michael Herries was born in New Orleans, Louisiana to Michael and Paula Herries. During the latter part of the summer of 2005, Hurricane Katrina forced the evacuation of the Herries family to St. Louis, MO. Ben finished up the two final years of elementary school before attending De Smet Jesuit High School for secondary education. He studied a range of college preparatory subjects, taking an interest in math and science, before graduating in the top 10% of his class in May of 2011.

Due to both of Ben’s parents being alumni from the University of Missouri – Rolla and road trips around Missouri, he was quite familiar with the town of Rolla and the engineering university’s campus. When Ben heard about the Geological Engineering program at the Missouri University of Science and Technology and all the opportunities he would have as a student and a graduate of the program, as well as the chance to work outdoors, he was sold. Ben applied to Missouri University of Science and Technology and was accepted in the latter part of 2010. Ben began his first class as a freshman in the Fall Semester of 2011. Ben graduated magna cum laude with a Bachelor’s of Science in Geological Engineering in May 2015.

Ben decided to continue his education and began the pursuit of a Master’s of Science in Geological Engineering after graduation. He received a Master’s of Science in Geological Engineering from Missouri University of Science and Technology in July 2017. Ben then began work as a Geotechnical Engineer in Training with Stantec Consulting Services in St. Louis, MO.